AD 714538

MELT-DOMINATED IMPULSE EXPERIMENTS
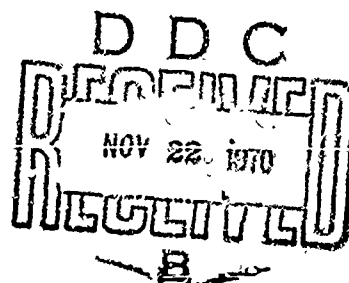# AND CALCULATIONS

FINAL REPORT

September 1970

J. Reaugh, A. Lutze, and G. Yonas

Prepared for

DEFENSE ATOMIC SUPPORT AGENCY
Washington, D.C.   20305

Under Contract DASA-01-69-C-0095
NWER Subtask 4C321

Preparing Agency

Physics International Company
2700 Merced Street
San Leandro, California 94577

DDC

NOV 22 1970

RECEIVED
B

MELT-DOMINATED IMPULSE EXPERIMENTS
AND CALCULATIONS

FINAL REPORT

September 1970

J. Reaugh, A. Lutze, and G. Yonas

Prepared for

Prepared by

Physics International Company
2700 Merced Street
San Leandro, California 94577

ABSTRACT

A combined experimental and analytical study of impulse genera-
tion in aluminum has been carried out using intense electron beams
as the source of high energy density loading. Both analytical models
and hydrodynamic codes were used in the modeling of the observed
material response. In addition this report presents a detailed
survey of current calculational techniques and an extensive dis-
cussion of the experimental methods required for this work. For
the electron beam fluence range employed here, giving peak doses
less than 2000 cal/g, a model of liquid spall was found to represent
the data well. This model was simplified to an analytical expres-
sion which depends exponentially on deposition time and is suitable
for predicting melt-dominated impulse in a wide range of materials.
In addition, hydrodynamic code calculations have been carried out
and comparisons are made with measured transmitted stress histories
and liquid ejecta velocities.

FOREWORD

This report presents the results of a 15-month program, begun January 23, 1969, and completed April 22, 1970. The program was supported by DASA Contract 01-69-C-0065 and monitored by Captain Allen A. Weston. Our purposes were to investigate an important material-response phenomenon, namely the generation of impulse in test materials under well-diagnosed loading conditions using electron beams, and to develop appropriate models for impulse generation in a wide range of materials.

The work was conducted by members of Physics International Company's Intense Beams and Applications Group within the Nuclear Radiation Effects Department, under the supervision of Dr. Alan Klein. Principal investigators were Dr. Gerold Yonas, Program Manager, and Messrs. Andrew Lutze and John Reaugh, Program Physicists.

The authors acknowledge the important contributions of Dr. Phillip Spence and Mr. Sergei Heurlin in the characterization of the electron beam environment and the work of Mr. James Call, the technician who gave substance to many of our ideas.

CONTENTS

ILLUSTRATIONS

ix

ILLUSTRATIONS (cont.)

ILLUSTRATIONS (cont.)

SECTION I

INTRODUCTION

For several years intense electron beams have been suggested
as a suitable laboratory tool for investigating the high energy density
response of materials. Recent developments in beam handling and
diagnostic techniques, along with improvements in laboratory
methods of diagnosing material response, have permitted workers
in this field to collect data that can be of great value in deter-
mining material properties and in evaluating the hydrodynamic
codes or analytical methods that use these material parameters.

The essence of this technique is to use a well-characterized
electron deposition profile with a sufficiently large area of
irradiation that one dimensional stress-wave propagation can be
assured in the solid material and one-dimensional flow in any
material ejected from the front surface. In addition, one is
interested in achieving high enough energy densities such that
material phase changes can occur. To accomplish this, one must
work with relatively high-current electron beams using low-
impedance pulsers. With the advent of low-impedance transmission
lines and diode structures between 1965 and 1967, it became possible
to generate the required beams. Beam physics research has been
continuing since that time and beam control and diagnostic methods
have been constantly evolving (References 1-3). In addition,
pulsers capable of generating increasingly higher currents have
been developed and the present state of development should be viewed
as an intermediate one (Reference 4).

The goal of this work was to investigate the response of a
relatively simple material to high energy density loading in order
to provide a firm empirical basis for analytical modeling. The
state of development of the electron beams at the time of this work

1

was such that peak doses less than 2000 cal/g could be achieved over areas of 3 cm^2 using the Physics International 738 Pulserad. Such a beam was therefore used to study the process of impulse generation resulting from blow-off and the material chosen was aluminum. Aluminum itself was used as a sample material for several reasons: (1) it is a relatively easy-to-obtain, inexpensive, representative metal, (2) it has no major solid-solid phase transitions, nor is it particularly rate sensitive, so that the calculation of stress wave propagation is straightforward. The results, however, are thought to apply to all homogeneous materials that undergo a solid-liquid transition in the energy-density range of interest.

Since the completion of the experimental portion of the program, further techniques have been developed using the 738 Pulserad, which allow one to achieve doses up to 6000 to 7000 cal/g uniformly over areas of roughly 0.5 cm^2 (References 5 and 6) and it is expected that the extension of the work discussed here to this higher dose range, will be relatively straightforward.

This report, then, presents an in-depth approach to one of the fundamental problems characteristic of impulse generation; namely, that dominated by removal of material in a liquid phase. In addition, the report presents a rather general discussion of the analytical and hydrodynamic computer code modeling of impulse generation over the full range of phenom nology from solid spall to full vaporization. Finally, suggestions are presented as to how this method can be extended to cover the entire scope of impulse-generation effects.

SECTION II

ANALYSIS OF IMPULSE GENERATION

A.   INTRODUCTION

This report is concerned with the generation of a net impulse[*]
in a material by sudden deposition of energy through the use of a
high-intensity electron beam. The process of energy deposition by
electrons slowing down in a material in itself imparts essentially
no momentum. (At the nominal electron beam parameters used in the
experiments, 50 cal/cm^2 of 0.25 MeV electrons, the total beam
momentum is less than 0.01% of the typically measured values.)
Since momentum is conserved in the motion of deformable bodies,
the imparting of a net impulse requires ejecting material from the
front (irradiated) surface. The content of this report is essen-
tially a study of the way in which material is ejected.

Before presenting a detailed discussion of calculational
techniques for predicting impulse, it will be useful to give a
qualitative picture of the processes involved in removing material
from a suddenly heated region. As a benchmark for this discussion,
we will consider the case where no net impulse is generated--a solid
that stays solid.

Suppose a finite region inside a material is heated instan-
taneously. There is then a sudden localized temperature rise,
$T - T_o$. Since the material is compressible, it takes time to expand
to the relaxed volume $V_o(1 + 3\alpha(T - T_o))$ where α is the linear
coefficient of thermal expansion. The material is effectively

_____

[*]As used throughout this report, impulse is defined as momentum
per unit area.

3

compressed by a thermal strain in the amount $3\alpha(T - T_o)$. This,
then causes a stress $P = K(3\alpha)(T - T_o)$, where K is the bulk modulus.
If e is the specific deposited energy, the formula

$$P = \frac{K(3\alpha)}{C_v} \, e = \gamma \frac{e}{V}$$

holds, where C_v is the specific heat and γ is the Gruneisen ratio.
If we assume that the material is elastic and that conditions of
one-dimensional strain hold, the stress pulse will separate into
two elastic waves moving in opposite directions with half the
original amplitude. If the heated region starts at a free surface,
one (compressive) wave moves into the cold material. The wave
moving initially toward the heated surface is reflected with op-
posite sign and moves into the solid. In this way, then, a
suddenly heated region near the front surface generates a compres-
sive and tensile stress pulse moving into the material. A point
inside the material will feel first the compressive (direct) part,
then the tensile (reflected) part. In this way there is no net
impulse:

$$\int_o^\infty P \, dt = 0$$

As was stated earlier, in order to generate a net impulse by
sudden heating, material must be ejected at the front (irradiated)
surface. This ejection is basically one of two types—the motion
of spalled or vaporized material away from the solid. Much of the
difficulty with describing impulse generation quantitatively is
associated with the fact that the two types of ejection are not
distinct, and are truly only appropriate at the extremes of tem-
perature rise.

4

Spall, the low-temperature phenomenon, is simply tensile failure. The (reflected) tensile stress wave exceeds the cohesive strength. If this occurs at only one depth in the material, all the material moving away from the solid remainder is ejected; if it occurs over a region, that region solid is pulverized. For the case at hand, the spalled material has a uniform velocity away from the solid, since that is the direction of material motion in the reflected wave. The fact of spall implies that the stress wave in the remaining solid will no longer be symmetric--the tensile part will no longer exceed the cohesive strength--and a net impulse is generated.

On the other hand, very large temperature rises will produce vaporization. The vapor state, unlike the solid, has the property that it is never in tension. The fact that it is never tensile, however, implies that there is also no restoring force once it begins to expand. As a consequence, the vapor moves away from the solid, and the stress pulse in the solid is a compressive pulse that decays slowly as the pressure of the vapor on the solid surface decays.

Neither of the above pictures of behavior, which may be considered a mechanical description, are totally accurate. This is seen to be the case, particularly when one considers a phase diagram drawn from considerations of equilibrium thermodynamics. The paths to be considered on the equation-of-state surface are the initial pressure (and temperature) rise at constant volume, and the adiabatic release paths.

In Figure 1, in particular, two release adiabats are shown on such a phase diagram. The heavy line represents the path taken by the spall model, used in this case to describe liquids.

Liquid Spall Model

Presumed Actual Behavior

Gas

Critical
Point

Solid

Solid-Liquid

Liquid

Pressure

STP

Liquid-
Vapor

Vapor

T_C

Triple Line

Solid-Vapor

Volume
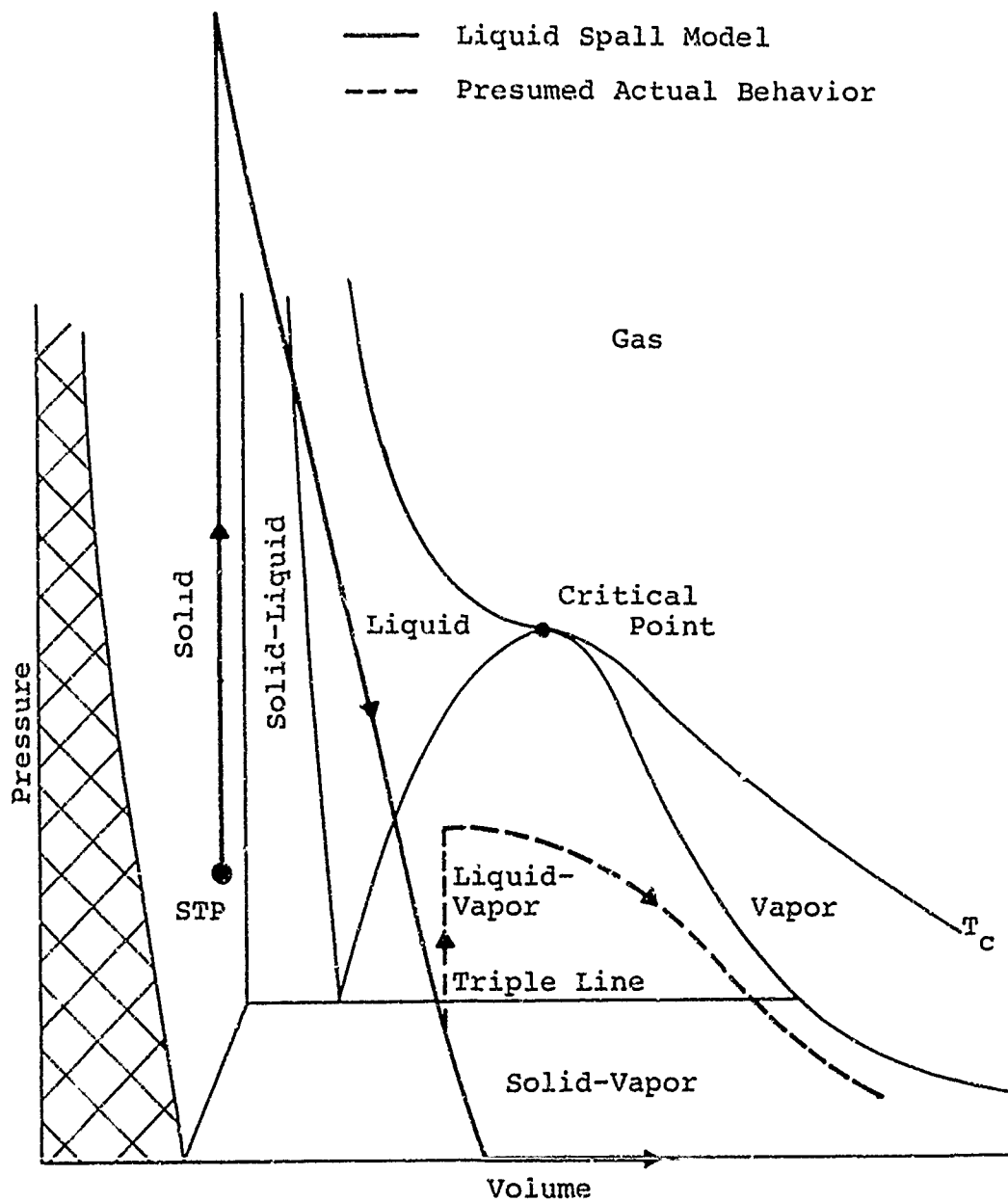
FIGURE 1.   SCHEMATIC LOADING PATH AND RELEASE ADIABATS

6

The solid-liquid phase transition is ignored, and the liquid is
assumed to release to just below zero pressure, the liquid cohesive
strength, followed by spalling of the liquid so that zero pressure
is maintained. The actual path taken is probably more like the
dashed line. The liquid release adiabat is followed down to some
positive pressure, the metastable limit. It then jumps back to
some equilibrium vapor pressure, and further expansion occurs in-
side the liquid-vapor dome. The liquid spall model, however, is
found to describe the behavior of liquid spall quite well. This
can only be the case when the equilibrium vapor pressure is quite
small with respect to the initial pressures, so that ignoring the
vapor pressure affects the solution very little. For solid spall,
of course, the equilibrium vapor pressure is less than the triple
line pressure (for materials that exhibit a liquid state it is
less than 1 atm) so that the pressure can be considered zero.

Vapor expansion adiabats, too, will cross into the liquid-
vapor coexistence region (Reference 7). If the initial deposited
energy density is high enough, however, it will occur at sufficiently
low pressures so as not to materially affect the impulse generated.

There are several methods of calculating the impulse generated
by rapid energy deposition in a slab of material at ambient con-
ditions. These methods may be grouped into two categories, that
use respectively, "analytical expressions" and "hydro-codes." The
analytical expressions require the evaluation of a one-dimensional
integral, which is the total impulse. The hydro-codes are of a
family of computer programs evolved from programs, developed at
the University of California's Lawrence Radiation Laboratory, that
require an equation-of-state of the form $P(V,E)$. These programs are
used to calculate the detailed motion (typically in one dimension)
of the expanding material. The total impulse is then the asymptotic
value of this momentum at long time intervals.

7

B. ANALYTICAL EXPRESSIONS

Two expressions are in use that give impulse as an integral. They are the Whitener formula and the BBAY formula. In their most general form, they are given in Equations (1) and (2), respectively.

$$I = \sqrt{2} \int_0 \left[E_i(m) - E_f(m) \right]^{\frac{1}{2}} dm \tag{1}$$

$$I = 1.2 \left\{ 2 \int_0 m \left[E_i(m) - E_f(m) \right] dm \right\}^{\frac{1}{2}} \tag{2}$$

1. Derivation of the Expressions

a. Whitener Formula

The Whitener formula may be derived from consideration of an incremental mass inside the expanding material. By considering the final state energy to be partitioned into the kinetic energy of the hydrodynamic motion, and the final state internal energy density,

$$\tfrac{1}{2} \Delta m \, (V^2) + E_f \, \Delta m = E_i \, \Delta m \tag{3}$$

where E_i is the initial energy density. Obtaining the expression for momentum, by assuming unidirectional velocity, and summing the contributions gives

$$I \equiv \int_0 V \, dm = \sqrt{2} \int_0 \sqrt{(E_i - E_f)} \, dm \tag{4}$$

8

b. **BBAY Formula**

The BBAY formula (Reference 8) is a closed form solution to the one-dimensional equations of motion and conservation. The hydrodynamic equations are

$$\frac{\partial x}{\partial \sigma} = V$$

$$\frac{\partial x}{\partial t} = U$$

$$\frac{\partial U}{\partial t} = -\frac{\partial p}{\partial \sigma}$$

$$\frac{\partial \varepsilon}{\partial t} = D(\sigma,t) - p\frac{\partial V}{\partial t} \qquad (5)$$

where $D(\sigma,t)$ is the heating rate, x is the Eulerian (space) coordinate, χ is the Lagrange (material) coordinate, $\sigma_{(\chi)} \equiv \int_0^x \rho_o(x')dx'$ is the areal density from front surface, V is volume, U is material (particle) velocity, and ε is the internal energy density. The fourth expression contains the hydrodynamic assumption of small distortional energy and no viscosity.

It is assumed that the deposition occurs at a constant rate, and that the final internal energy is subtracted out, so that

$$D(\sigma;t) = \begin{cases} \max[E_i(\sigma) - E_f(\sigma),0]/\rho_o(\sigma)t_1, & 0 \leq t < t_1 \\ 0 & t_1 \leq t \end{cases}$$

where $E_i(\sigma)$ is the total energy per unit volume to be deposited at σ. The quantity σ_v has the property that

$$E_i(\sigma_v) = E_f(\sigma_v)$$

9

Defining a new dependent variable Z by

$$Z = \int_0^\sigma x(\sigma',t)\,d\sigma'$$

the expressions of Equation (5) become

$$X = Z'$$
$$V = Z''$$
$$U = \dot{Z}'$$
$$P = -\ddot{Z}$$
$$\dot{\varepsilon} = D(\sigma;t) + \ddot{Z}\dot{Z}'' \qquad (6)$$

If the equation of state of the vapor is given by

$$\varepsilon = pV/(\gamma-1)$$

the γ-law gas assumption,

$$\dot{\varepsilon} = (\dot{p}V + p\dot{V})/(\gamma-1).$$

Thus the $\dot{\varepsilon}$ equation of (6) becomes

$$D(\sigma;t) + \ddot{Z}\dot{Z}'' = [-\dddot{Z}\,Z'' - \ddot{Z}\dot{Z}'']/(\gamma-1),$$

or

$$\dddot{Z}\,Z'' + \gamma\ddot{Z}\,\dot{Z}'' = -(\gamma-1)\,D(\sigma,t).$$

Assuming that Z is separable,

$$Z(\sigma,t) = Y(\sigma)\,f(t), \text{ and}$$

$$[f\,\dddot{f} + \gamma\dot{f}\,\ddot{f}]YY'' = -(\gamma-1)\,D(\sigma;t).$$

10

Since D is a function of σ only,

$$\dddot{f}\,\dot{f} + \gamma \dot{f}\,\ddot{f} = \begin{cases} \Gamma_s, & 0 \le t < t_1 \\ 0, & t_1 \le t \end{cases} \tag{7}$$

and

$$Y\,Y'' = -(\gamma-1)\,D(\sigma,t)/\Gamma_s = -(\gamma-1)\max[E_i(\sigma) - E_f(\sigma),0]/(\Gamma_s \rho_o(\sigma) t_1) \tag{8}$$

where Γ_s is the separation constant.

Equation (7) is solved by $f = t^m$, $0 \le t < t_1$, which becomes

$$t^{2m-3}\,[m(m-1)(m-2) + \gamma m^2(m-1)] = \Gamma_s \quad \text{implying}$$

$$2m - 3 = 0 \quad \text{so} \quad m = \frac{3}{2}, \quad \Gamma_s = \frac{3}{8}(3\gamma-1)$$

For $t \ge t_1$, $f^{-(\gamma-1)}\dfrac{d}{dt}(f^\gamma\,\ddot{f}) = 0$, or

$$f^\gamma \ddot{f} = \text{const} = t_1^{3/2\gamma}\,\frac{3}{2}\,(\tfrac{1}{2})\,t_1^{-1/2} = \frac{3}{4}\,t_1^{(3\gamma-1)/2}$$

Thus for $t \ge t_1$ and using $f(t_1) = t_1^{3/2}$, one obtains the solution

$$\dot{f} = \left[\frac{3t_1}{2\beta} - \frac{3t_1^{(3\gamma-1)/2}}{2(\gamma-1)}\,f^{-(\gamma-1)}\right]^{\frac{1}{2}},$$

where

$$\beta = \left[\frac{3}{2} + \frac{1}{\gamma-1}\right]^{-1} = \frac{3(\gamma-1)}{4\Gamma_s}.$$

Equation (8) becomes

$$Y\,Y'' = -\frac{4}{3}\,\frac{\beta}{\rho_o(\sigma)t_1}\max[E_1(\sigma) - E_2(\sigma),0], \quad \sigma \le \sigma_v$$

11

with the boundary conditions

$$P(0,t) = -Y(0)\ddot{f}(t) = 0$$

$$U(\sigma_V) = Y'(\sigma_V)\dot{f}(t) = 0$$

That is, the left boundary is a free surface, and the solid-vapor interface is (nearly) fixed.

The impulse is defined as

$$I_B = \int_0^\infty P(\sigma_V,t)\,dt$$

$$= -\int_0^\infty \ddot{z}\,dt$$

$$= \dot{z}(\sigma_V,0) - \dot{z}(\sigma_V,\infty)$$

$$= [\dot{f}(0) - \dot{f}(\infty)]Y(\sigma_V)$$

Since

$$\dot{f}(0)Y(\sigma) = \dot{z}(0,\sigma) = \int_0^\sigma U(\sigma',0)\,d\sigma' \quad \text{and since}$$

$$U(\sigma,0) = 0 \text{ and } f(0)Y(\sigma) \neq 0 \quad \text{implying } Y(\sigma) \neq 0,$$

$$\dot{f}(0) = 0.$$

Since the analytical form of f is a monotonically increasing function, (without boundary)

$$\dot{f}(\infty) = \sqrt{\frac{3t_1}{2\beta}} \ .$$

Thus

$$I_B = -\sqrt{\frac{3t_1}{2\beta}}\ Y(\sigma_V) \ .$$

12

Defining

$$F(\sigma) = \frac{4}{3} \frac{\beta}{\rho_o(\sigma)t_1} \max[E_1(\sigma) - E_2(\sigma), 0],$$

Equation (8) with $U(\sigma_v) = 0$ B.C. implying $Y'(\sigma_v) = 0$ becomes

$$Y'(\sigma) = -\int_{\sigma_v}^{\sigma} \frac{F(\sigma')}{Y(\sigma')} d\sigma'$$

and $P(0,t) = 0$ B.C. implying $Y(0) = 0$ gives

$$Y(\sigma) = \int_0^{\sigma} d\sigma'' \left[\int_{\sigma''}^{\sigma_v} \frac{F(\sigma')}{Y(\sigma')} d\sigma' \right].$$

For $\sigma \geqslant \sigma_v$ one can interchange the order of integration, since the integral is not a function of σ'' ,

$$Y(\sigma_v) = \int_0^{\sigma_v} \frac{\sigma' F(\sigma')}{Y(\sigma')} d\sigma' \tag{9}$$

Equation (9) can be solved numerically by an iteration technique, but the standard BBAY equation states that the average value of Y over the interval 0 to σ_v is given by $Y(\sigma_v)/\alpha^2$. Thus substituting the average for $Y(\sigma')$,

$$[Y(\sigma_v)]^2 = \alpha^2 \int_0^{\sigma_v} \sigma' F(\sigma') d\sigma' ,$$

and

$$I_B = \alpha \sqrt{\frac{3t_1}{2\beta}} \sqrt{\frac{4}{3}\frac{\beta}{t_1}} \left\{ \int_0^{\sigma_v} d\sigma' \frac{\sigma'}{\rho_o(\sigma')} \max[E_i(\sigma')-E_f(\sigma'), 0] \right\}^{\frac{1}{2}}$$

or simplifying

$$I_B = \alpha \left[2 \int_0^{\sigma_v} \frac{\sigma'}{\rho_o(\sigma')} [E_i(\sigma') - E_f(\sigma')] d\sigma' \right]^{\frac{1}{2}} \tag{10}$$

It is then shown that for reasonable forms of $E_i(\sigma)$, $1 \leqslant \alpha^2 \leqslant 2$; hence α is chosen to be 1.2.

13

The form of the BBAY formula (although not the coefficient) may be derived by considering a snowplow model. At a point a distance x into the expanded material, which corresponds to m mass units, the velocity of the Δm mass is lower than in the Whitener form, since it pushes on the mass ahead of it. Thus the kinetic energy is $\frac{1}{2} mv^2 = (E_i - E_f)\Delta m$, and the square of the momentum contribution at a point is

$$(mv)^2 = 2m(E_i - E_f)\Delta m$$

Thus the total impulse squared is

$$I^2 = \int_0^x 2m (E_i - E_f) \, dm$$

and the impulse is just

$$I = \left\{ 2 \int_0^x m(E_i - E_f) \, dm \right\}^{\frac{1}{2}}$$

which, except for the coefficient α is the BBAY formula.

2. Use of Analytical Expressions

Both the Whitener and BBAY formulas contain an adjustable parameter $E_f(x)$ that corresponds to the internal energy of the final state. There are, in general, two ways in which this may be obtained.

a. Final Energy as Polynomial of Deposited Energy

The first way, which has had some success, is to plot experimental impulse data and a family of lines of calculated impulse with E_f the parameter. This produces a plot such as shown in Figure 2.

14

Impulse (arbitrary units)

E(1)

E(2)

E(3)

— calculated impulse

+ data

$E^{(1)} < E^{(2)} < \ldots$

0   1   2   3

Fluence (Arbitrary Units)
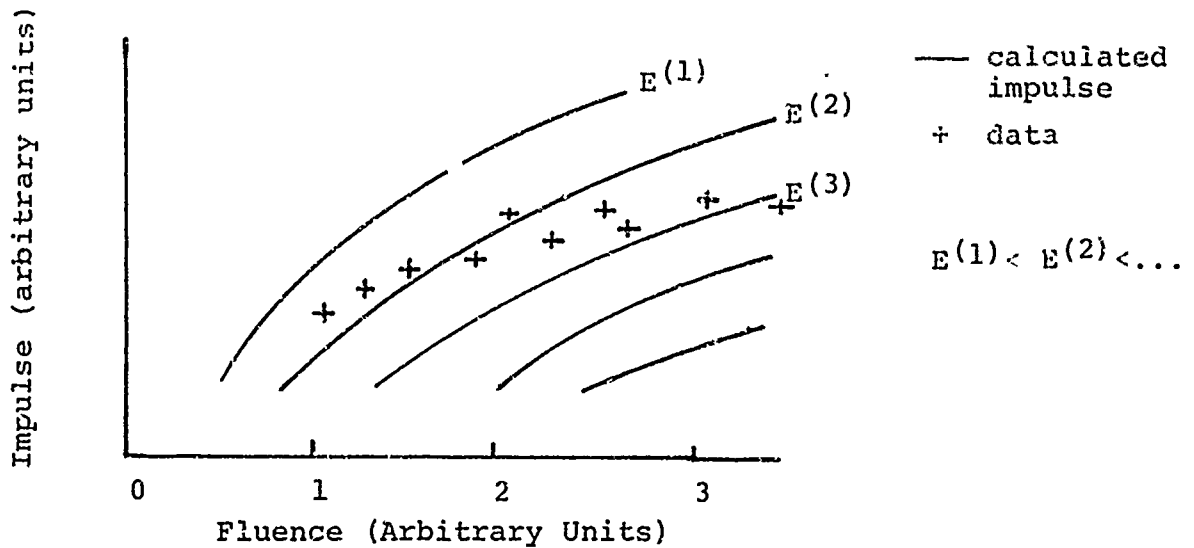
FIGURE 2.   TYPICAL CALCULATED IMPULSE WITH E_f PARAMETER
AND IMPULSE DATA

Using such data, one can obtain a least-squares fit to the
final energy density as a function of the initial (deposited) energy
density, assuming a polynomial form. For each data point, the depth of
material removal is measured (or estimated by the temperature at
which the tensile strength goes to zero). Assuming that this is
constant, or taking an average value, one has the minimum final
energy E_o. Then for each data point, one has

$$I^2 = K \int_0^{x(E^*)} x(E_i(x) - E^*)dx = K \int_0^{x(E_o)} x\left[(E_i(x) - E_f(E_i(x)))\right] dx$$

where E^* is the apparent final energy, obtained by interpolating
impulse between lines of constant E_f. Rearranging,

$$-\int_{x(E^*)}^{x(E_o)} xE_i(x)dx - E^* \frac{[x(E^*)]^2}{2} = -\int_0^{x(E_o)} xE_f(E_i(x))dx$$

For the kth data point, call the left-hand side (LHS) $-D_k$.

15

Assuming

$$E_f = \sum_{j=0}^{m} \alpha_j E_i^j \ ,$$

where

$$\alpha_o \equiv E_o$$

and defining for the kth data point

$$J_{nk} \equiv \int_o^{x(E_o)} x[E_k(x)]^n \, dx \ , \quad n = 0, m \ ,$$

i.e., m+1 quantities

$$RHS = -\sum_{j=0}^{m} \alpha_j J_{jk} \ .$$

Using the standard definition of a least-squares fit, the system of m equations (m < N, the number of data points) for the α_j is

$$(M_{ij})(\alpha_j) = (\beta_i) \ , \quad i,j = 1,m \ ,$$

where the elements of column vector β_i are ($\alpha_o = E_o$, $J_{ok} = 0.5 \, x^2(E_o)$)

$$\beta_i = \sum_{k=1}^{N} (D_k - E_o J_{ok}) J_{ik} \ ,$$

and the elements of the symmetric m by m matrix M_{ij} are

$$M_{ij} = \sum_{k=1}^{N} J_{ik} J_{jk} \ .$$

Thus the solution, (symbolically), is given by

$$\alpha_j = (M_{ij})^{-1} (\beta_i) \ .$$

This solution, of course, does not require that the data points have the same deposition profile, so that data from widely varying sources may be used together, provided only that E^* and $x(E^*)$ can be obtained. For this least-squares fit to be useful over large ranges of energy, large amounts of reliable data or considerable faith in extrapolation is required, for the value of impulse is certainly related to the value of E_f.

b. Freezing (McCT) Model for Final Energy

The alternative method for obtaining E_f, and the way required when data are lacking or uncertain, is to construct a model for the final state of the partially condensed gas, and derive a functional form for E_f (E_i). The most successful of the models has been the McCloskey-Thompson model. This model is discussed in some detail below.

It is known (Reference 7) that at some point in the isentropic expansion of gas, the composition freezes. The distance between the condensing droplets becomes large, requiring a longer interval to reach thermodynamic equilibrium. When this time interval becomes long with respect to the time associated with hydrodynamic motion, condensation stops, and the composition remains fixed.

The McCloskey-Thompson (McCT) model assumes that the composition stays fixed at the intersection of the isentrope with the triple line. This, of course, is a useful assumption, since pressure and temperature are constant on the triple line as the specific volume changes. Their derivation then proceeds as follows:

Consider a solid heated instantaneously. The initial energy and entropy are given by

$$E_i = E_\ell (V_o, T_t) + C_{v\ell} (T_i - T_t)$$

(11)

$$S_i = S_\ell (V_o, T_t) + C_{v\ell} \ln\left(\frac{T_i}{T_t}\right)$$

for $C_{v\ell}$ a constant. Denoting E_o and S_o as the constant (base) energy and entropy, and evaluating them at the normal melting temperature (which is, in general, near the triple temperature) one can solve for S_i (E_i) by eliminating T_i in Equation (11) and obtain

$$S_i = S_o + C_{v\ell} \ln\left(1 + \frac{E_i - E_o}{C_{v\ell} T_o}\right)$$

(12)

If the final state is on the triple line,

$$S_f = x S_o + (1-x) S_{vo}$$

(13)

$$E_f = x E_o + (1-x) E_{vo} .$$

18

Eliminating x, the liquid fraction, and solving for the final entropy,

$$S_f = S_o + \frac{S_{vo} - S_o}{E_{vo} - E_o} (E_f - E_o)$$

since

$$\frac{\Delta S_{\ell-g}}{\Delta E_{\ell-g}} \simeq \frac{\Delta S}{\Delta H} = \frac{1}{T_o}$$

that is, the change in enthalpy for a constant pressure phase transition is nearly the change in internal energy, the final entropy is given by

$$S_f = S_o + \frac{1}{T_o} (E_f - E_o) \; .$$

Equating the initial and final entropies for the isentropic expansion,

$$E_f = E_o + C_{v\ell} T_o \ln \left(1 + \frac{E_i - E_o}{C_{v\ell} T_o} \right) \; .$$

Approximating $C_{v\ell} T_o$ to E_o, the final form is given by

$$E_f = E_o \left[1 + \ln \left(\frac{E_i}{E_o} \right) \right] \; . \tag{14}$$

The maximum initial energy for which this formula is valid is given by

$$E_{vo} = E_o \left(1 + \ln \frac{E_{i-max \; \ell}}{E_o} \right)$$

or

$$E_{i\,max\,\ell} = E_o \exp\left[\frac{E_{vo} - E_o}{E_o}\right] \qquad (15)$$

and the minimum energy E_o.

c. Non-Freezing Model for Final Energy

One may reinterpret the McCT model and remove the essentially arbitrary choice of freezing the composition at the triple temperature and pressure. For materials that are in a liquid state at ambient pressure, the pressure of the triple point is less than atmospheric—water, for example, and a triple point pressure of 5 Torr. Most impulse experiments are performed at 1 atm or less. It is improbable that impulse measurements made at 1 atm or less will change with ambient pressure.[*] Thus we may replace the assumption that the composition freezes by the assumption that the material expands to ambient pressure, which is taken to be the triple point pressure.

Since material vapors generally follow the ideal gas law at pressures less than 1 atm, one can easily calculate the final entropy and internal energy.

For
$$E_i > E_{i\,max}$$

$$E_f = E_{vo} + C_{vg}\,(T_f - T_o) \qquad (16a)$$

$$S_f = S_{vo} + C_{vg}\,\ell n\left(\frac{T_f}{T_o}\right) + R\,\ell n\left(\frac{v_f}{v_o}\right) \qquad (16b)$$

where by applying the assumption

$$P_f = P_o = \frac{RT_f}{v_f}$$

---

[*] Considering that most of the impulse is generated in 1 μsec or so, 1 bar-μsec corresponds to 1 tap.

20

Setting $E_{vo} - C_{vg} T_o = E_{sub}$ and solving Equation (16a) for V_f,

$$V_f = \frac{R(E_f - E_{sub})}{C_{vg} P_o} \quad .$$

Then Equation (16b) becomes

$$S_f = S_{vo} + C_{vg} \ln \left[\frac{E_f - E_{sub}}{C_{vg} T_o} \right] + R \ln \left[\frac{E_f - E_{sub}}{C_{vg} T_o} \right] \tag{17}$$

Equating Equations (17) and (12), replacing $C_{v\ell} T_o$ with E_o, and $C_{vg} T_o$ with $E_{vo} - E_{sub}$

$$\ln \left(\frac{E_f - E_{sub}}{E_{vo} - E_{sub}} \right) = \frac{C_{v\ell}}{R\beta} \ln \left(\frac{E_i}{E_o} \right) - \frac{S_{vo} - S_o}{R\beta} \quad ,$$

or

$$E_f = E_{sub} + \left(E_{vo} - E_{sub} \right) \left(\frac{E_i}{E_o} \right)^{C_{v\ell}/R\beta} \exp \left(- \frac{\Delta S}{R\beta} \right)$$

where

$$\beta = \frac{C_{vg}}{R} + 1 \quad .$$

If one makes the additional replacements that $E_{sub} \simeq L$, $\Delta S = L/T_o$, where L is the change in enthalpy between liquid and vapor at the melt temperature,

$$E_f = L + (E_{vo} - L) \left(\frac{E_i}{E_o} \right)^{C_{v\ell}/R\beta} \exp \left(- \frac{1}{\beta} \frac{L}{RT_o} \right). \tag{18}$$

By construction, Equation (18) has the property that E_f (for $T_f = T_o$ so $L = 0$ and $E_i = E_o$) $= E_{vo}$, so that it joins smoothly with Equation (15).

Since for $E_i > E_{i\ max\ell}$, E_f is an increasing function, the use of a constant value as suggested in the McCT reference will give results that predict a larger impulse at high initial energy densities.

C. HYDRODYNAMIC CODES

The analytical expressions discussed in this section do not deal with the shape of the stress wave propagated into the remaining solid material. If this stress wave shape is required, one must solve the hydrodynamic equations of motion and conservation. In addition, as was seen in the BBAY derivation, a relation between pressure, volume, and internal energy--an equation of state--is required. In these codes, then, it is the equation of state that determines the impulse and pressure history, so that a study of impulse calculation with hydro-codes is a study of the various equations of state.

1. One-Phase Equations-of-State

In a restricted range of initial energy densities, one-phase equations have been used successfully in predicting the impulse and, in fact, the transmitted stress profile obtained by quartz gauge measurements (Reference 9). For maximum internal energy densities such that the vapor pressure is less than a few bars, equations of state generated from Hugoniot (shock compression) data with two modifications are used. First, for elastic-plastic codes, the yield stress goes to zero as internal energy approaches the enthalpy of a melting solid. Second, and more important, the tensile strength goes to zero as the energy approaches the melt enthalpy. If this tensile strength is exceeded at a point, the pressure is set to zero there, and the material is presumed to have spalled at that point. In this way a net momentum is imparted to

22

the solid material; the transmitted stress profile is nearly all compressive.

If appreciable vapor is formed, however, impulse calculations with a one-phase equation of state result in predictions of impulse lower than that measured. It is apparent, then, that for higher energy densities, a description of the vapor phase is important.

2. Two-Phase Equations of State

Two-phase equations of state in current use include the Tillotson equation (Reference 10), its modification (Reference 11) and the PUFF equation (Reference 12). These have the following in common: (1) there is a line in internal energy-volume space that separates the two equations of state (these lines are compared in Figure 3), and (2) the two equations-of-state forms are usually continuous at the boundary and have continuous first derivatives. The equations are given in Table I.

The PUFF and modified Tillotson equations have, among other parameters, one called E_s. The standard Tillotson equation uses $E_s = 0$. At large expansions, (η small) the dominant term of both equations is of the form with P equal to a constant $(E-E_s)$, the γ-law gas form. Thus to fit experimental data would, in general, require the use of E_s as an adjustable constant, as was the case in the BBAY and Whitener expressions. The PUFF and modified Tillotson equations give reasonably similar results for impulse when the same value of E_s is used. This is, of course, in agreement with the results of the BBAY derivation, which showed that impulse was independent of the value of γ in the γ-law gas equation of state. They are also both in reasonable agreement with the BBAY calculations using a constant E_s.
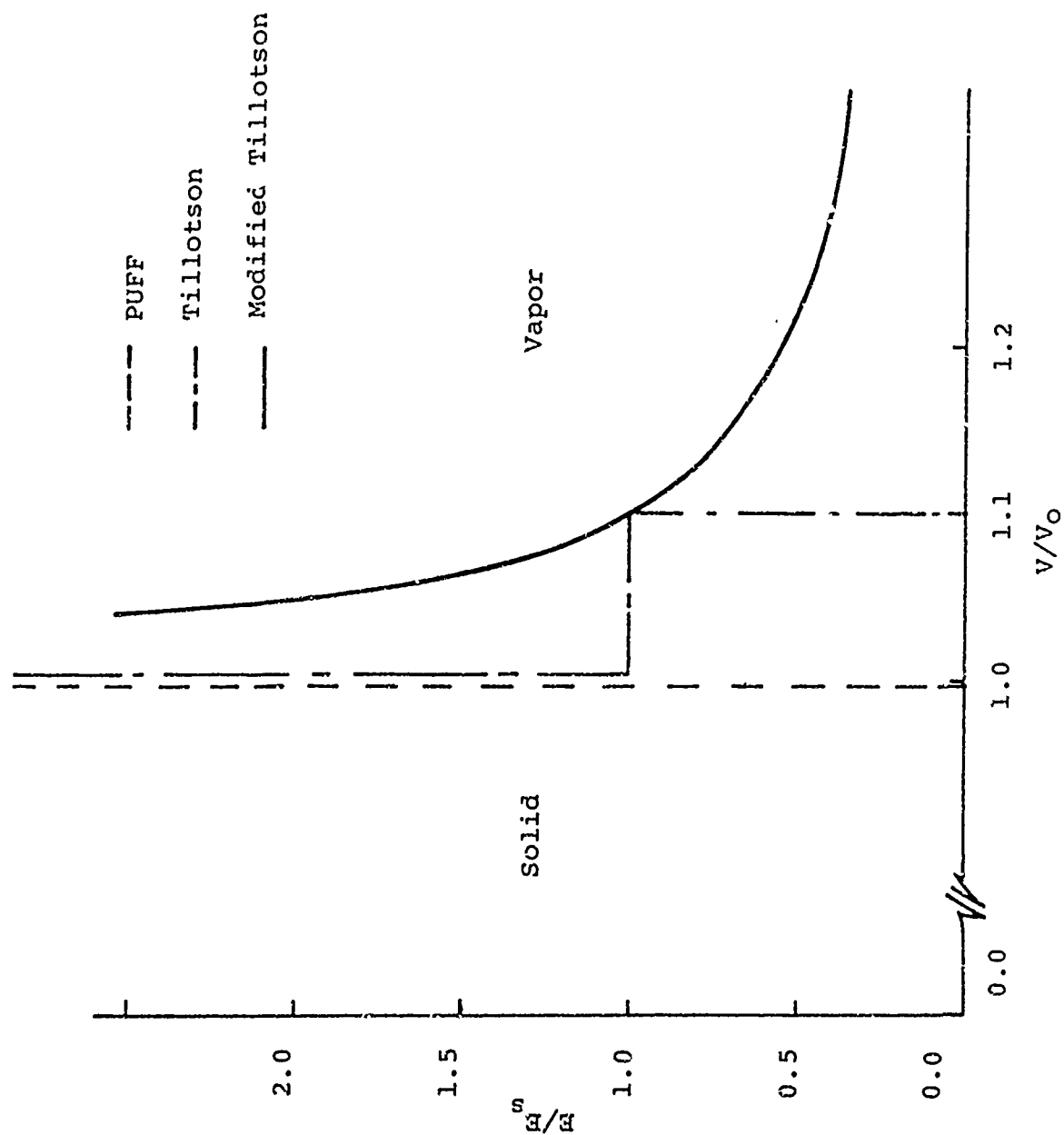
23

FIGURE 3   PHASE DIVISIONS OF VARIOUS EQUATIONS OF STATE
(IN ALUMINUM)

24

TABLE I

TWO-PHASE EQUATIONS OF STATE

Name	Solid	Vapor	Expression
PUFF	x		$C\mu + D\mu^2 + S\mu^3 + Gn E$
		x	$\eta[H + (G-H)\eta^{\frac{1}{2}}]\left\{E - E_s\left[1 - \exp\left[\frac{C}{GE_s}\frac{1}{\eta}(1-\frac{1}{\eta})\right]\right]\right\}$
TILLOTSON	x		$\left[a + b\left(\frac{E}{E_o}\frac{1}{\eta^2}+1\right)^{-1}\right]E\eta + A\mu + B\mu^2$
		x	$aE\eta + \left[bE\eta\left(\frac{E}{E_o}\frac{1}{\eta^2}+1\right)^{-1} + A\mu \exp \beta\left(1-\frac{1}{\eta}\right)\right]\exp$
			$\left[-\alpha\left(1-\frac{1}{\eta}\right)^2\right]$
MODIFIED TILLOTSON	x		$\left[a + b\left(\frac{E}{E_o}\frac{1}{\eta^2}+1\right)^{-1}\right]E\eta + A\mu + B\mu^2$
		x	$a(E-E_s)\eta + G \exp R,$

$$G = aE_s\eta + b\left(\frac{E}{E_o}\frac{1}{\eta^2}+1\right)^{-1}E\eta + (A\mu+B\mu^2)\exp(\beta R),$$

$$R = -\alpha\left(\frac{E_s}{E}\right)^2\left(\frac{\mu E}{\mu_s E_s}-1\right)^2$$

If the solid is heated so that the entropy is greater than
the critical point entropy, the distinction between phases becomes
quite arbitrary; properties change continuously between the "phases."
Thus a two-phase equation of state makes good physical sense for
this high energy density regime since pressure changes smoothly
along an isentrope. If a choice were necessary among the three
equations offered, the modified Tillotson equation would be best,
as the solid Gruneisen coefficient, Γ, varies from the ambient
value of approximately 2.0 to the asymptotic Thomas-Fermi gas value
of 0.5 as the internal energy increases. Whether the form chosen
for interpolation at reference density $0.5 + (\Gamma - 0.5)/(E/E_o + 1)$
is correct is not relevant. The equation is incorrect where the
interpolation form is important.[*]

The inaccuracy of the two-phase equations is greatest where
the mixed-phase (liquid-vapor) region is important. The calculation
of pressure in this region is difficult, particularly if there is a
requirement for thermodynamic consistency and agreement with the
limited equation of state data that is available.

_____

[*]Another equation of state with a temperature-dependent Gruneisen
was used in Reference 14 to fit Hugoniot data on porous media at
pressures up to several megabars. It does have the slight dis-
advantage of being implicit in energy (temperature is the dependent
variable).

D. MONK CODES

MONK codes (Reference 13) generate a two-phase equation of
state by an approach that differs from other two-phase equations.
Instead of selecting equation-of-state forms that join smoothly, the
MONK code uses separate forms for each phase and joins them by
equilibrium thermodynamics.

The vapor equation is one suggested in Reference 16 as being
useful for moderately high pressures (hundreds of kilobars) and at
near liquid densities. It is a virial expansion of the form

$$P = \frac{RT}{V} \left[1 + \frac{B(T)}{V} + \frac{C}{V^2} + \frac{D}{V^3} + \frac{E}{V^4} \right]$$

where B(T) is the second virial coefficient of Lennard-Jones (6-12)
potential and C, D, and E are constants. The coefficients are
given as dimensionless ratios of the co-volume. The temperature
and volume scaling parameters are related to the two constants in
the 6-12 potential, which are the depth of the potential well and
the radius of the minimum potential. They may in turn be estimated
from the critical point temperature and volume.

The solid form is separated into two parts corresponding to
nuclear and electronic contributions. The latter, of course, are
only dominant at high temperatures. The nuclear form uses the
compressibility and its pressure derivative, the coefficient of
thermal expansion, and the specific heat at constant volume to
obtain the nuclear contributions to pressure and internal energy
as functions of temperature and volume. This solid form is assumed
to hold throughout the solid and liquid phases.

27

It is desired, then, to make a transition between the forms at high mass densities and temperatures and to make it thermodynamically consistent. For phase changes at constant volume and temperature, the thermodynamic potential is the Helmholtz free energy. Since the expression for the Helmholtz free energy, $F = E - TS$, can be written for both phases, equating F_g and F_s defines a line $T_{sub}(V)$. For the MONK code, then, the transition between the two phases is a line in the $T - V$ plane, but a region in the $E - V$ plane. In this region, the pressure is calculated by a simultaneous solution of the three equations

$$\eta_g\, E_g + (1 - \eta_g)\, E_s = E$$

$$\eta_g\, V_g + (1 - \eta_g)\, V_s = V$$

$$P_g\, (T_{sub}\,(V),\, V_g) = P_s\, (T_{sub}\,(V),\, V_s) = P$$

As with the other two-phase equations, the formulation is only appropriate for high energy densities, where the release adiabats remain in the vapor phase.

For adiabats that intersect the mixed phase region (see Figure 4), however, it is necessary to construct the boundary of that region.
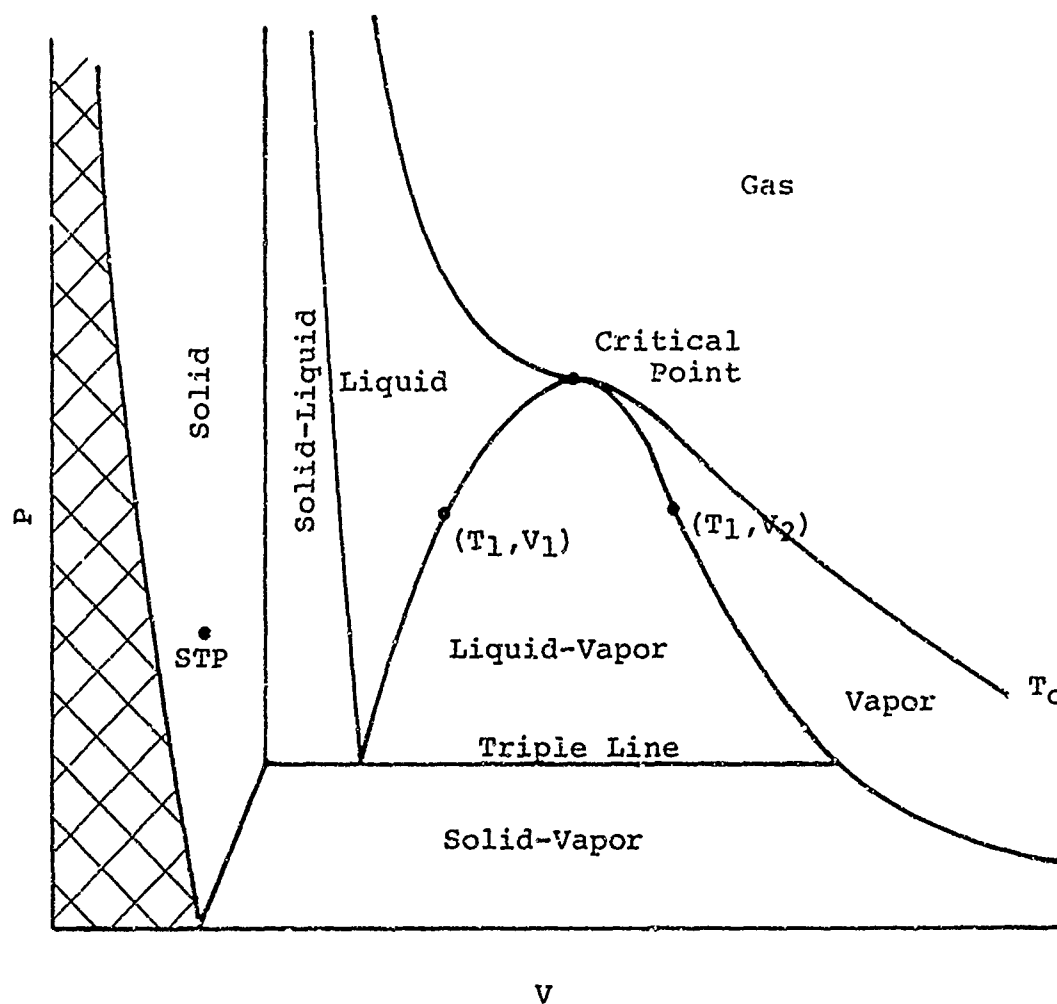
28

FIGURE 4.   TYPICAL PHASE DIAGRAM

E. MIXED-PHASE REGIONS

1. Construction of the Mixed-Phase Boundaries

The boundaries of the mixed-phase region (liquid-vapor) may be
established by the following arguments.

For any N-component mixture we may write the change in Gibbs
free energy, G, as

$$dG = \frac{\partial G}{\partial P}\bigg)_{T,n_i} dP + \frac{\partial G}{\partial T}\bigg)_{P,n_i} dT + \sum_{i=1}^{N} \frac{\partial G}{\partial n_i}\bigg)_{P,T,n_{j\neq i}} dn_i + \qquad (19)$$

now

$$\frac{\partial G}{\partial n_i}\bigg)_{P,T,n_{j\neq i}} = \mu_i \ ,$$

the chemical potential, and for equilibrium between two phases of
the same element at constant total mass, $N = 2$, $\mu_1 = \mu_2$, $dn_1 = -dn_2$,
so that Equation (19) reduces to $dG = VdP - SdT$. However, along
a line where T is equal to a constant in the mixed-phase region,
P is constant, so $dG = 0$.

Thus, at temperature T_1, we know that $G_{solid} (T_1, V_1)$
$= G_{gas} (T_1, V_2)$ (the subscripts refer to Figure 5). The gas and
solid energies may be placed on the same scale by assuming that
ΔH, P_b, and T_b are known at a boiling point. Then since
$\Delta H = \Delta E + \Delta(PV)$, and for standard boiling point data, P is constant,
$\Delta H_b = \Delta E_b + P_b \Delta V$.

30

V_g is found from the expression P_g $(T_b, V_g) = P_b$; V_s is found similarly.

If E_g can be represented functionally as E_g $(T,V) + E^O$

$$\Delta H_b = E_g(T_b, V_g) + E^O - E_s (T_b, V_s) + P_b (V_g - V_s) ,$$

or

$$E^O = \Delta H - E_g (T_b, V_g) + E_s (T_b, V_s) - P_b (V_g - V_s) .$$

The gas and solid entropies are placed on the same scale by the equality of Gibbs free energy at the boiling point.

$$G \equiv F + PV \equiv E - TS + PV$$

again write the gas entropy as S_g $(T, V) + S^O$.

$$E_g (T_b, V_g) + E^O - T_b [S_g (T_b, V_g) + S^O] + P_b V_g =$$

$$E_s (T_b, V_s) - T_b [S_s (T_b, V_s)] + P_b V_s$$

$$\Delta E + P_b \Delta V + T_b S_s (T_b, V_s) - T_b S_g (T_b, V_g) = T_b S^O$$

$$S^O = \frac{\Delta H_b}{T_b} + S_s (T_b, V_s) - S_g (T_b, V_g) .$$

With the energy and entropy scales correct, the dome may be constructed by solving two implicit equations for selected V_g

$$P_s (T, V_s) = P_g (T, V_g)$$

$$G_s (T, V_s) = G_g (T, V_g) ,$$

for V_g expressed in the two unknowns T and V_s.[*]

---

[*]The convergence of the iteration may be speeded by using the Clapyron equation $dP/dT = \Delta H/T\Delta V$ to estimate the temperature T.

2. Calculation of Pressures

Several difficulties can be foreseen in the calculation of pressure; they are described below.

a. Mixed-Phase Region

Clearly there are two possible states near the condensed vapor line. Consider the following two experiments for ambiguity.

For the first experiment, put the solid material in a rigid container with a piston at one end, not attached to the material. Heat the material to less than the 1 atm melting point, and then expand the volume at constant temperature. At some volume, the piston will no longer touch the solid, and the pressure on the piston is just the saturation pressure (or vapor pressure) at that temperature. This then describes a material under the liquid-vapor dome.

The second experiment, however has a piston that is rigidly attached to the face of the material. As the piston is "expanded," the material will go into tension until it spalls. Then the pressure increases rapidly to the proper point in the liquid-vapor dome, and expansion continues as in the first experiment.

With these two experiments in mind, then, the "mixed-phase" logic in a hydro-code becomes: if the material was condensed, compute pressure as solid (P_s). If P_s is less than the spall strength (at temperature T), compute as mixed phase. If the material was a gas, or if one surface of the zone is free, compute as mixed phase.

32

b. Gas-Phase Region $(V \geqslant V_{crit}, T > T_{dome} (V))$

In this region there is no difficulty, provided the negative B coefficient (the viral coefficient) does not dominate the pressure equation at the input volume. One determines that the substance is a gas by the condition

$$E_{in} \geqslant E_g \left[T_{dome} (V_{in}), V_{in} \right]$$

and computes the pressure by solving the implicit equation $E_g (T, V_{in}) = E_{in}$ for the temperature. The pressure, P, is given by $P = P_g (T, V_{in})$.

c. High-Density Region $(V < V_{crit}, T > T_{dome} (V))$

One problem in this region is the description of the "transition" from a solid to a high-density gas. Both this problem, and one other--that there is no guarantee that the liquid-vapor dome will close at a critical point--can be traced to the parameters in the solid equation of state.

If the liquid-vapor dome closes, certainly the intersection of the solid and gas lines is a place where the Helmholtz free energies are equal, and continuity arguments would say that the line of equal Helmholtz free energies, the T_{sub} line, can be drawn from V_{crit}, at least part way to V_o. Extrapolating this line, making sure that $E_g > E_s$ would give a reasonable transition line. Remember, however, that pressures computed near this artificial transition line may not be accurate.

If the dome does not close, there is no assurance that the T_{sub} line can be drawn at all. There are two ways in which nonclosure may occur. The first, in which there is a coexistence region extending to high temperatures, is shown in Figure 5.
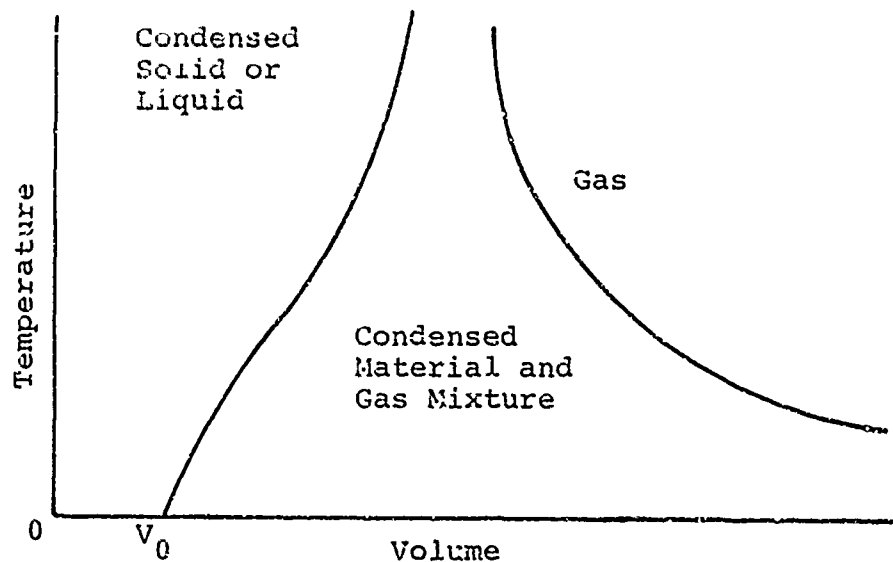
33

FIGURE 5. TWO-PHASE DIAGRAM FOR SUBSTANCE WITH
NO CRITICAL TEMPERATURE OR VOLUME

Figure 5 may well represent the condition of equilibrium
between a solid and its vapor--there may be no critical point.
This is certainly reasonable behavior, and may be pictured
crudely as a combination of the vapor pressure increasing
rapidly with temperature, and the stiffening of a material at
high pressures beginning to overcome the softening associated
with high temperatures.

The second way in which nonclosure occurs, however, is
the case where there is no temperature at which the Gibbs free
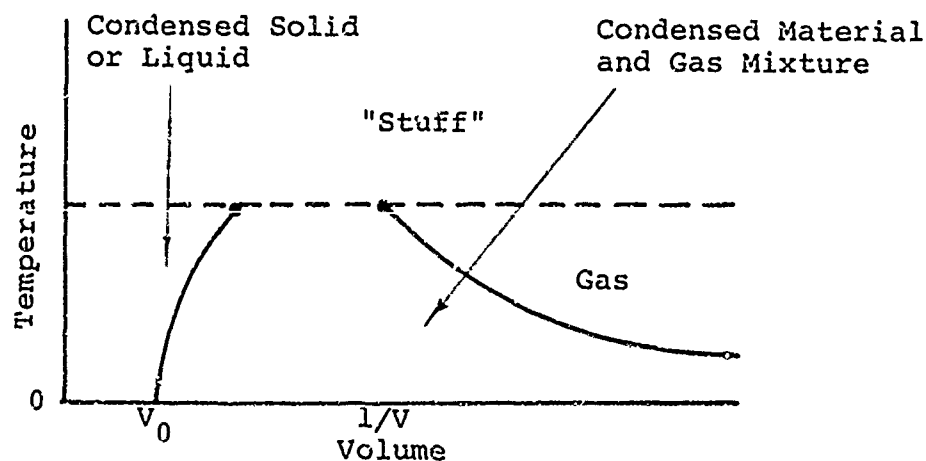energies equal, shown in Figure 6.

FIGURE 6. TWO-PHASE DIAGRAM FOR SUBSTANCE WITH CRITICAL
TEMPERATURE BUT NO CRITICAL VOLUME

34

The second case (shown in Figure 6) is more difficult to interpret physically, but the implication is that since the two phases may not coexist above a certain temperature, there must be a third (separate) phase there. Since it is assumed at the outset that there are but two phases, it is clear that the difficulty is with the separate equations of state.

In the first case, there is no real problem in calculating pressure. There is no transition between solid and vapor phases in the high-density region, only the mixed phase. In the second case, a T_{sub} line is sought starting at the maximum solid volume by the standard MONK procedure. If there is no solution, a temperature on the V_s line where $E_g \geq E_s$ is used. From that point an extrapolation is made on a T_{sub} line at constant temperature (if possible) keeping $E_g > E_s$.

d. Alternative Methods

Certainly one alternative to the methods outlined above would be to use a solid equation-of-state form that guarantees the proper behavior at the critical point. This was the method taken in Reference 15. The difficulty with (and simplicity of) this method is that there are no adjustable parameters that can be used to accommodate shock wave data. It would seem, then, that this approach is not fruitful for use in a hydro-code.

e. Consistency Check

After the boundary of the dome has been calculated, one severe test of consistency is that the critical volume and temperature are related to the co-volume, B_o, and temperature ε/k:

$$\varepsilon/k = 0.77 \; T_{crit}$$

$$B_o = 0.75 \; V_{crit}$$

which are initially estimated to scale the gas equation of state. If these are very different from the values used previously, the dome should be redrawn, using revised values of the co-volume and characteristic temperature.

Major areas of doubtful values of pressure using this formulation would be near the transition line, T_{sub}, and near the critical point, particularly if the liquid-vapor dome does not close with zero slope. It should, however, do well with condensation and boiling phenomena for $P < P_{crit}$, and for release adiabats with $P > P_{crit}$ at $V = V_{crit}$.

f. Approximate Version

An approximation to the above description can be made as follows. Inside the liquid-vapor dome, the two relations that follow hold rigorously.

$$\eta_g (E_g - E_s) + E_s = E$$

$$\eta_g (V_g - V_s) + V_s = V$$

(20)

Figure 7 shows the reduced vapor pressure as a function of reduced temperature. This is, for aluminum, using the critical constants $T_c = 6842^{\circ}K$, $P_c = 4.7$ kbar, and the vapor pressure form of Reidel (Reference 15),

$$P_v = \exp\{\alpha \ln t + C[36/t - 35 - t^6 + 42 \ln t]\}$$

36

In further analysis, this will be given by the power law

$$P_v = t^{6.85} \tag{21}$$

which holds reasonably well down to 10 bar (the line in Figure 7).

Assuming the gas to be ideal, the condition

$$T = \frac{E_g - E_o}{3/2 \, R} \tag{22}$$

holds, where E_o is the internal energy of the gas at zero temperature and may be calculated by a known boiling point at, for example, 1 atm.

The condition

$$P_v(t) = \frac{RT/V_g}{P_c} \tag{23}$$

serves to determine the gas volume at the "dew point." If we assume further that

$$T = E_s/3R \tag{24}$$

i.e., small volume changes in the solid, $T \gtrsim 2\theta$, we may make the further approximation that

$$\eta_g = \frac{V - V_s}{V_g - V_s} = \frac{V}{V_g} + \left(\frac{V}{V_g} - 1 \right) \left[\frac{V_s}{V_g} + \left(\frac{V_s}{V_g} \right)^2 + \cdots \right] \simeq \frac{V}{V_g} \tag{25}$$

Then solving Equation (20) for an η_g, we obtain

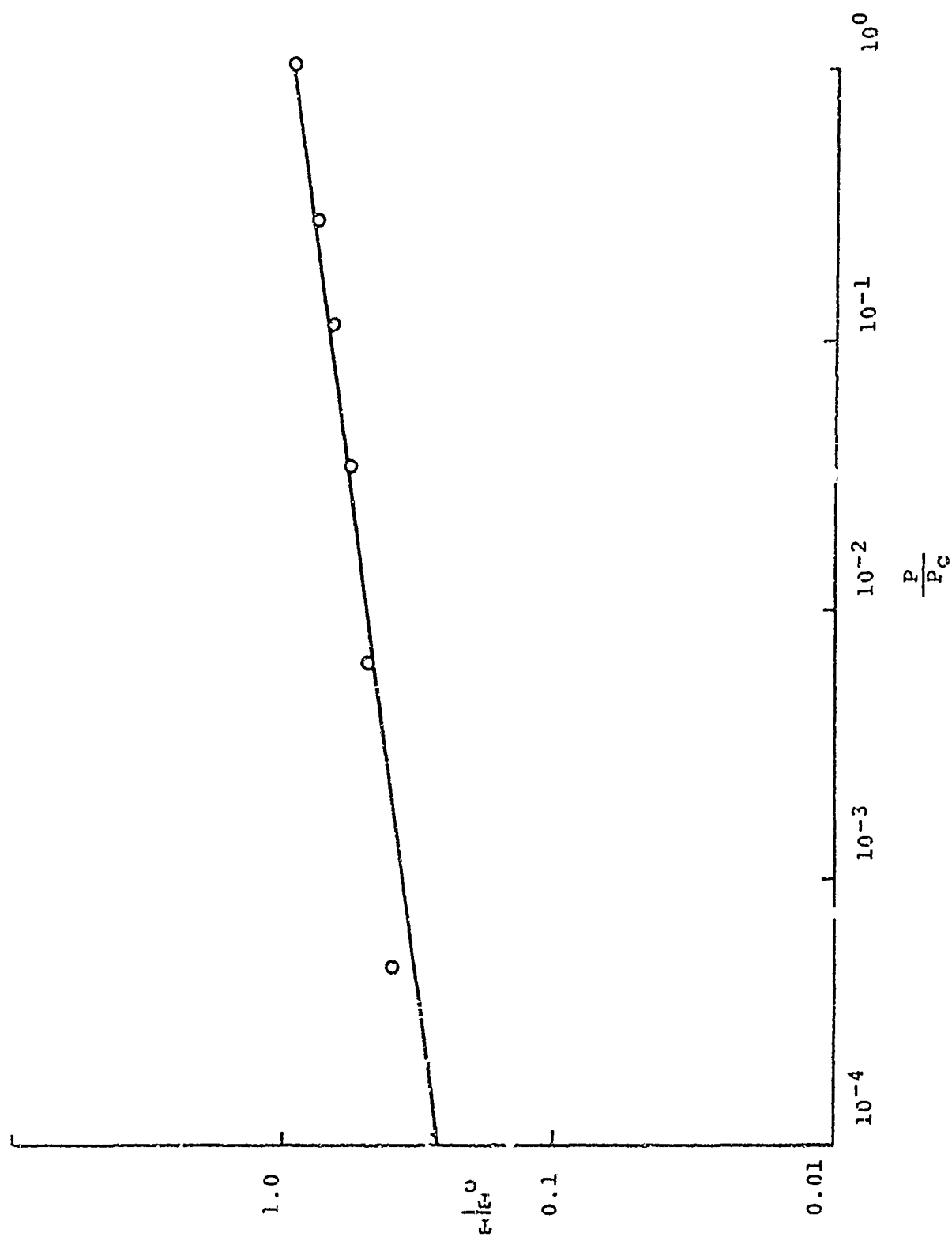$$\eta_g = \frac{E - E_s}{E_g - E_s} \tag{26}$$

37

FIGURE 7   REDUCED VAPOR PRESSURE OF ALUMINUM

38

Conditions of Equations (22) and (24) give

$$E_s = 3R \frac{(E_g - E_o)}{3/2\ R} = 2\ (E_g - E_o)$$

Defining $U \equiv E_g - E_o$, $E_s = 2U$, Equation (26) becomes

$$\eta_g = \frac{E - 2U}{U + E_o - 2U} = \frac{E - 2U}{E_o - U} \tag{27}$$

Using Equations (21) and (23) and solving for V/V_g,

$$\frac{V}{V_g} = \frac{P_c\ P_v}{RT} = \frac{P_c\ (t)^{6.85}}{RT}$$

Substituting Equation (22) for T, and defining $U_c \equiv 3/2\ RT_c$

$$\frac{V}{V_g} = \frac{P_c}{R}\ \frac{3/2\ R}{U}\ V\ \left(\frac{U}{3/2\ RT_c}\right)^{6.85}$$

$$= P_c\ \frac{3}{2}\ \frac{V}{U} \left(\frac{U}{U_c}\right)^{6.85} \tag{28}$$

Substituting Equation (28) into (25) and equating to (27)

$$P_c \left(\frac{U}{U_c}\right)^{6.85} \frac{3}{2}\ \frac{V}{U} = \frac{E - 2U}{E_o - U}$$

which on rearranging becomes

$$P_c \left(\frac{U}{U_c}\right)^{6.85} = \frac{2}{3}\ \frac{U}{V}\ \frac{(E - 2U)}{(E_o - U)} \tag{29}$$

Let the value of U which satisfies (29) be U^*. Then in the mixed phase region

$$T = \frac{U^*(E,V)}{3/2\ R}$$

$$\frac{1}{V_g} = P_c\ \frac{3}{2}\ \frac{1}{U^*}\ \left(\frac{U^*}{U_c}\right)^{6.85} = \frac{3}{2U^*}\ \text{LHS Equation (29)}$$

$$P = \frac{RT}{V_g} = \text{LHS Equation (29).}$$

To relate this to a hydro-code calculation, let the solid pressure be the standard polynomial, P_s, and determine the approximate mixed-phase region by $P_s\ (E,V) < P_V\ (E/3\ RT_c)$ and if $V/V_g < 1$ then use the mixed-phase logic.

It should be noted that the approximations restrict the range of validity to $T < T_{crit}$, so that, for aluminum $E_{inc} \lesssim 1500$ cal/g.

F. CONCLUSIONS

With these calculational techniques, one can predict impulse in materials over a wide range of deposited energies. For high doses, so that the impulse is vapor dominated, the two-phase equations of state in hydro-codes and the BBAY expression are reasonably effective. For low doses, the spall-dominated region, the BBAY formula is inappropriate. It will be shown in Section III that the Whitener formula with an appropriate model for E_f is effective in predicting impulse when proper account is made of the deposition time. In addition, one-phase equations of state predict impulse and the transmitted stress pulse.

Equations of state in current use were found not to account for the effects of vapor-liquid equilibria. A modification and

40

extension of the existing McCloskey-Thompson model of vapor-liquid equilibrium effects used in BBAY integral expressions was presented. Finally, a technique for generating a thermodynamically consistent model for vapor-liquid equilibria was derived, and a simplified version suitable for direct use in hydrodynamic codes was shown.

To select the appropriate models for predicting impulse, one needs a basis of empirical information, and the experiments described in the following sections were performed at Physics International on the 738 Pulserad to provide such data. Since accurate electron energy deposition profiles are required for all of the models, diagnosis of the electron energy spectrum, current, and mean angle of incidence are necessary for the electron transport (Monte Carlo) codes used to calculate the deposition profile. Section III presents the diagnostic techniques used for obtaining this information, as well as the techniques for measuring impulse.

SECTION III

EXPERIMENTAL TECHNIQUES

A. INTRODUCTION

The first phase of the experimental portion of this program consisted of: (1) demonstrating a system of electron-beam diagnostics to determine time-dependent energy deposition in the test material as a function of depth, and (2) demonstrating a reliable technique to measure electron-beam-generated impulse. The methods used to accomplish these two goals are discussed in this section. The beam diagnostics include diode voltage and current monitors to define the electron beam at injection into the drift chamber, as well as Rogowski coils and a Faraday cup to measure the net and primary beam currents at the sample location. For beam intensities sufficiently low to preclude material spallation or vaporization, graphite calorimeters and thin foil-aluminum dosimeters were used to measure electron-beam intensity and in-depth energy deposition.

The ability to determine energy deposition as a function of material depth utilizing voltage and current monitor outputs in conjunction with mean angles of incidence of beam electrons was independently verified by the following comparisons:

1. Calculated energy deposition with that measured in thin-foil dosimeters.
2. Measured electron number transmission with that derived from calculated deposition profiles.
3. Measure rear-surface pressure in a material with a well-known equation of state with that from calculated energy deposition and beam intensity.

Preceding Page Blank

Metallic guide cones instrumented with Rogowski coils were employed to transport electron beams. The geometry of the guide was designed to shape the beam intensity so that the fluence (cal/cm^2) is uniform over the guide-cone exit area (approximately 3.0 cm^2). The Rogowski-coil instrumentation provides a measurement of the net current of the beam, which can be empirically related to the primary current. This relationship has been used to predict beam intensity (fluence) within ±10%.

A ballistic pendulum was used to measure electron-beam-generated impulse in test materials. The important features of the pendulum were a variable transformer recording the time history of the pendulum deflection and a low damping co-efficient of oscillation. The guide cone and pendulum system are mounted on an inertial platform used to decouple the measuring apparatus from "bulkhead shock" caused by the shock generated in the oil switch between the transmission line and the diode. The beam guides have been slotted to minimize the effects of anode debris on pendulum motion.

B. DIAGNOSTIC TECHNIQUES

Electron-beam parameters are monitored in two regions: the diode and the drift chamber. Diode diagnostics provide a time history of electron accelerating voltage and current at the anode plane. This information is required to determine the characteristics of beam production in the diode.

Following injection of the beam into the drift chamber, the characteristics of beam transport to the sample location can alter the energy spectrum generated in the diode. Addi-

44

tional diagnostics in the drift chamber are, therefore, required
to specify the electron-beam environment at the sample location.
Strong evidence indicates that the voltage waveform is not signi-
ficantly altered for beam transport lengths up to 30 cm. However,
the primary current-pulse shape can undergo substantial change
caused by losses of electrons with high transverse energy com-
ponents as well as by the "erosion" of the beam front (Reference 3).

What follows is a description of the monitors in the diode
and drift chamber regions, including their calibration and function
to determine electron-beam characteristics.

1.   Diode Diagnostics

The Physics International 738 Pulserad was used to generate
the high energy density states required in this program. The
pulser consists of a 38-stage Marx generator, used to pulse-charge
an 8.5-ohm, oil-filled coaxial transmission line. The trans-
mission line is switched into the load, a field emission diode
consisting of a $2\frac{1}{2}$-in. diam, 600-needle cathode, and a thin,
0.00025-in.-thick, aluminized Mylar anode. Diode impedance is
variable between $\approx$ 1 and $\approx$ 8 ohms by adjustment of the anode-to-
cathode spacing, such that at typical pulse charge voltages of
3.5 mV, the machine output can be varied in the 200 keV to 1 MeV
mean electron energy range at current levels of 250 to 125 kA,
respectively.

The diode diagnostics consist of a resistive voltage divider
attached to the cathode, a self-integrating loop current monitor,
and an open loop dI/dt monitor. These three monitors are situated
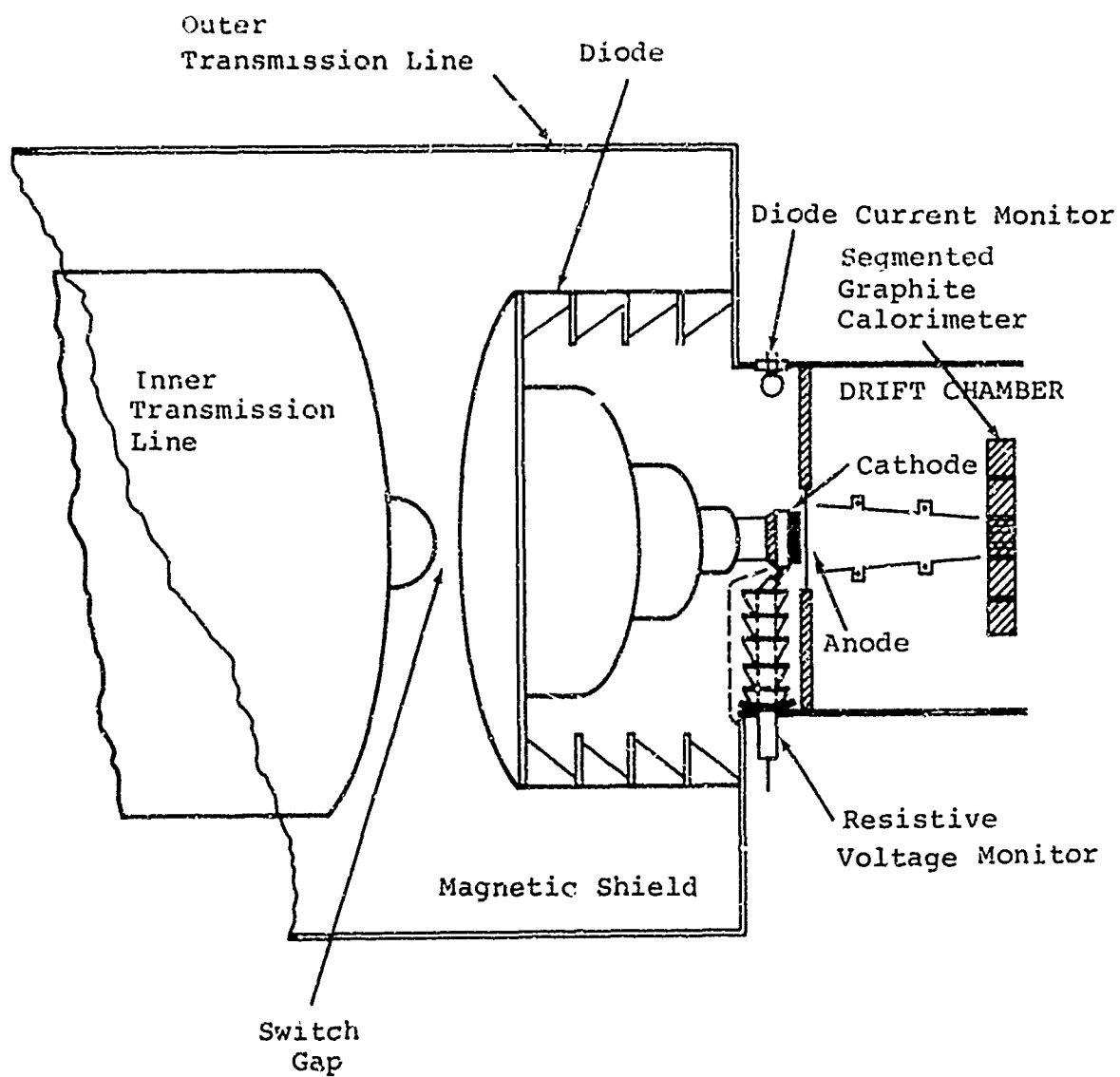in the diode (Figure 8). Their construction is described in
Reference 2.

45

Outer
Transmission Line

Diode

Diode Current Monitor

Segmented
Graphite
Calorimeter

DRIFT CHAMBER

Inner
Transmission
Line

Cathode

Anode

Resistive
Voltage Monitor

Magnetic Shield

Switch
Gap

FIGURE 8. ANODE-CATHODE REGION AND PLACEMENT OF DIAGNOSTICS

46

These monitors were calibrated as follows:

1. The diode current monitor was calibrated by firing the beam into a Faraday cup located at the anode plane at both high (200 kA) and low (50kA) current levels. The diode voltage monitor was calibrated at 25 kV with an external voltage source.

2. The inductive pickup of the voltage monitor (Figure 9c) was measured for anode-cathode shorted shots and correlated with the signal from the dI/dt probe located in the diode region. The dI/dt probe was then used as a measure of the inductive component of the diode voltage signal on all subsequent shots. This component was subtracted from the voltage monitor signal (Figure 9d) to yield the actual accelerating voltage pulse shape (Figure 9e).

3. A series of shots was fired into total shopping graphite calorimeters near the anode. The total beam calories deposited in the calorimeter agreed (±5%) with $\int_0^{t'''} VI\, dt$ calculated from diode voltage and current records.

2. Beam Transport

The beam in the drift chamber is controlled by metallic guide cones (Figure 10). These cones produce an extremely flat fluence distribution over the 3/4-in. exit diameter (at drift chamber pressures in the range 0.5 to 6.75 Torr) as confirmed by uniform depth cratering in aluminum, and X-ray pinhole photography of the bremsstrahlung produced in a tantalum target at the cone exit. The pinhole photographs in Figure 11 show uniform density spots corresponding to the area at the cone exit. The elliptical shape
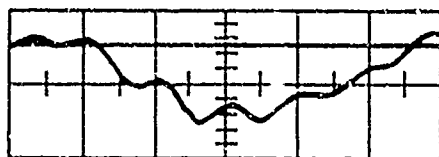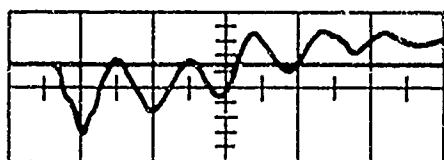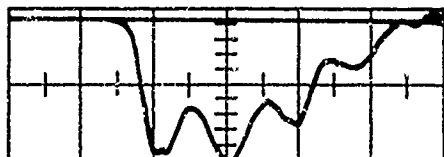
237 kA/cm

a. Current Monitor
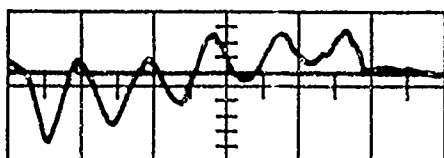
950 V/cm

b. $\frac{dI}{dt}$ Probe, $V_o(t) = \beta\frac{dI}{dt}$

275 kV/cm

c. Voltage Monitor Inductive
    Component, $V_o(t)$. (A-K
    Shorted)

275 kV/cm

d. Voltage Monitor, V (t),
    (A-K Spacing 3 mm)

275 kV/cm

e. Corrected Voltage, V (t) $- \beta\frac{dI}{dt}$

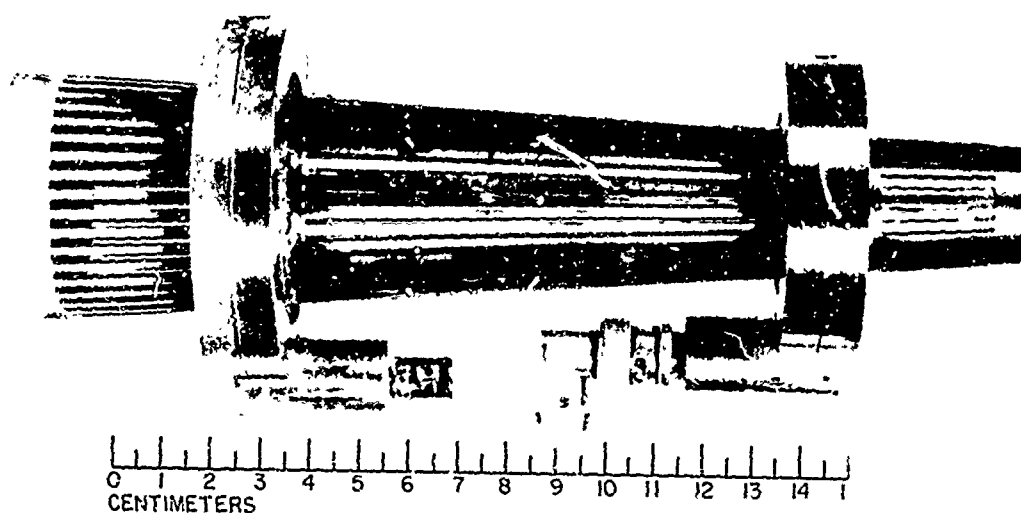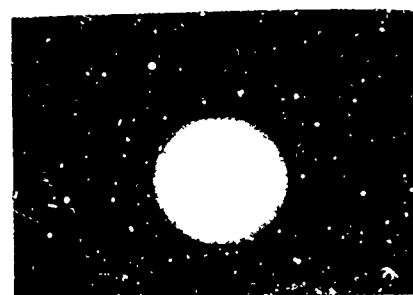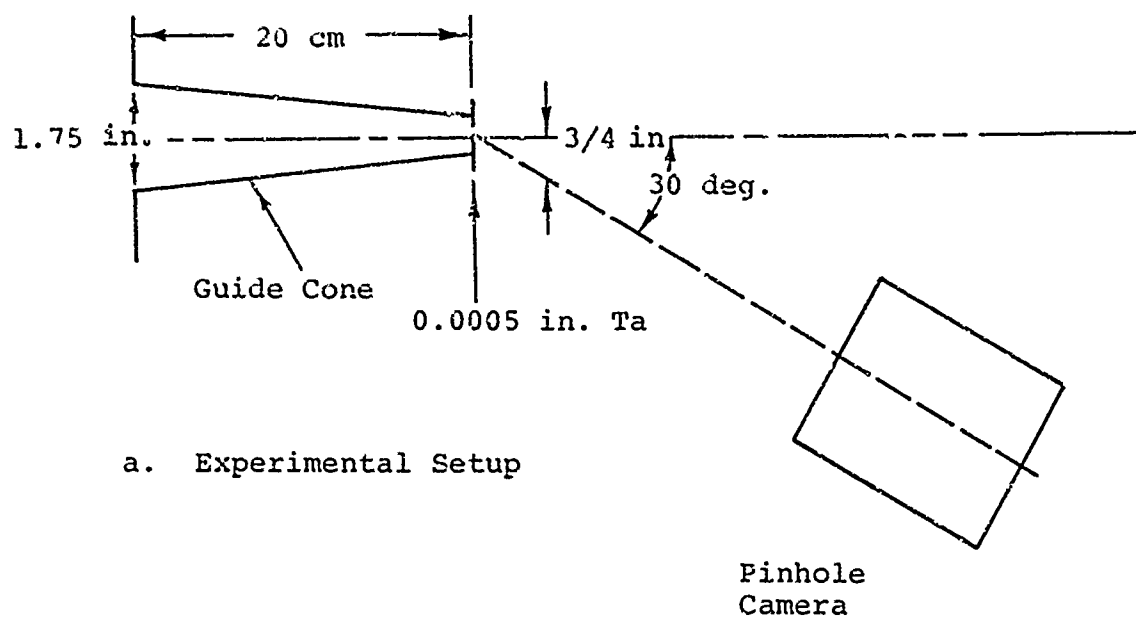FIGURE 9. DIODE DIAGNOSTIC TRACES
           (TIME SCALE = 20 nsec/cm)

48

FIGURE 10. SLOTTED ELECTRON BEAM GUIDE CONE INSTRUMENTED
WITH TWO ROGOWSKI COILS

6756

49

20 cm

1.75 in.

3/4 in.

30 deg.

Guide Cone

0.0005 in. Ta

Pinhole
Camera

a.   Experimental Setup

b.   Pinhole Photographs

FIGURE 11.   PINHOLE PHOTOGRAPHY OF CONE EXIT AREA

of the spots results from positioning the pinhole camera 30 degrees off-axis from the center line of the cone. Figure 12 shows the top and side view of an electron-beam-caused crater in an aluminum slab. The uniform crater depth confirms a uniform fluence distribution over the exit area of the cone.

The level of the uniform fluence distribution (at fluence levels low enough to preclude removal of graphite by the beam) is determined by allowing the beam to impinge on a totally absorbing (5/16-in. thick) segmented calorimeter array placed at the cone exit. The energy stopped in those blocks which are well within the projection of the exit area of the cone onto the calorimeter array (Figure 13) is divided by the frontal area of the blocks ($\frac{1}{2}$ x $\frac{1}{2}$-cm^2) to yield the fluence level (cal/cm^2).

The fluence level indicated by blocks near the circumference of the cone exit area projection is underestimated for two reasons. These blocks are not irradiated over their entire area (fluence calculations average incident calories over entire front surface of the block) and also they lie on the slope of a severe temperature gradient from the hotter blocks in the center to the colder blocks near the edge of the calorimeter array. The heat transfer is demonstrated by fluences recorded in blocks that were not irradiated (see Figure 13, Calorimeter Array). Consequently, the fluence map obtained from the calorimeter array is a poor indication of fluence uniformity.

Figure 13 shows a radial fluence distribution obtained from calorimetry incorporating a correction for irradiation of only portions of blocks along the cone circumference projection.
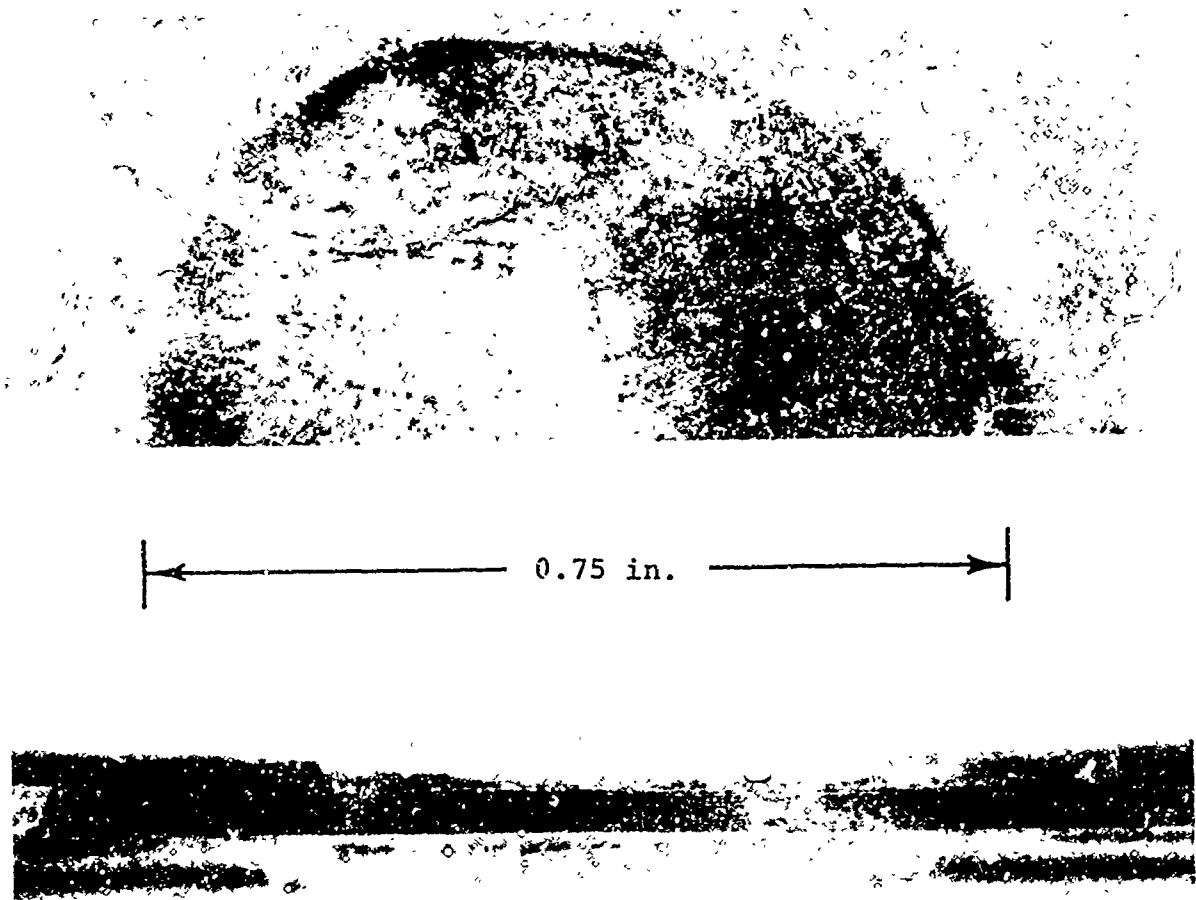
51

$\longleftarrow$ 0.75 in. $\longrightarrow$

FIGURE 12. TOP AND SIDE VIEWS OF CRATER CAUSED BY 170-keV
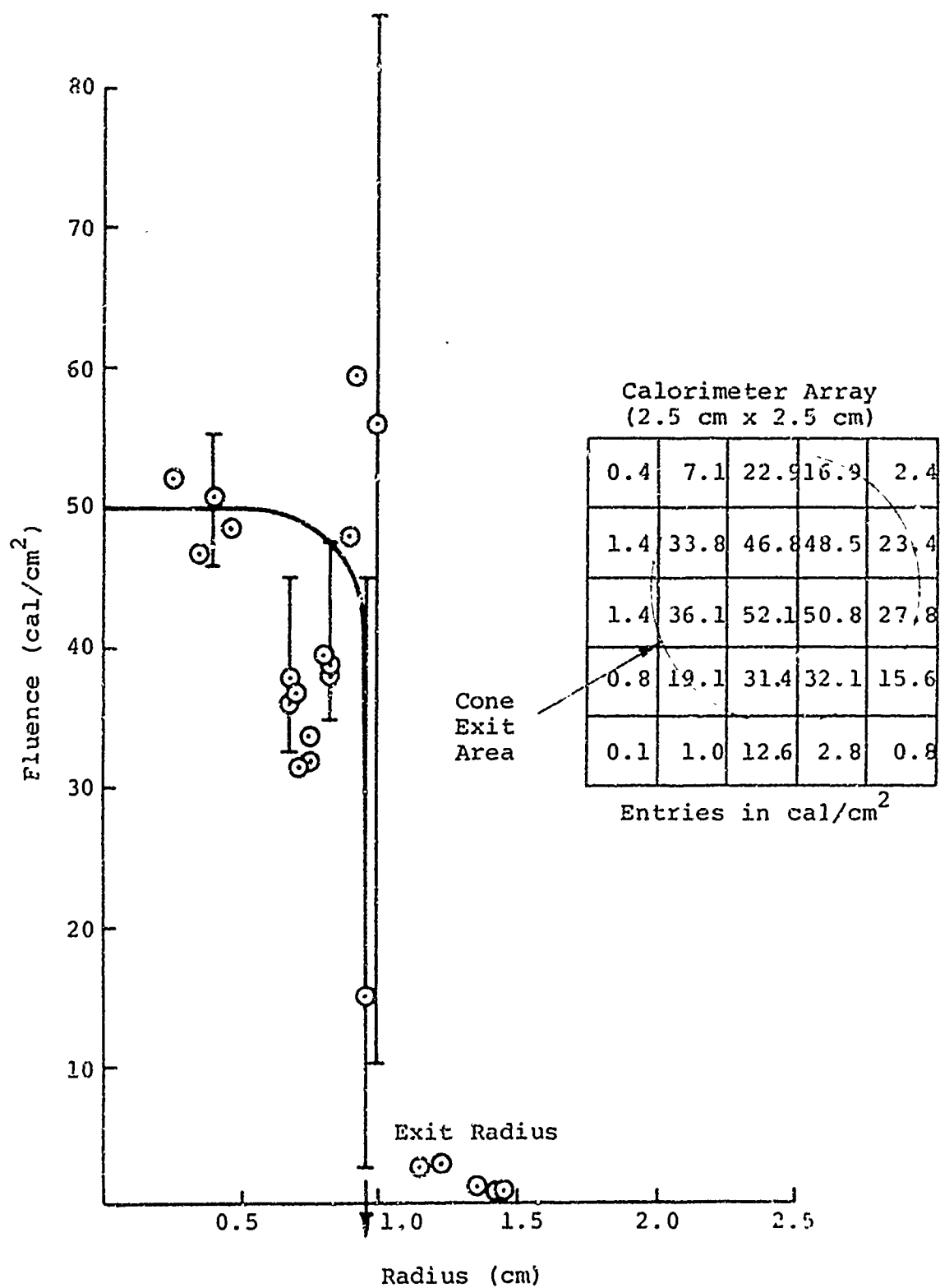ELECTRON DEPOSITION 35 cal/cm^2 FLUENCE, IN ALUMIN'M

52

FIGURE 13   FLUENCE VERSUS RADIUS IN A BEAM GUIDE CONE

53

3.   Drift Chamber Diagnostics

The beam guide cones are instrumented with two Rogowski
coils, each of which is a loosely wound torus. The Rogowski
coil is self-integrating and has a voltage output proportional
to the average flux threading all its turns. This diagnostic
measures the net current flowing through the guide cone. A
completed coil is shown in Figure 14. Neglecting any mutual
inductance between the separate turns of the Rogowski coil,
the output voltage is

$$V = \frac{R}{L} \ nA\mu_o \ \tfrac{1}{2}\pi a \quad (mks)$$

where   R = resistance of integrating resistor,

                   L = net self-inductance of the coil,

                   n = number of turns in coil,

                   A = area of a single turn,

                   a = mean radius of the torus.

In view of the approximations involved in determining the
Rogowski coil output, an empirical calibration was necessary.
A calibration fixture and fast readout system have been developed
from the following:

  1.   Fast risetime pulse generator, 10 A into 50-ohm load
       with a 2-nsec risetime.
  2.   Sampling oscilloscope, 2 mV/cm sensitivity, 0.3-nsec
       risetime.
  3.   Impedance matching load threading the coil.

A typical calibration trace on the sampling oscilloscope is
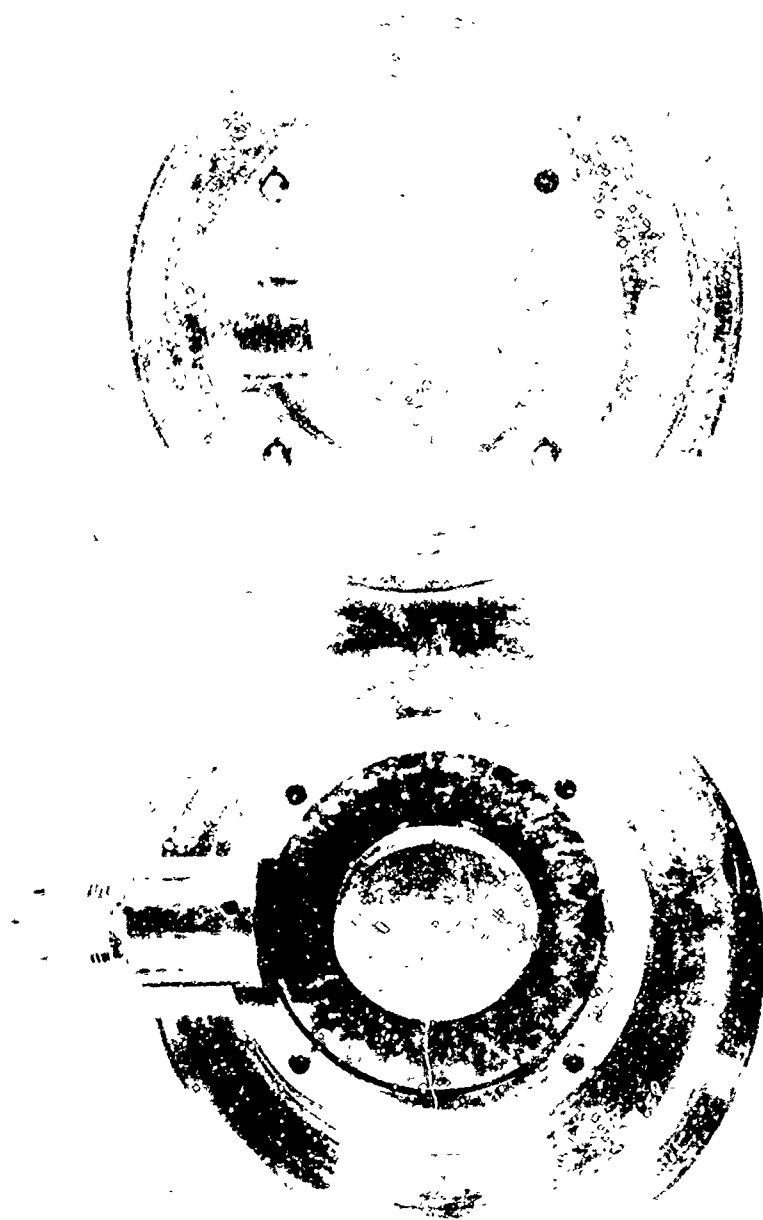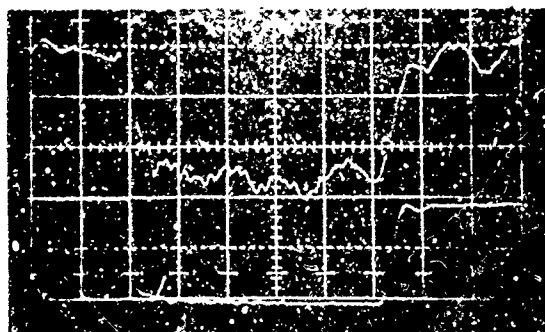shown in Figure 15a, where the upper trace is the coil output, and
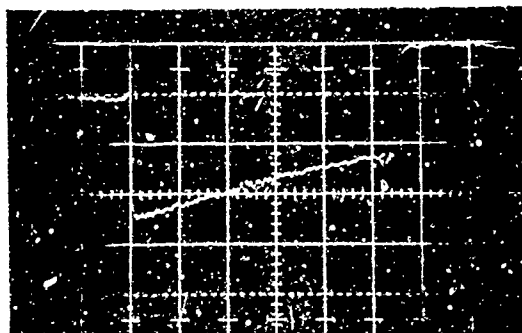
54

FIGURE 14. RO   SK

Coil Output
20 mV/cm

Input Pulse
5 A/cm

2 nsec/cm

a. Coil Response to 10-A, 10-nsec
    Input Pulse

Coil Output
20 mV/cm

50 nsec/cm

b. Coil Response to 10-A, 270-nsec
    Input Pulse

FIGURE 15. CALIBRATION TRACES FOR A 2-cm
I. I. POGOWSKI COIL (No. 15)

the lower is the input current pulse. Figure 15b shows the coil
response to a longer (270 nsec) 10-A input pulse. A summary of
the characteristics for coil 15 is given below.

COIL CHARACTERISTICS

2 cm i.d. Rogowski Coil Number 15

Risetime	0.9 nsec
Absolute Sensitivity	4.8 V/kA
Decay Constant	400 nsec

The aim of the inclusion of Rogowski coils in the beam guide
cones was the prediction of fluence levels when a sample completely
covers the cone exit area thus making fluence data collection im-
possible. A Faraday cup is used to achieve this predictive capa-
bility (Figure 16). The Faraday cup is a charge collector combined
with an integral milliohm shunting resistor and incorporates a fast
vacuum pumping system and a conical collector specifically designed
to intercept high-current, low-energy electron beams. A thin rub-
ber membrane acts as a vacuum seal in front of the collector, and
in principle, prevents the plasma formed in the beam channel from
shorting out the current path through the monitoring resistor.
Typical output signals of the Rogowski coil and the Faraday cup
are shown in Figure 17.

With I_1, I_2, and I_p^{max} defined in Figure 17, the following
empirical relation between the primary and net current for a fixed
drift chamber pressure (e.g., $K = 2.0$ at 0.5 Torr) has been ob-
served:
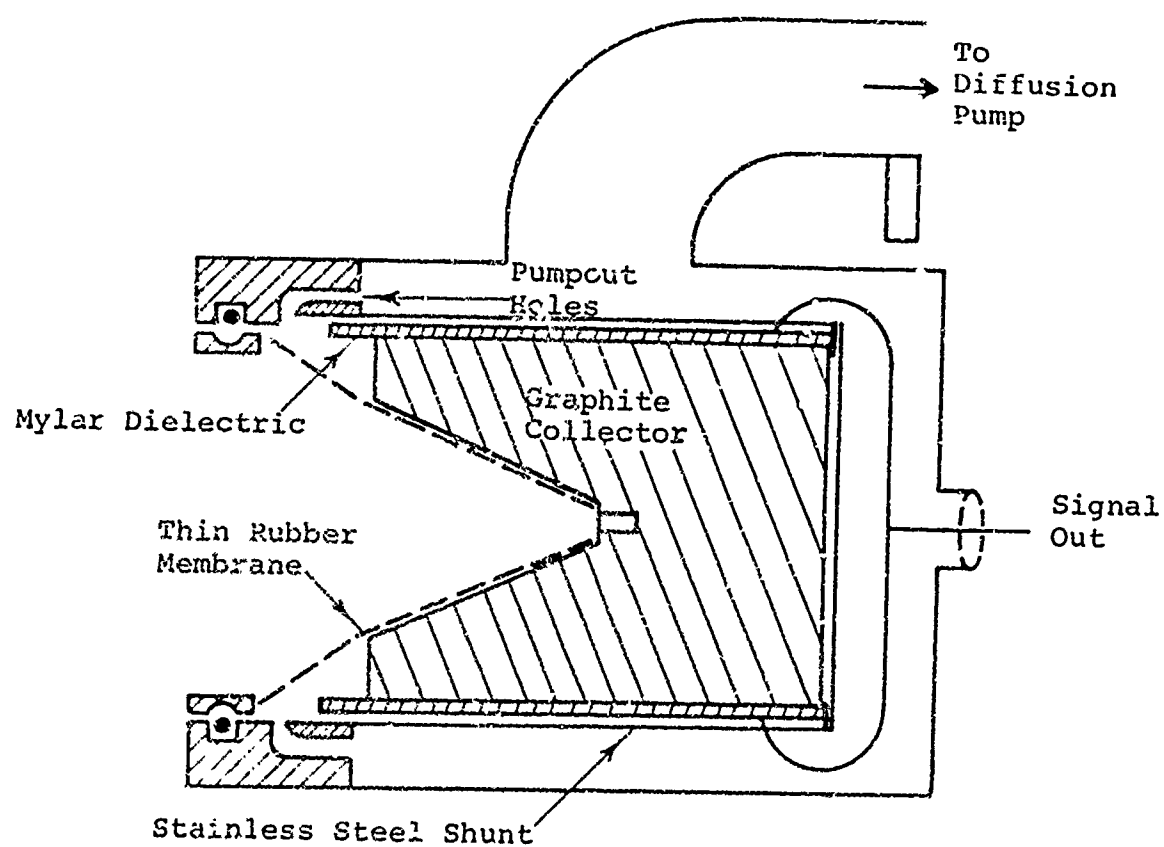
$$I_p^{max} = I_1 + k\ I_2$$
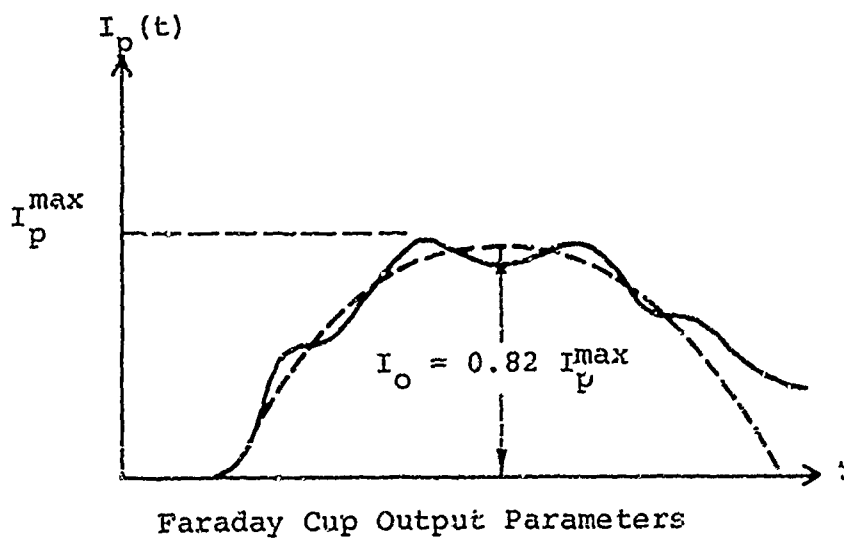
57

FIGURE 16. SCHEMATIC OF FARADAY CUP

Labels in figure:
To Diffusion Pump
Pumpout Holes
Graphite Collector
Signal Out
Mylar Dielectric
Thin Rubber Membrane
Stainless Steel Shunt

Rogowski Coil Output Parameters
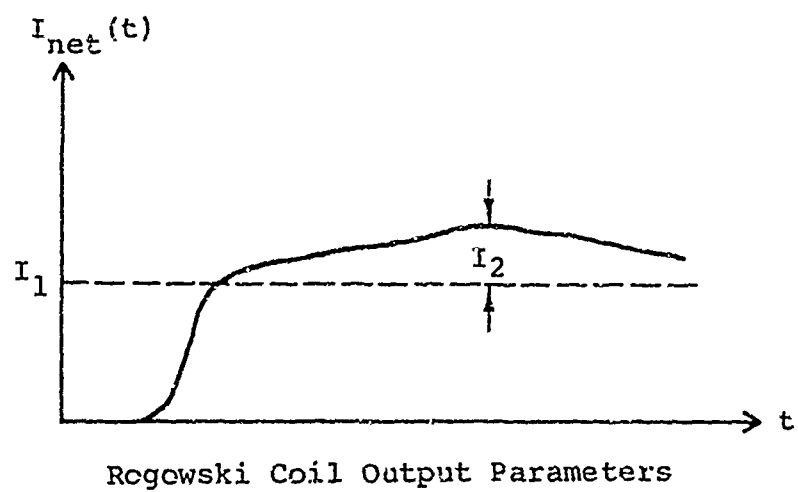

Faraday Cup Output Parameters

FIGURE 17 $I_O = 0.82\ I_p^{max} = 0.82\ (I_1 + k\ I_2)$
PARAMETER DEFINITION

59

The rms deviation in the prediction of the primary current peak amplitude is ±6% (Figure 18).

Since a Faraday cup trace of the primary current is not available during a sample irradiation shot, the time dependence of the primary current was approximated by

$$I_p(t) = I_0 \sin \frac{\pi}{c'} (t - a')$$

where

$$I_0 = 0.82 \, I_p^{max}$$

$$c' = \text{full width} = 86 \text{ nsec}$$

$$a' = \text{lag time compared with } V(t = 0) = 5 \text{ nsec}$$

The accelerating voltage, $V(t)$, from the voltage monitor trace was approximated by a trapezoid:

$$V(t) = \frac{V_1}{a} t \text{ for } 0 \leq t \leq a = 12 \text{ nsec}$$

$$V(t) = \frac{(V_2 - V_1) t - (aV_2 - bV_1)}{b - a} \text{ for } a \leq t \leq b = 50 \text{ nsec}$$

$$V(t) = \frac{V_2 (c - t)}{(c-b)} \text{ for } b \leq t \leq c = 86 \text{ nsec}$$

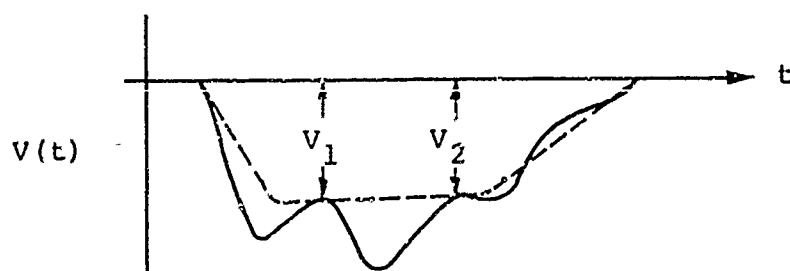where V_1 and V_2 are defined in Figure 19:
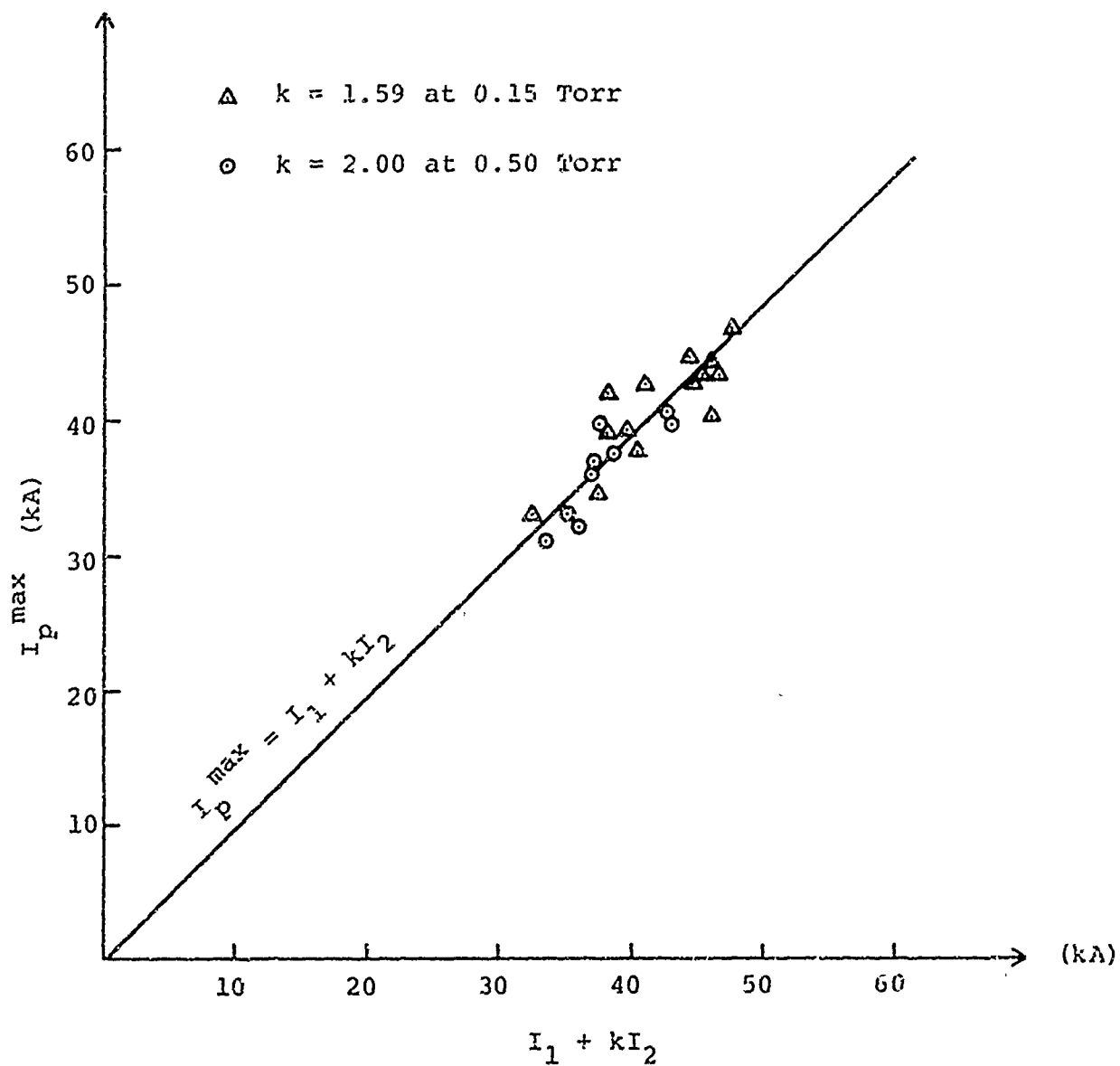

FIGURE 19.   VOLTAGE MONITOR TRACE PARAMETERS

60

FIGURE 18   MEASURED PEAK PRIMARY CURRENT, I_p^{max} VERSUS
THE $I_1 + kI_2$ CALCULATION

61

Using the approximations for $V(t)$ and $I_p(t)$ as defined above, let

$$\mathcal{K}(cal) = \frac{1}{4.186} \int_0^{\infty} V(t) I_p(t) dt = I_o(kA) [3.12 \ V_1(kV) + 7.34 \ (kV)] \times 10^{-3}$$

represent the total beam calories near the cone exit. The uniform fluence near the cone exit now permits division by the cone exit cross-sectional area giving an approximate fluence level

$$\bar{\phi}(cal/cm^2) = \frac{\mathcal{K}}{A} = I_o(kA) [1.09 \ V_1(kV) + 2.55 \ V_2(kV)] \times 10^{-3}$$

where $\quad I_o = 0.82 \ I_p^{max} = 0.82 \ (I_1 + 2.0 \ I_2)$, with

$$k = 2.0 \text{ at } 0.5 \text{ Torr}$$

$$A = 2.85 \text{ cm}^2$$

$\bar{\phi}$ depends only on parameters from the net current (Rogowski coil output) and the accelerating voltage (diode voltage monitor output). This information is available on any shot, including sample irradiation.

The results of a series of fluence shots into segmented graphite calorimeters were used to test the accuracy of the total beam calories prediction, $\mathcal{K}$. The rms deviation from the measured total beam calories, $\mathcal{K}$, in the range of 60 to 170 cal was ±10% (Figure 20). A further comparison consisted of measuring the primary beam current with a Faraday cup at the guide cone exit. The waveforms of the voltage and primary current were then used in an exact integration of $\int V(t) I_p(t) dt$ to obtain the total beam calories which were compared with $\mathcal{K}$ calculated from approximations to those waveforms. These data are also presented in Figure 20.
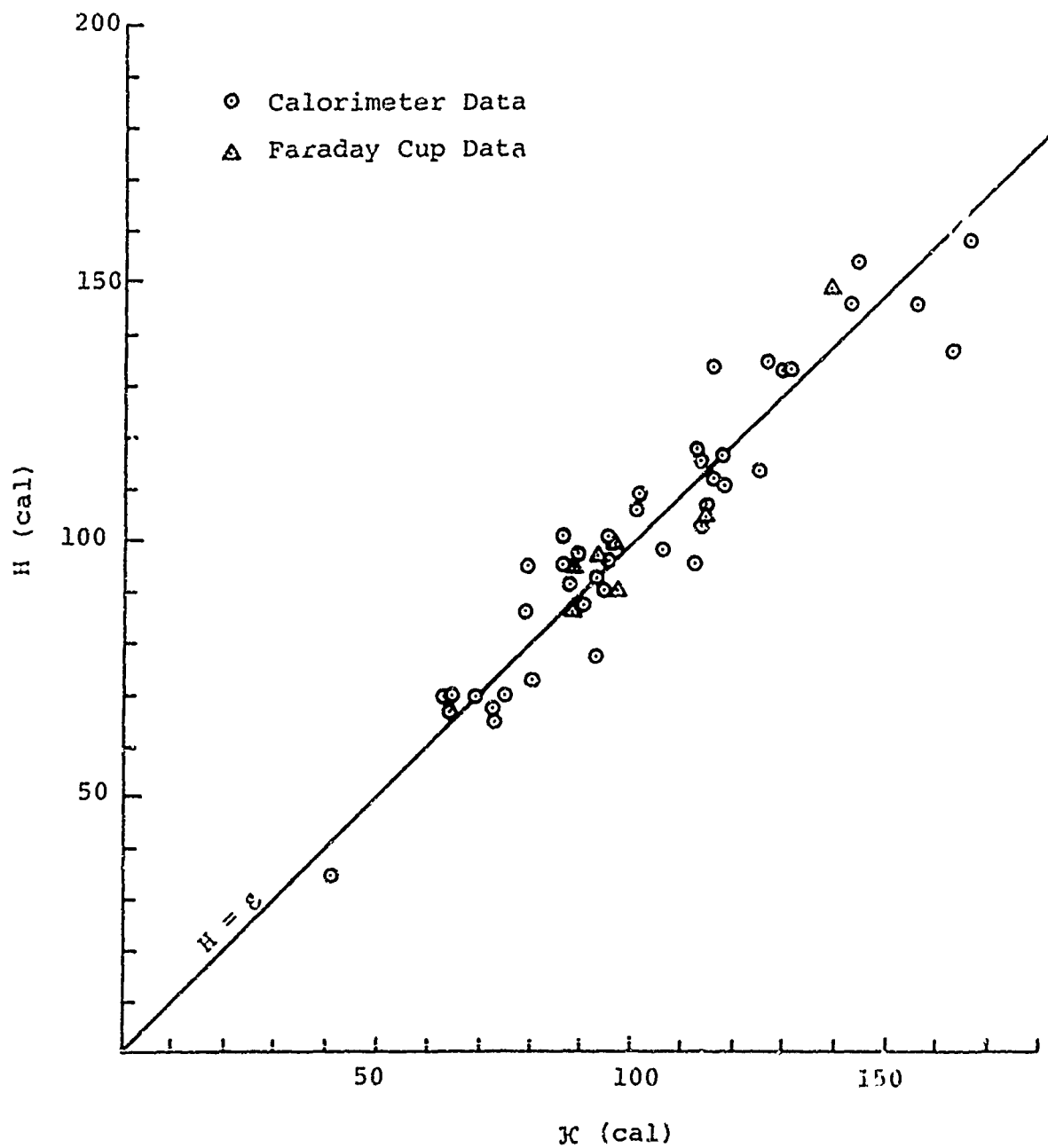
62

FIGURE 20. MEASURED TOTAL BEAM CALORIES , H VERSUS
CALCULATED TOTAL BEAM CALORIES, ℋ

63

The mean electron energy is defined as

$$\langle E \rangle = \frac{\displaystyle\int_{0}^{\infty} V(t)I(t)dt}{\displaystyle\int_{0}^{\infty} I(t)dt}$$

and $\mathcal{K} = \displaystyle\int_{0}^{\infty} V(t)I(t)dt$ with $I(t) = I_o \sin \pi/c'\ (t - a')$.

Taking advantage of the $\mathcal{K}$-approximation, the mean electron energy can be estimated by

$$\frac{\displaystyle\int_{0}^{\infty} V(t)I(t)dt}{\displaystyle\int_{0}^{\infty} I(t)dt} = 0.266\ V_1\ (kV) + 0.626\ V_2\ (kV) \qquad \langle \varepsilon \rangle$$

The correlation between $\langle E \rangle$ and $\langle \varepsilon \rangle$ can be used as a further check on the validity of the $\mathcal{K}$-approximation. Figure 21 is a plot of $\langle E \rangle$ versus $\langle \varepsilon \rangle$, when $\langle E \rangle$ was calculated from the signals of the voltage and current monitors without approximation. The rms deviation of this comparison is less than $\pm 10\%$.

C.   ELECTRON ENERGY DEPOSITION PROFILE AND SUMMARY OF BEAM
     DIAGNOSTICS

1.   Depth Dose and Electron Number Transmission Measurements

The method used to predict the deposition profile is diagramed in Figure 22. The electron beam is fired into an array of 0.003-in. aluminum foils with thermocouples attached (depth dose), to record the temperature rise. The data are translated into energy deposited in each foil, and a normalization is obtained by dividing the cal/g

64
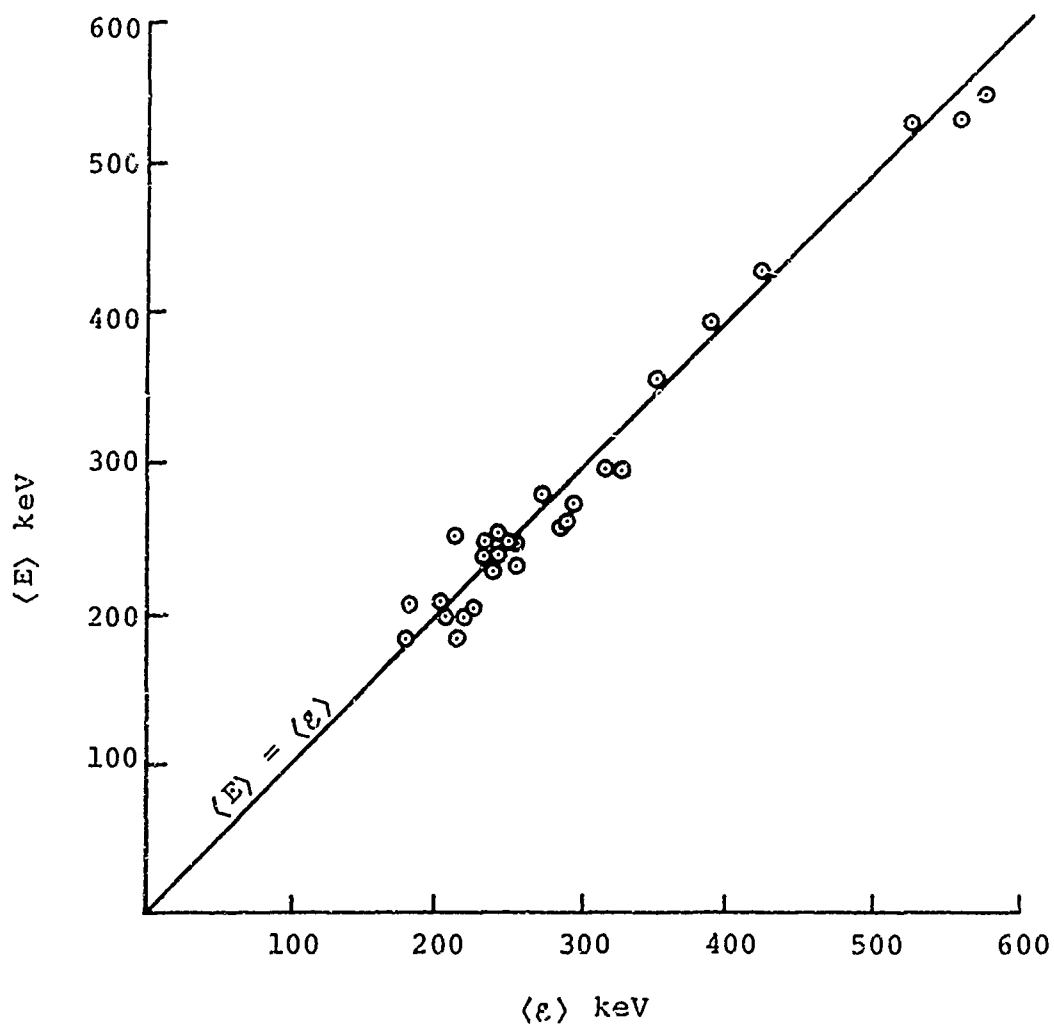
FIGURE 21. EXACT CALCULATION OF THE MEAN ELECTRON ENERGY, <E>, VERSUS THE APPROXIMATION, $\langle \varepsilon \rangle = 0.266\ V_1 + 0.626\ V_2$

65

Accelerating Voltage V(t)		Calculated Deposition Profile		Measured Depth-Dose Histogram

$$\sum_i [V(t_i)I(t_i),t_i]$$

PIE-SPENCE Code

Diode Current I(t)

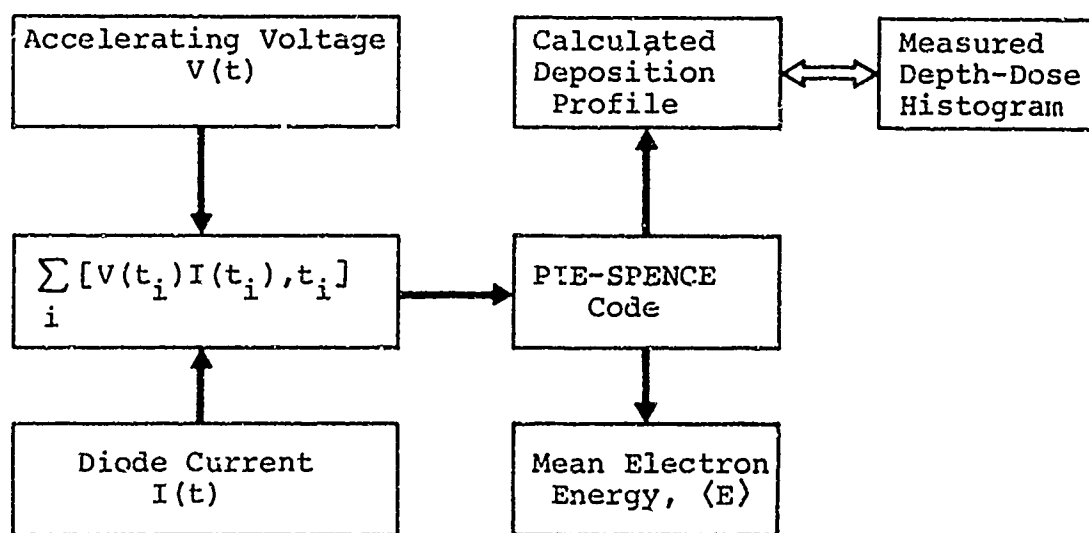Mean Electron Energy, $\langle E \rangle$

FIGURE 22. DIAGNOSTICS LOGIC DIAGRAM

deposited in each foil by the incident fluence. The fluence is defined by the total calories stopped in the entire array divided by the collimator area. The result is a measured deposition profile for aluminum in histogram form.

For the same shot, the time-dependent accelerating voltage, $V(t)$, and the diode monitor, $I(t)$ (Reference 3), are divided into small, equal, time increments, Δt, generating a set $[V(t_i), I(t_i)]$, which becomes the input to an electron deposition code based on an interpolation of Spence's data (Reference 2). The code considers each pair, $[V(t_i), I(t_i)]$, to be a monoenergetic source of energy $eV(t_i)$ and the electron number $\Delta t\, I(t_i)$ from which it calculates the spectrum and the net deposition profile in aluminum. The deposition profile obtained carries the normalization of unit fluence, i.e., $cal/g/cal/cm^2$. The depth-dose histogram is then compared with the deposition profile calculated from the accelerating voltage and diode monitor traces. Figures 23 and 24 show the calculated deposition profiles for mean electron energies of 283 and 216 keV, respectively. Superimposed over these curves are the measured depth dose histograms.

A consistent trend appears in the comparison of the deposition profiles. The first foil always reads a value higher than, and the second foil a value lower than that predicted from the diode diagnostics. This behavior is consistent with non-paraxial electron trajectories and appears to be characteristic of all high-current beams. Clearly, a precise definition of electron trajectories is required to resolve this question, and experiments to this end have been conducted under DASA Contract No. DASA-01-68-C-0096. Specifically, these measurements incorporated a Faraday cup behind filters of various thicknesses, and the transmission data were compared with Monte Carlo electron deposition calculations (Figures 25 and 26).

67
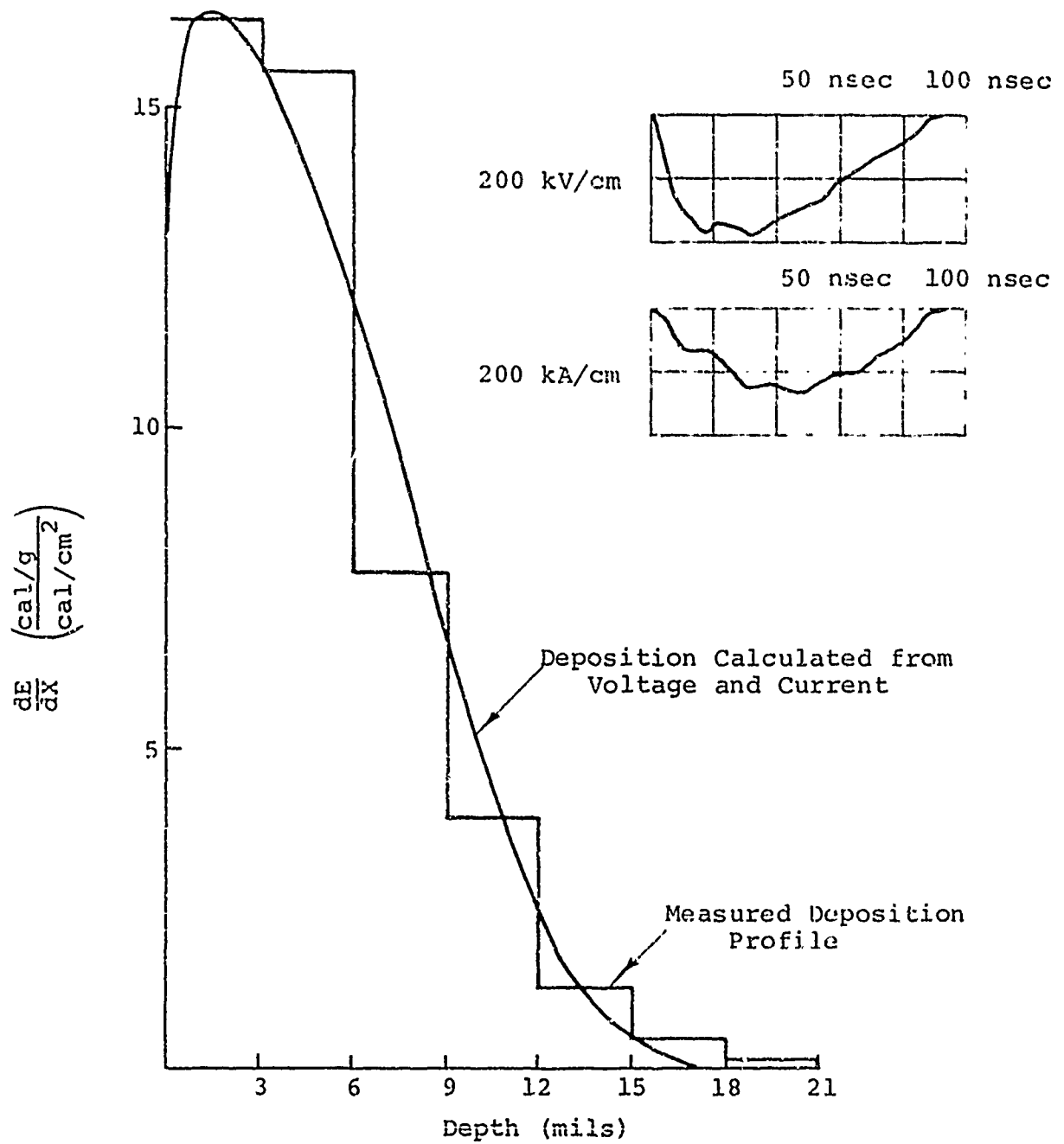
FIGURE 23.   MEASURED AND CALCULATED DEPOSITION
             PROFILES--<E> = 283 keV

68
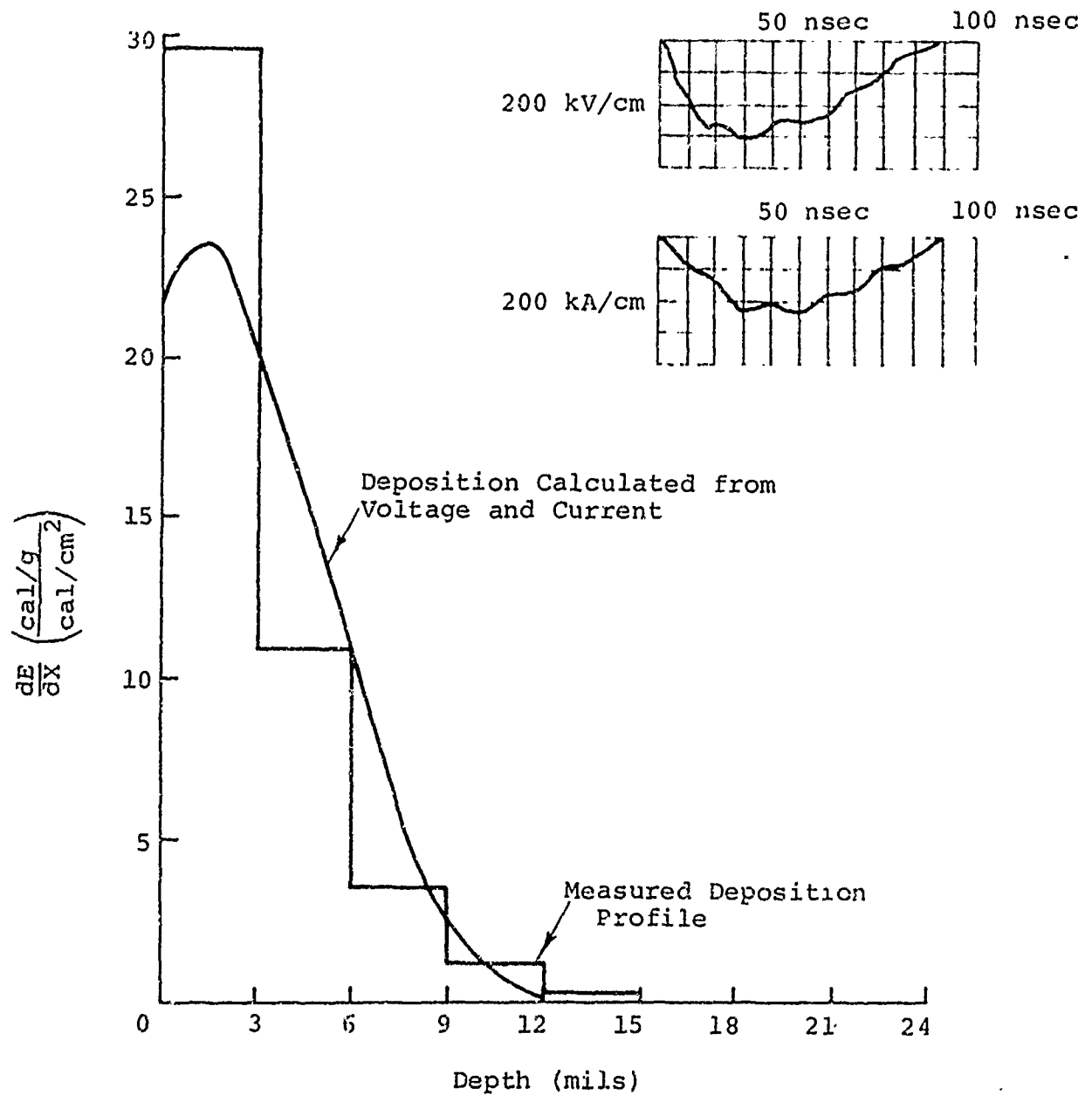
FIGURE 24   MEASURED AND CALCULATED DEPOSITION
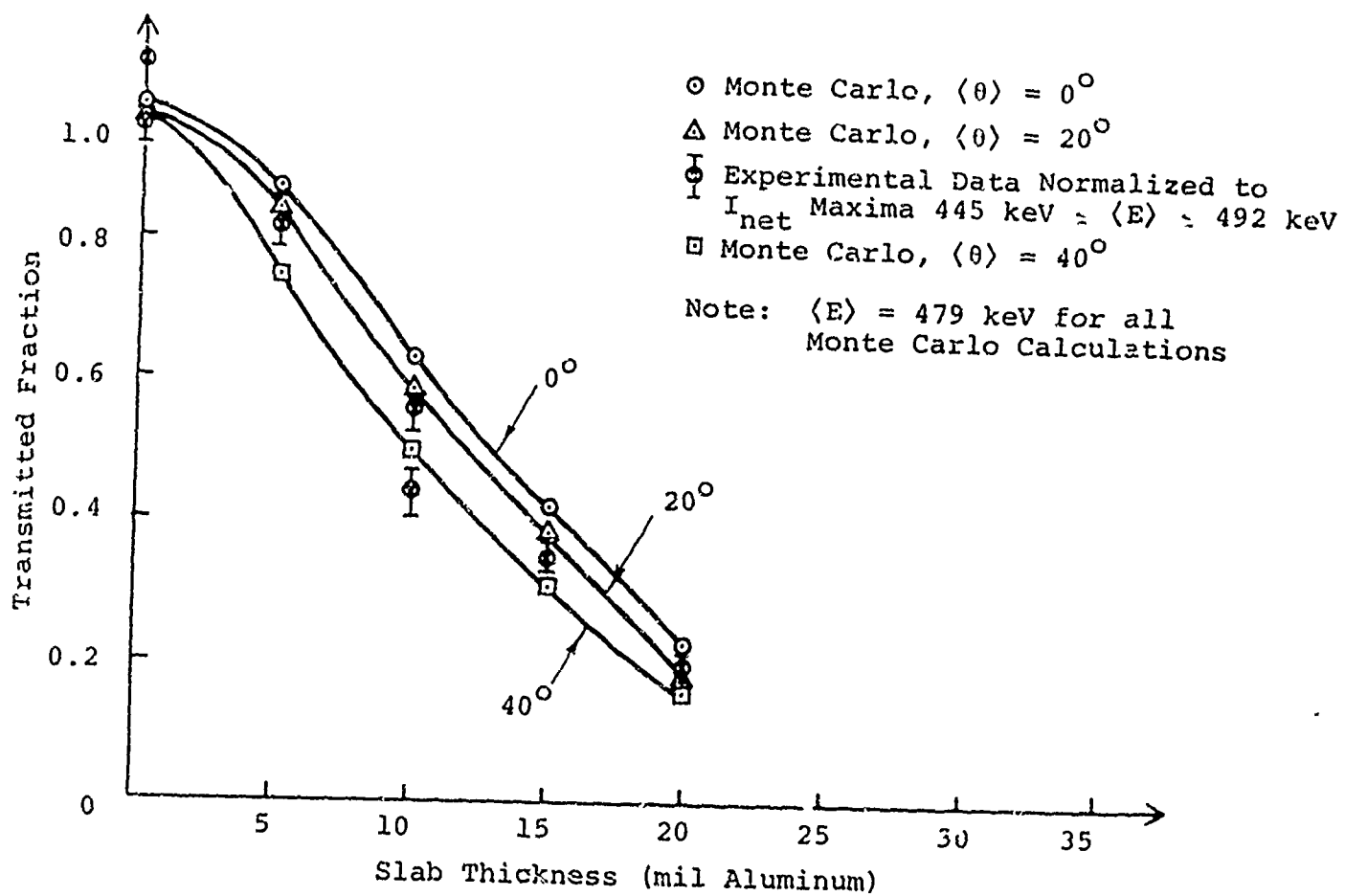PROFILES--<E> = 216 keV

69

FIGURE 25   ELECTRON NUMBER TRANSMISSION THROUGH
             ALUMINUM FILTERS
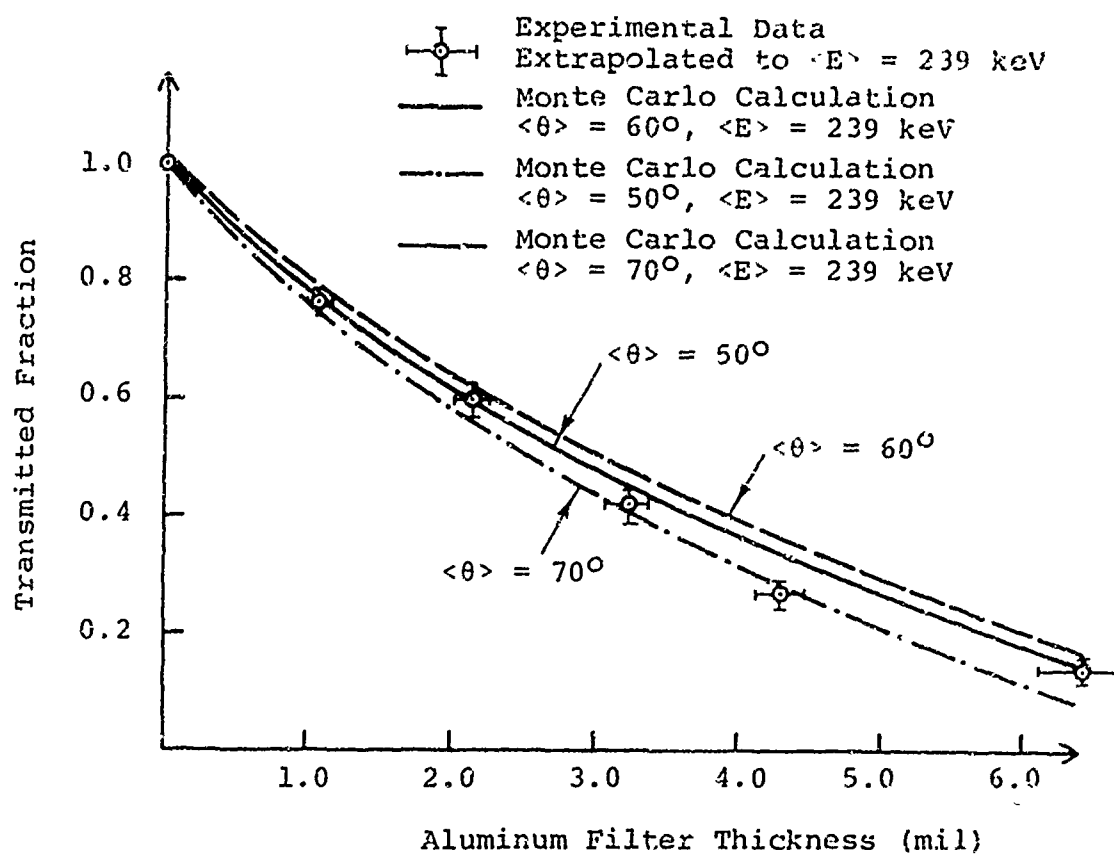
FIGURE 26   ELECTRON NUMBER TRANSMISSION THROUGH
             ALUMINUM FILTERS

71

Results of these investigations indicate a good correlation between the measured mean incidence angles, $\langle\theta\rangle$, and those calculated from the balance between electron transverse and magnetic pressures (Reference 3), which predicts

$$\tan^2\langle\theta\rangle = \frac{\langle\beta_T^2\rangle}{\langle\beta_L\rangle^2} = \frac{2}{\sqrt{\left[\frac{34\times10^3\,\beta\gamma}{I_{net}(1-f_m)}\right]^2 + 1} - 1}$$

$$\gamma = (1-\beta^2)^{-\frac{1}{2}}$$

$$(1-f_m) = \frac{\text{Peak Net Current}}{\text{Peak Primary Current}}$$

$$c\beta_T = \text{Transverse Velocity}$$

$$c\beta_L = \text{Longitudinal Velocity}$$

$$c\beta = c\sqrt{\beta_L^2 + \beta_T^2} = \text{Total Velocity}$$

$$I_{net}(kA) = \text{Net current in amps (Rogowski coil output)}$$

Data from a recent program funded by Sandia, Livermore (Reference 9), illustrate the correlation between measured and calculated $\langle\theta\rangle$ at the sample location:

$$\langle E\rangle = 480\ keV$$

$$(1-f_m) = 0.6$$

$$I_{net} = 15\ kA$$

72

$$I_{pr} = 25 \text{ kA}$$

$$\frac{\langle \beta_T{}^2 \rangle}{\langle \beta_L \rangle^2} = 0.38$$

$$\langle \theta \rangle = 31^{\circ}$$

The calculated angle is in good agreement with the data shown in Figure 25.

2. <u>Summary of Beam Diagnostics</u>

The techniques of determining the electron fluence level and normalized deposition profile as discussed in the preceding section are summarized in Figure 27. A brief review follows:

The scaled dI/dt probe signal representing the inductive pickup of the voltage monitor is subtracted from the voltage monitor signal, yielding the accelerating voltage across the anode-cathode space. This, in addition to diode current and the mean angle of incidence, is used as the input to Monte Carlo electron-deposition calculations yielding the mean electron energy and a deposition profile normalized to unit fluence. Using the signals from the voltage monitor and the Rogowski coil (net beam current near the sample), the fluence during an actual sample irradiation shot is determined and used to scale the normalized deposition profile to yield the actual deposition profile for that shot.

Data collected in a recent program (Reference 9) has afforded an excellent opportunity to test the validity of the 738 Pulserad diagnostics in defining the electron-beam environment. Figure 28 shows the comparison between calculated and measured stress his-
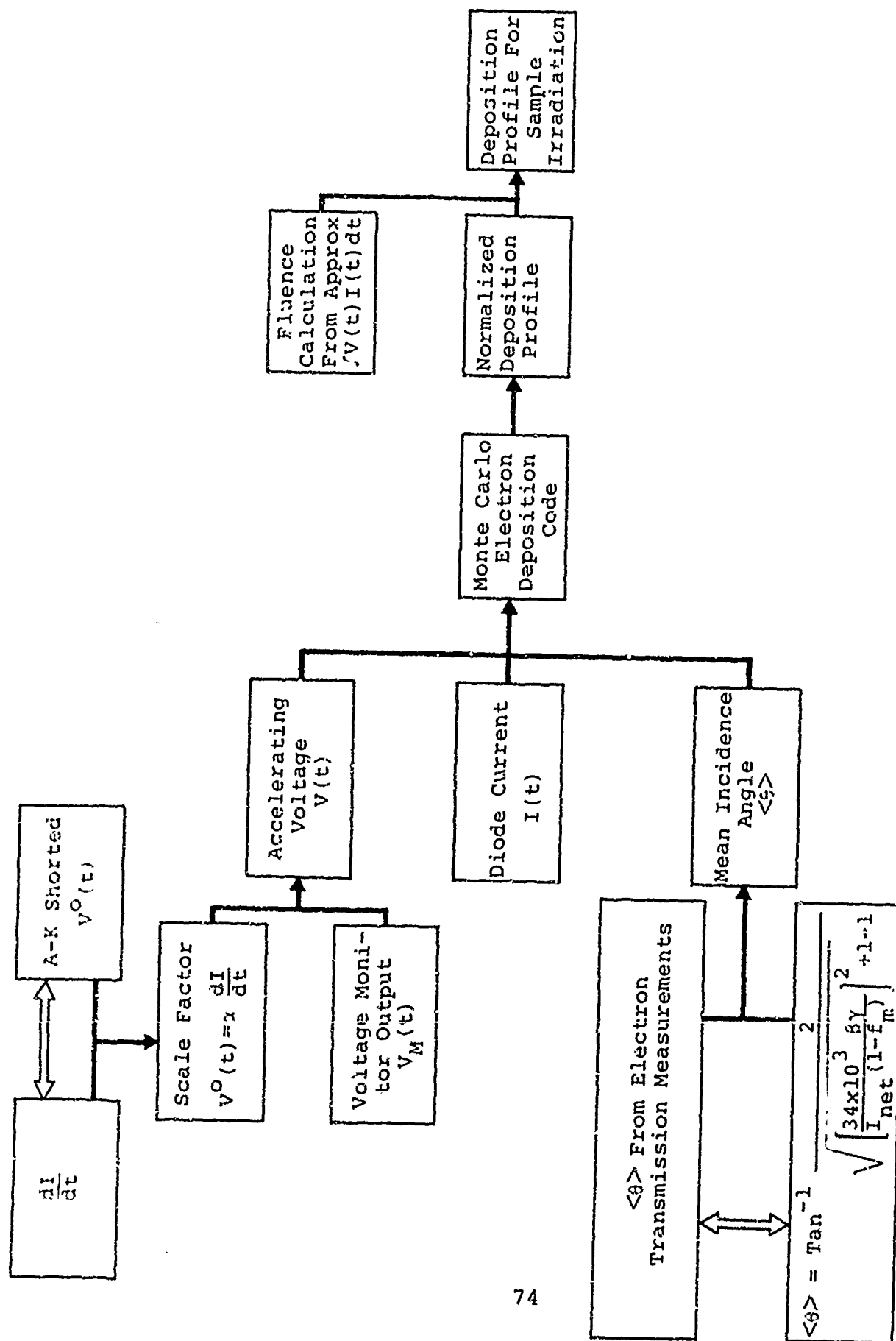
FIGURE 27   APPLICATION OF ELECTRON BEAM DIAGNOSTICS TO MATERIAL RESPONSE STUDIES
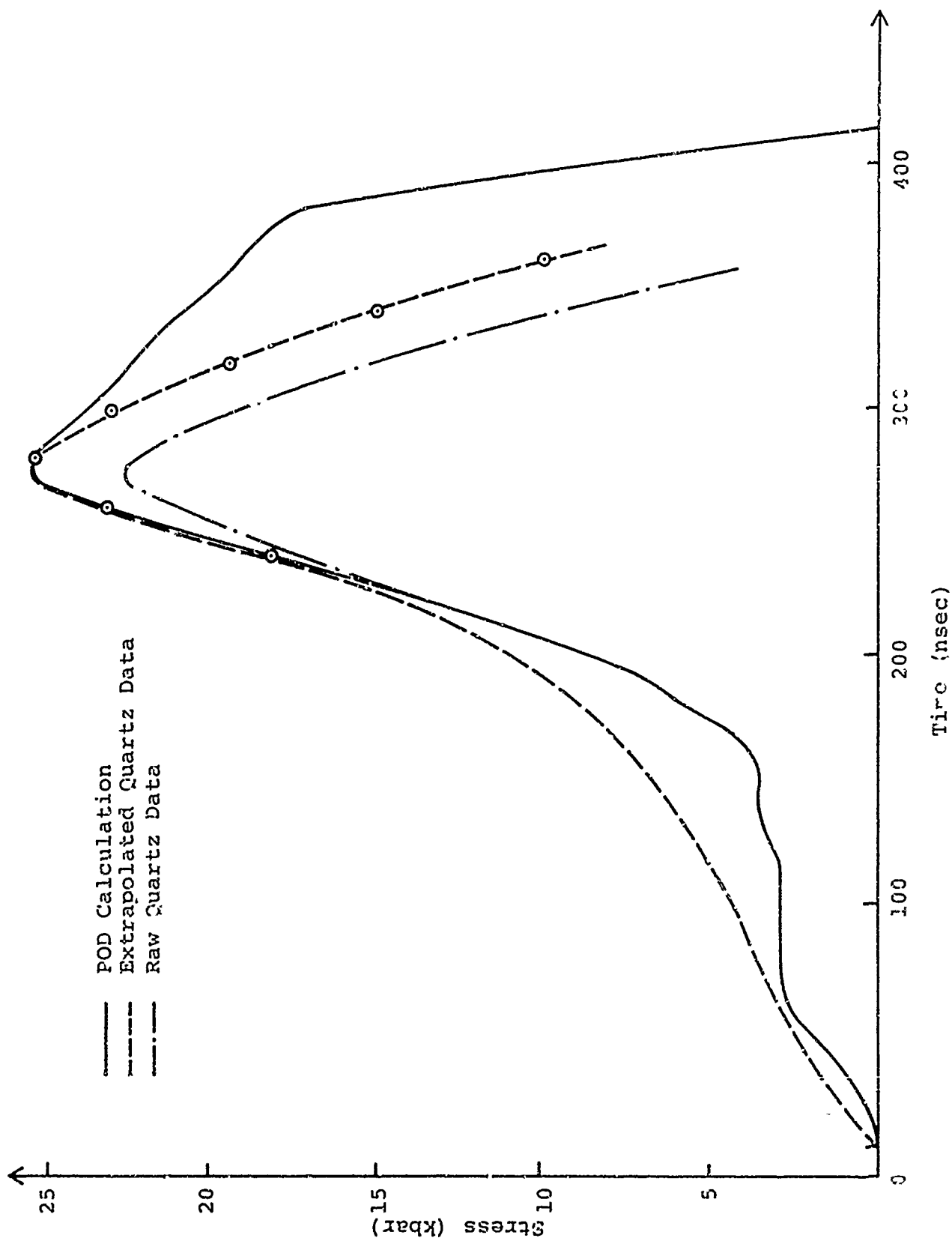
74

FIGURE 28. MEASURED AND CALCULATED STRESS HISTORY

7114

75

tories and Figure 29 gives a plot of peak stress (measured and calculated) versus fluence in beryllium. The agreement between the measurements and calculations indicates a good confidence level in the diagnostics.

D.   IMPULSE MEASUREMENT TECHNIQUES AND DATA SUMMARY

The ballistic pendulum used in this program is shown in Figure 30. The pendulum axle supporting the rod and bob rotates on two instrumentation bearings and is mechanically coupled to a variable transformer to record the pendulum deflection. Rotation of the pendulum axle changes the magnetic coupling between an externally powered primary and a secondary coil whose output signal is then displayed on an oscilloscope. Figure 31 shows a typical output signal recording the pendulum deflection as a function of time. The variable transformer response was calibrated by photographing its output at successive pendulum deflections in five-degree increments (Figure 32).

Figure 33 shows the calibration curve obtained by plotting pendulum deflection, θ, versus the output signal from the variable transformer. The output is linear for $0^{O} \leq \theta \leq 20^{O}$, with increasing non-linearity for $\theta > 20^{O}$. Although the calibration curve permits meaningful operation in the $\theta > 20^{O}$ region of maximum deflection, the normal operating procedure is to increase the bob mass of the pendulum in advance of anticipated deflections of $\theta > 20^{O}$. Low-impulse sensitivity is obtained by decreasing the bob mass while increasing the oscilloscope sensitivity.

The differential equation governing the motion of a damped simple pendulum is of the form

$$\ddot{\theta} + 2\beta\dot{\theta} + \frac{g}{\ell} \sin \theta = 0$$
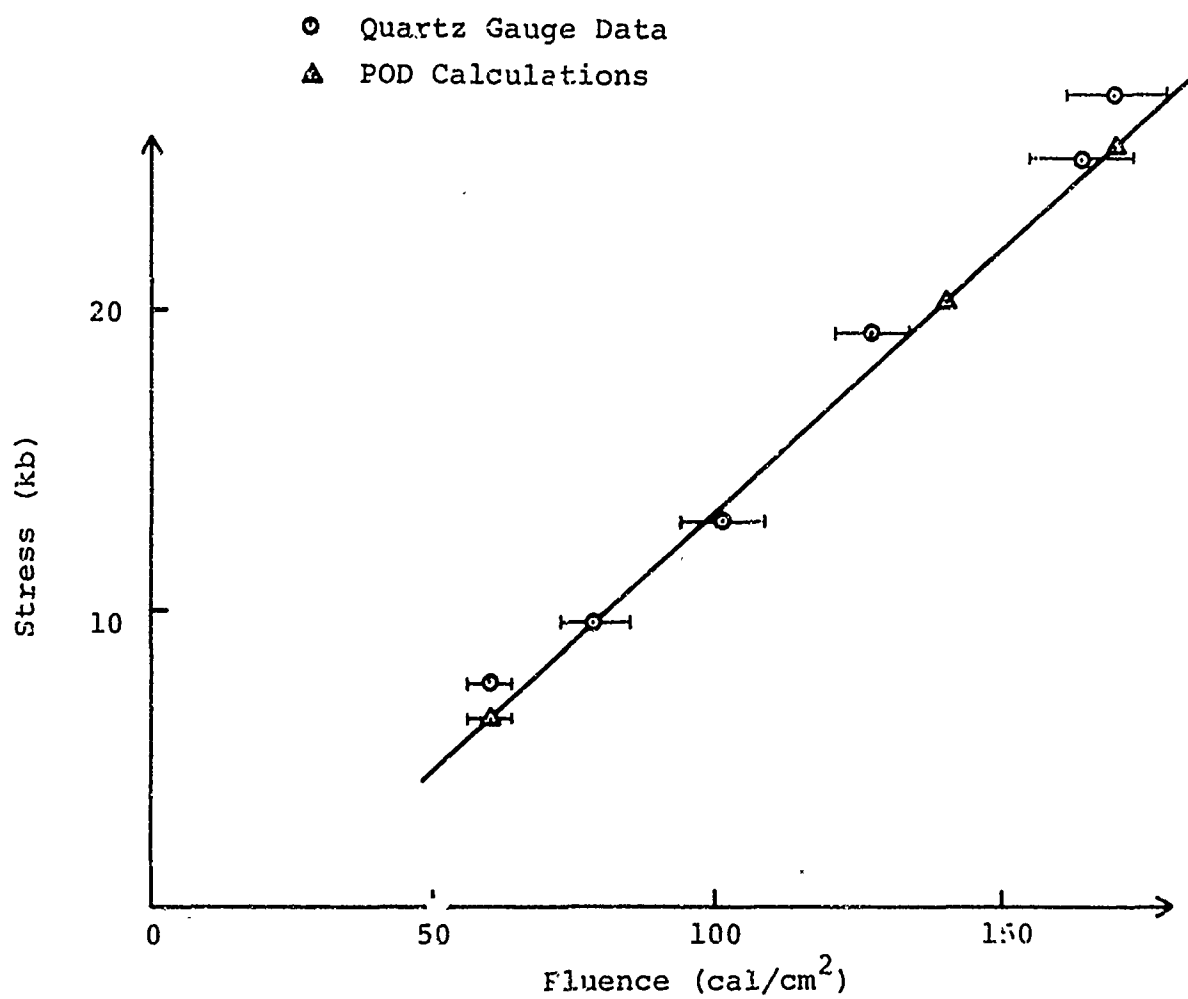
FIGURE 29. PEAK STRESS VERSUS FLUENCE QUARTZ DATA FOR BERYLLIUM

7074

77
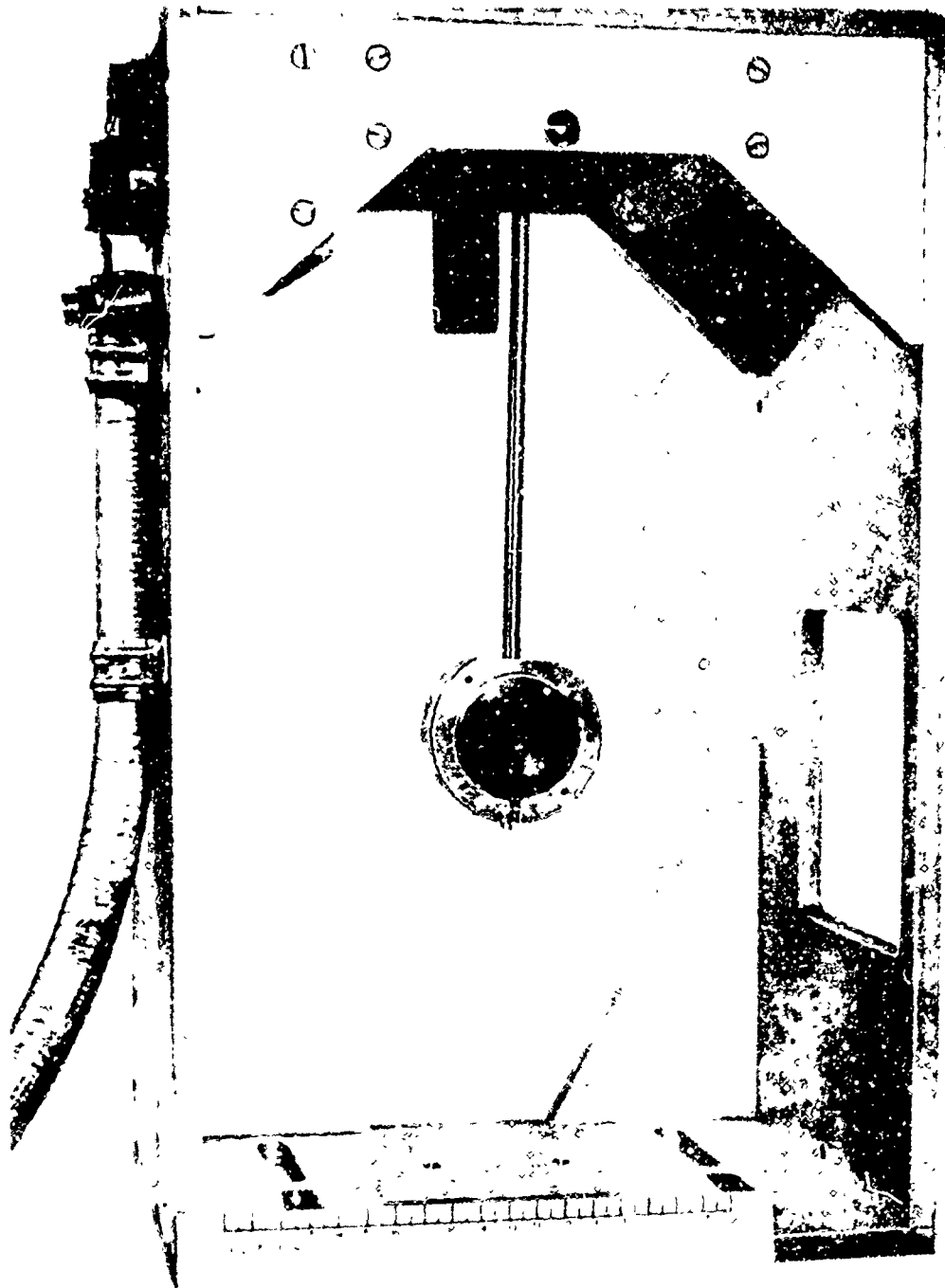
FIGURE 30. BALLISTIC PENDULUM

78

Upper:
100 msec/cm

Lower:
10 msec/cm

Base Lines (θ=0)

Upper:
6.67 deg/cm
100 msec/cm

Lower:
1.67 deg/cm
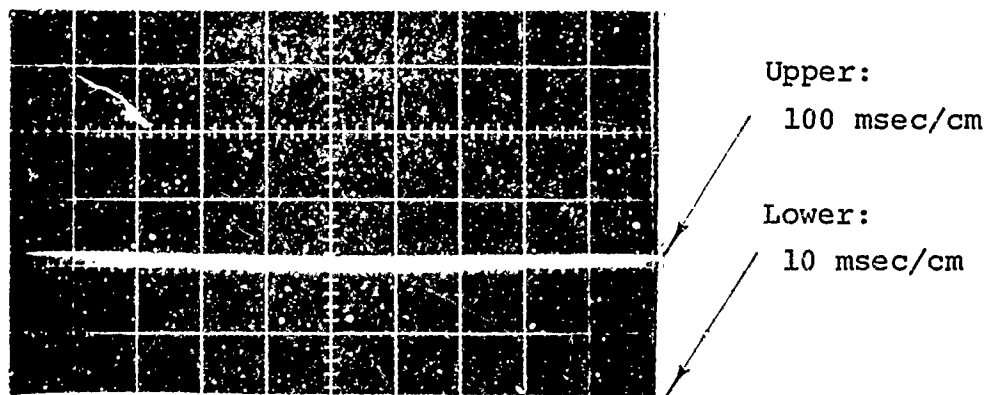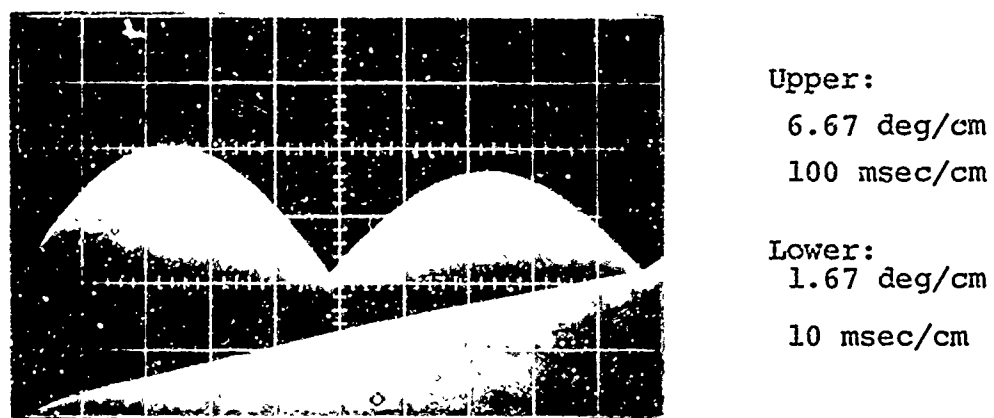
10 msec/cm

Pendulum Deflection.   Second Peak Is A Rebound From A Bob Stop
To Prevent Sample Impact On Guide Cone

FIGURE 31.   RECORDED PENDULUM DEFLECTION

R8700

79

a.

1 V/cm
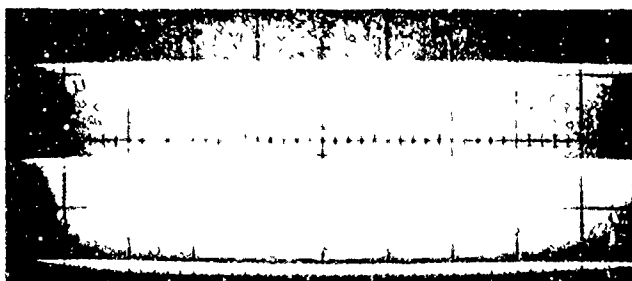
100 msec/cm

b.

2 V/cm
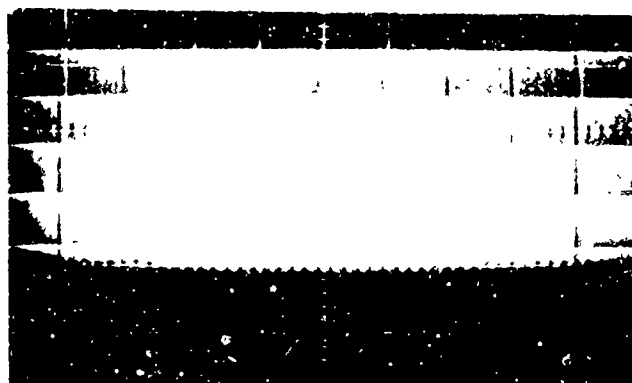
100 msec/cm

FIGURE   32. VARIABLE TRANSFORMER CALIBRATION AT $\Delta\theta = 5$ deg

R8501

80
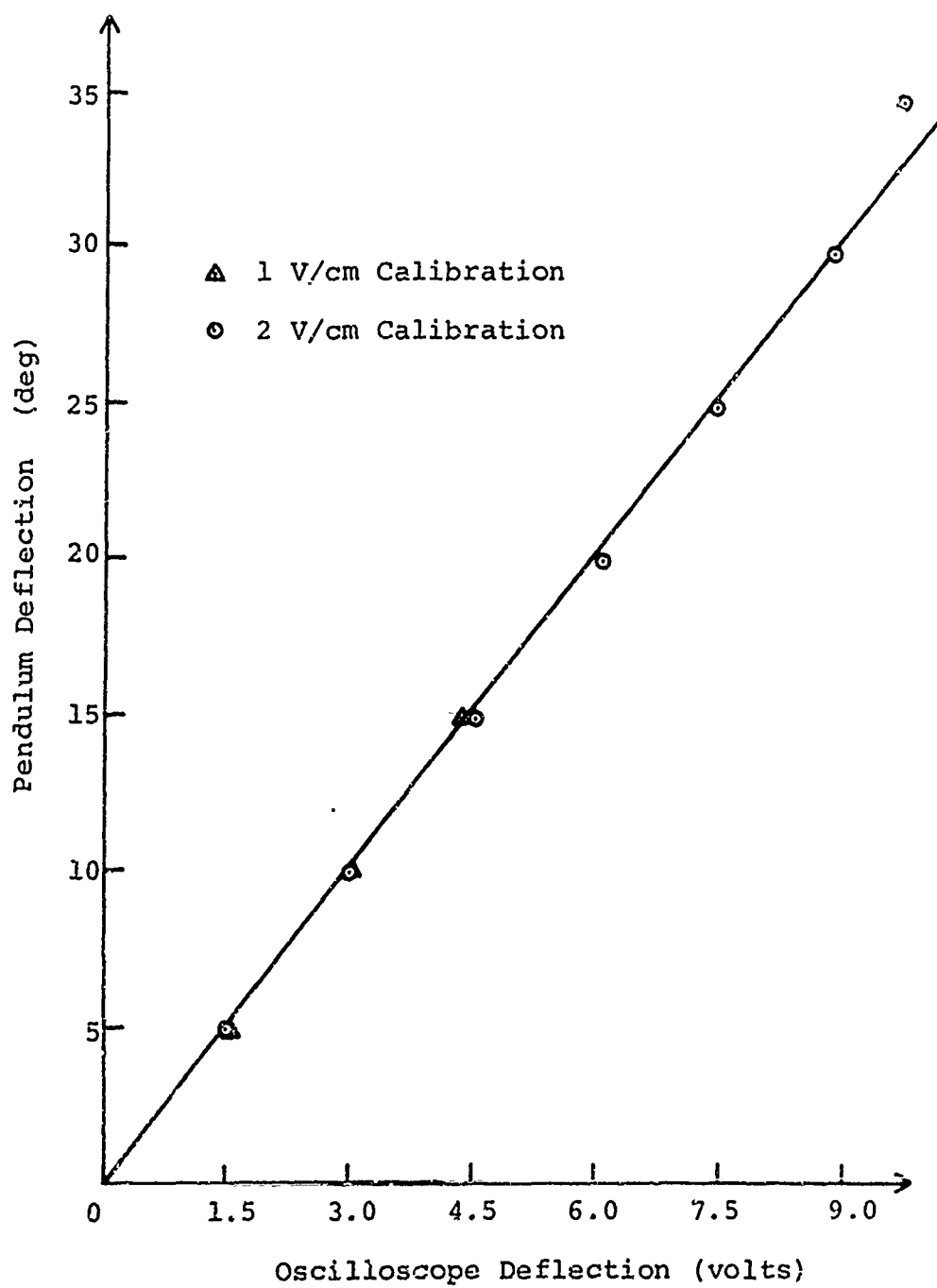
FIGURE 33. VARIABLE TRANSFORMER CALIBRATION CURVE

81

where the damping is proportional to the angular velocity, $\dot{\theta}$. For angles up to 20 degrees $(\sin \theta)/\theta \approx 0.98$. Thus, to a good approximation

$$\ddot{\theta} + 2\beta\dot{\theta} + \frac{g}{\ell}\,\theta = 0$$

It can be shown that $\theta(t) = Ae^{-\beta t} \sin \omega t$ with $\omega = \sqrt{g/\ell - \beta^2}$ satisfies the equation of motion.

A determination of the damping coefficient, β, is made by recording a number of free oscillations of the pendulum resulting from electron-beam-generated impulse. Comparing peak deflections, a number of oscillations, n, apart yields

$$\frac{\theta(t_1)}{\theta(t_2)} = \frac{Ae^{-\beta t_1} \sin \omega t_1}{Ae^{-\beta t_2} \sin \omega t_2} = e^{-\beta(t_1 - t_2)} = e^{2\pi n\beta/\omega}$$

Thus, the damping coefficient

$$\beta = \frac{\omega}{2\pi n}\,\ln \frac{\theta(t_1)}{\theta(t_2)} = \frac{1}{nT}\,\ln \frac{\theta(t_1)}{\theta(t_2)}$$

where the period T and the ratio $\theta(t_1)/\theta(t_2)$ are taken directly from the output of the variable transformer. Damping coefficient determinations are performed prior to every experimental run. A typical value is $\beta = 0.03$ sec^{-1}. The period, T, of the pendulum is 0.95 sec for most bob masses used. The first peak deflection from the beam-generated impulse occurs at $t = 1/4T = 0.24$ sec. The damping factor, under these conditions, has the value $e^{-\beta t} = 0.99 \approx 1.0$.

Consequently, bearing drag associated with pendulum motion, although small, can be accounted for in the impulse calculation.

Applying the initial condition $\ell d\theta/dt = v$ at $t = 0$ to the solution of the damped pendulum equation of motion yields

$$\theta(t) = \frac{v}{g} \ (\omega + \beta^2/\omega) \ e^{-\beta t} \ \sin \omega t$$

But since typically

$$\beta^2/\omega = \frac{(0.03)^2 \ (0.95)}{2\pi} \ = \ 0.0014 \ << \ \omega,$$

$$\theta(t) = \frac{\omega v}{g} \ e^{-\beta t} \ \sin \omega t \ = \ \frac{2\pi v}{gT} \ e^{-\beta t} \ \sin \omega t$$

The maximum deflection, θ_{max}, occurs at $t = 1/4 \ T$ where $\sin \omega t = 1$. Solving the θ_{max} equation for v and multiplying by the total moving mass of the pendulum, the momentum imparted to the pendulum is

$$(MV) = \frac{Mg \ T \ \theta_{max} \ e^{\beta(T/4)}}{2\pi} \ = \ 2.72 \ MT \ \theta_{max}(deg) \ exp \ (\frac{\beta T}{4})$$

The peak deflection, θ_{max}, and the period of the pendulum, T, are obtained directly from the oscilloscope trace of the output from the variable transformer that monitors the pendulum motion (Figure 31).

Consideration of the initial slope of the pendulum deflection (Figure 31, lower trace) affords another calculation of the impulse impacted to the pendulum. If ℓ is the pendulum center of mass, then

$$\Delta(MV) = M\ell \ \frac{\Delta\theta}{\Delta t} = \frac{Mg}{\omega^2 + \beta^2} \ \frac{\Delta\theta}{\Delta t} \ \longrightarrow \ \frac{Mg}{\omega^2} \ \frac{\Delta\theta}{\Delta t}$$

or

$$\Lambda(MV) = Mg \left(\frac{T}{2\pi}\right)^2 \frac{\Delta\theta}{\Delta t}$$

Since the damping coefficient measurements cannot reflect effects from static frictional forces at the start of the pendulum swing, a calibration of the pendulum with a known impulse was necessary. A CO_2-cartridge-fed air pistol provided the calibrating impulse. The pellet velocity was obtained from the transit time between two photocells separated by a known distance; the pellet mass was measured with an analytical balance. The pellet was brought to rest in the pendulum bob by a layer of absorbing material. The setup is shown in Figure 34 and the calibration data are shown in Figure 35.

Because of the motion of the 738 Pulserad during an electron beam pulse, it became necessary to mount the ballistic pendulum and beam guide cone on a stable platform. The experimental setup is shown in Figure 36.

Existing pendulum bobs accommodate disk-shaped samples of 1.30 in diam and thicknesses from 0.080 to 0.25 in. This, however, is not a limitation, since bobs are easily fabricated to suit the task. The samples are clamped between two retaining rings and this essentially constitutes the front face of the pendulum bob (Figure 37).

The accuracy of impulse measurements depends on two quantities: the momentum imparted to the bob, $\Lambda(MV)$ and the crater area of the sample, $\bar{A}$. The error in $\Lambda(MV)$ is best demonstrated in the calibration (Figure 35) in which the deviation
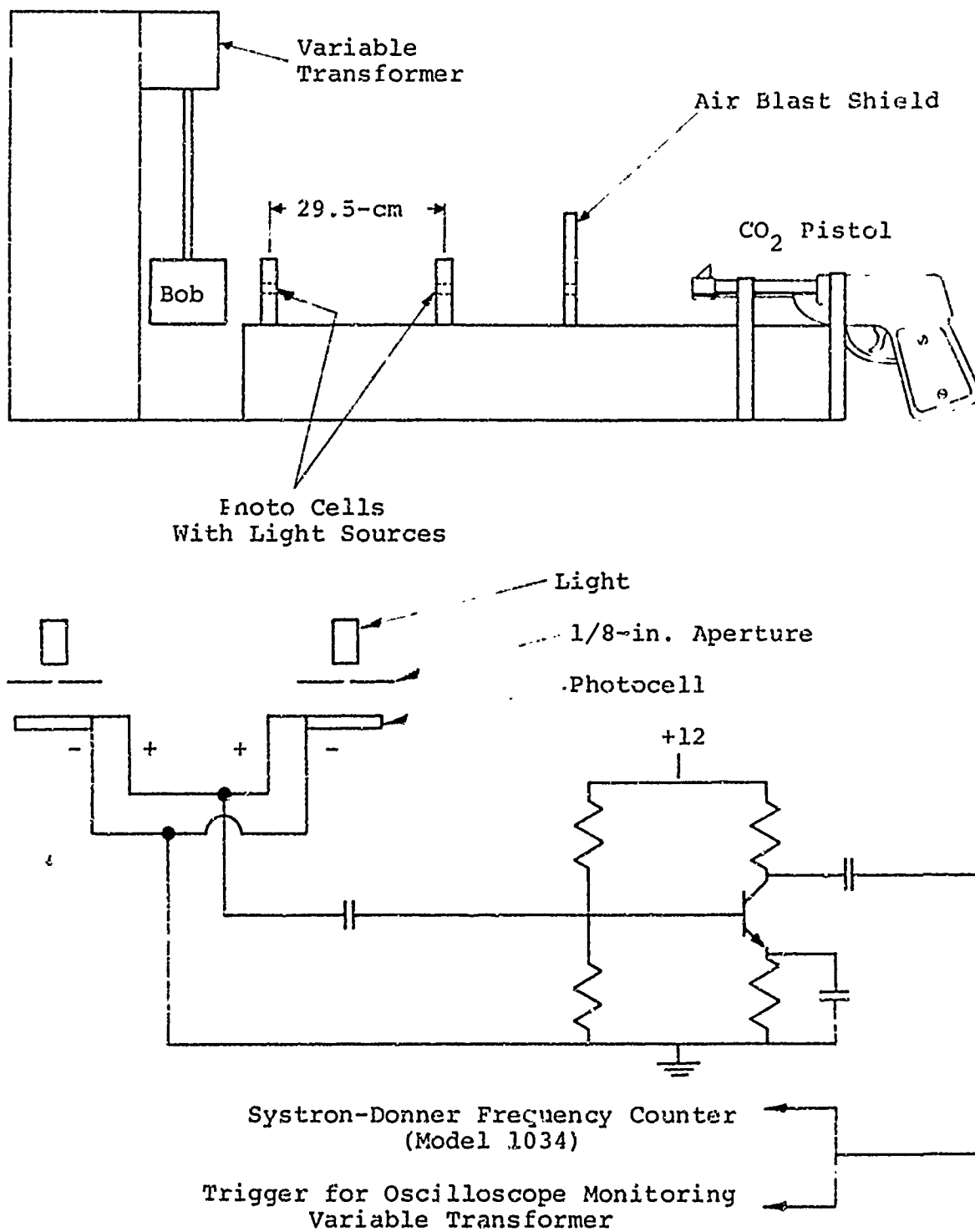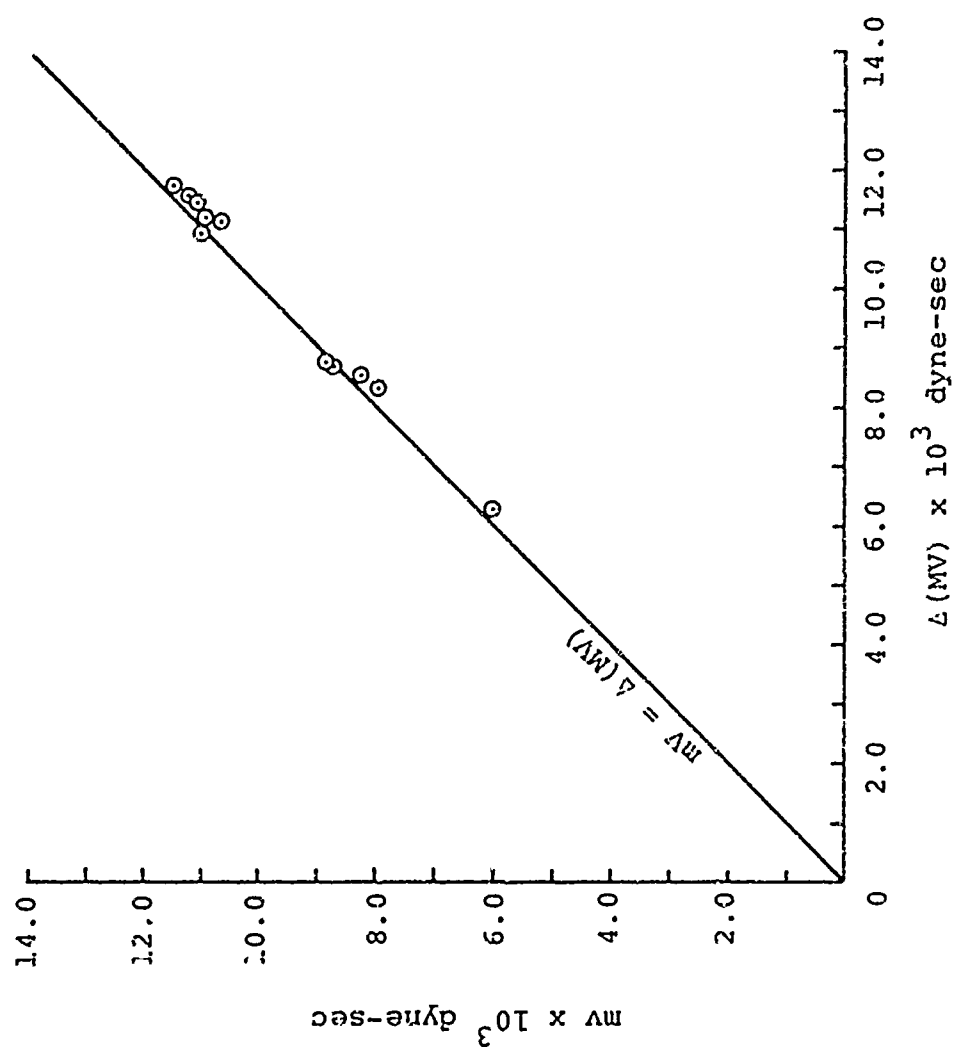
84

FIGURE 34   PENDULUM CALIBRATION SETUP

FIGURE 35   GUN PELLET MOMENTUM, mv VERSUS MOMENTUM
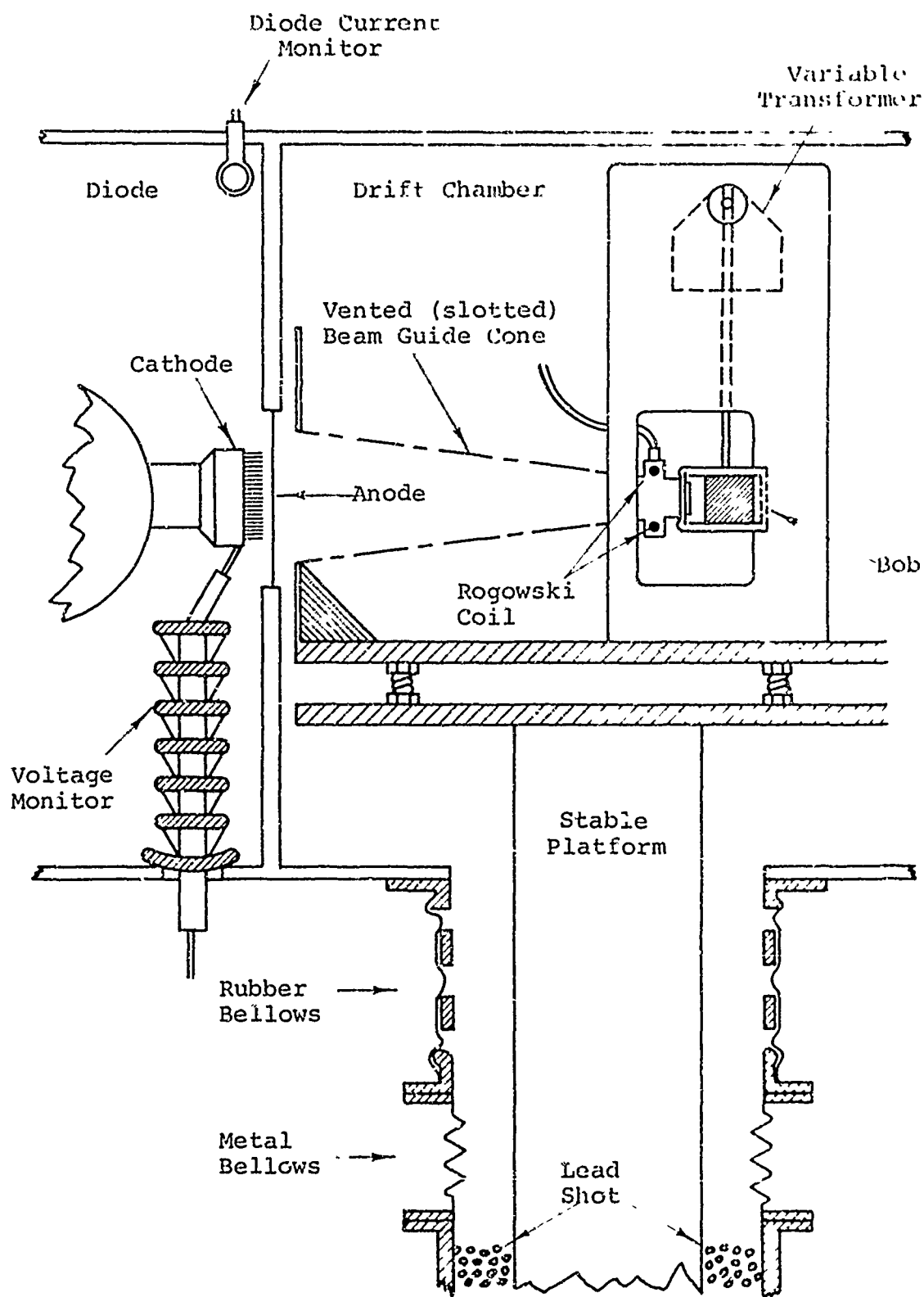   RECORDED BY PENDULUM ∠ (MV)

86

FIGURE 36. IMPULSE MEASUREMENT SETUP

87
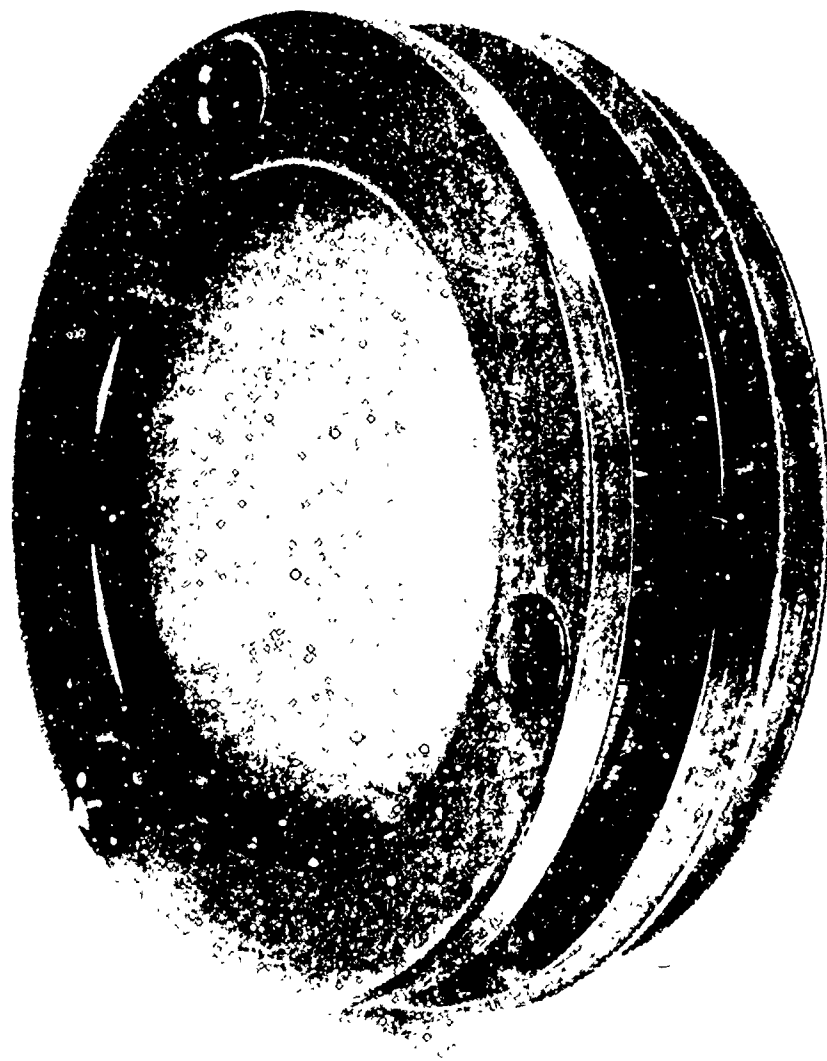
Figure 37.   PENDULUM BOB FACE ASSEMBLY WITH SAMPLE

from the calibrating momentum is less that ± 3%. This error bar
includes inaccuracies in the measurement of the total moving mass
and the error incurred in measuring the maximum amplitude and
period of oscillation from the oscilloscope photograph of the
variable transformer output. The error in the measurement of
beam crater area can be minimized by photographing samples "head-
on" and measuring $\bar{A}$ from the pictures using a polar planimeter.

The deflection readout of the pendulum is unaffected by
electron-beam-generated noise since the bob remains stationary
during deposition time and begins to move long after all noise
has subsided. Variations in the deposition profile shape affect
the pendulum only through the magnitude of the total impulse they
generate. The pendulum deflection can be controlled by varying
the mass of the bob. Oscillations on the order of a tenth of a
degree are easily measured by increasing oscilloscope sensitivity
to the variable transformer signal. There is virtually no upper
limit to measurable impulse since bob mass can be increased to
the kilogram range.

A pendulum with a manganin gauge built into the bob is
currently under development. Damping characteristics like those
of the standard pendulum have been achieved. The remaining
difficulty is shielding the gauge from the RF environment in the
electron beam drift chamber without coupling the machine motion
to the pendulum. This problem is presently being addressed and
once solved will allow the measurement of total impulse and rear
surface stress simultaneously.

89

The techniques described above have been used to generate impulse data in aluminum. These data are summarized in Table II. Since the data cover a range of mean energies, a number of typical energy deposition profiles, normalized to unit fluence, are shown in Figures 38 to 43.

The maximum front surface dose in these experiments was 1800 cal/g. This is shown in the following section to be within the range of the spall-dominated impulse. In Section IV, a model is presented for this regime, which is in good agreement with the data. In addition, measurements and calculated values of transmitted stress and ejected velocities are presented.

TABLE II

ALUMINUM IMPULSE DATA

$\langle E \rangle$ (keV)	Φ (cal/cm^2)	$\overline{A}$ (cm^2)	Δ (MV) (KILO-DYNE-SEC)	I (ktap)	Δm (g)
$(208)^1$	29^2	2.7^3	4.08	1.51	0.082
(222)	(30)	3.2	5.93	1.85	0.109
220	31	3.0	5.45	1.83	0.119
(225)	35	3.2	5.55	1.72	0.131
(232)	(37)	3.3	7.66	2.32	0.151
(233)	41	3.35	7.19	2.15	0.117
(260)	41	3.0	6.54	2.18	0.140
219	42	3.5	7.19	2.07	0.138
249	43	3.2	6.02	1.88	0.114
257	43	2.8	7.30	2.61	0.154
(223)	45	3.3	6.76	2.05	0.137
353	52	(~4.0)	13.17	~3.3	0.242
266	60	3.3	9.05	2.74	0.155
371	60	3.9	17.08	4.40	0.279
(386)	61	(~3.8)	13.63	~3.6	0.241
620	113	3.7	31.25	8.44	0.537

Notes to Tabular Data

Column 1. Parentheses indicate mean energy estimated by approximate integration scheme, others by numerical integration of voltage and current traces.

Column 2. Parentheses indicate fluence estimated by approximate integration of current trace.

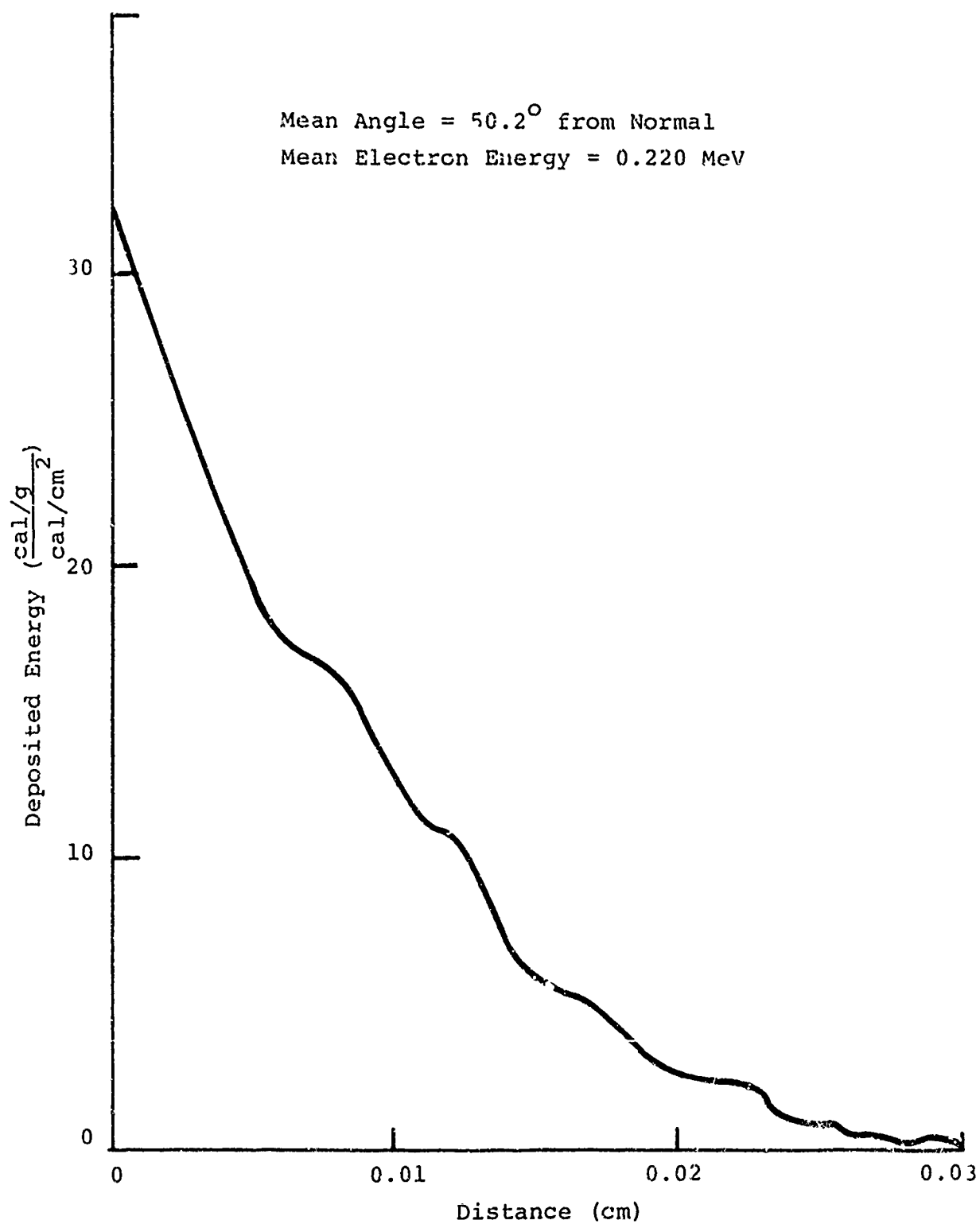Column 3. Parentheses indicate uncertain measurements of area due to irregular crater edge.

FIGURE 38.   NORMALIZED DEPOSITION PROFILE

FIGURE 39. NORMALIZED DEPOSITION PROFILE
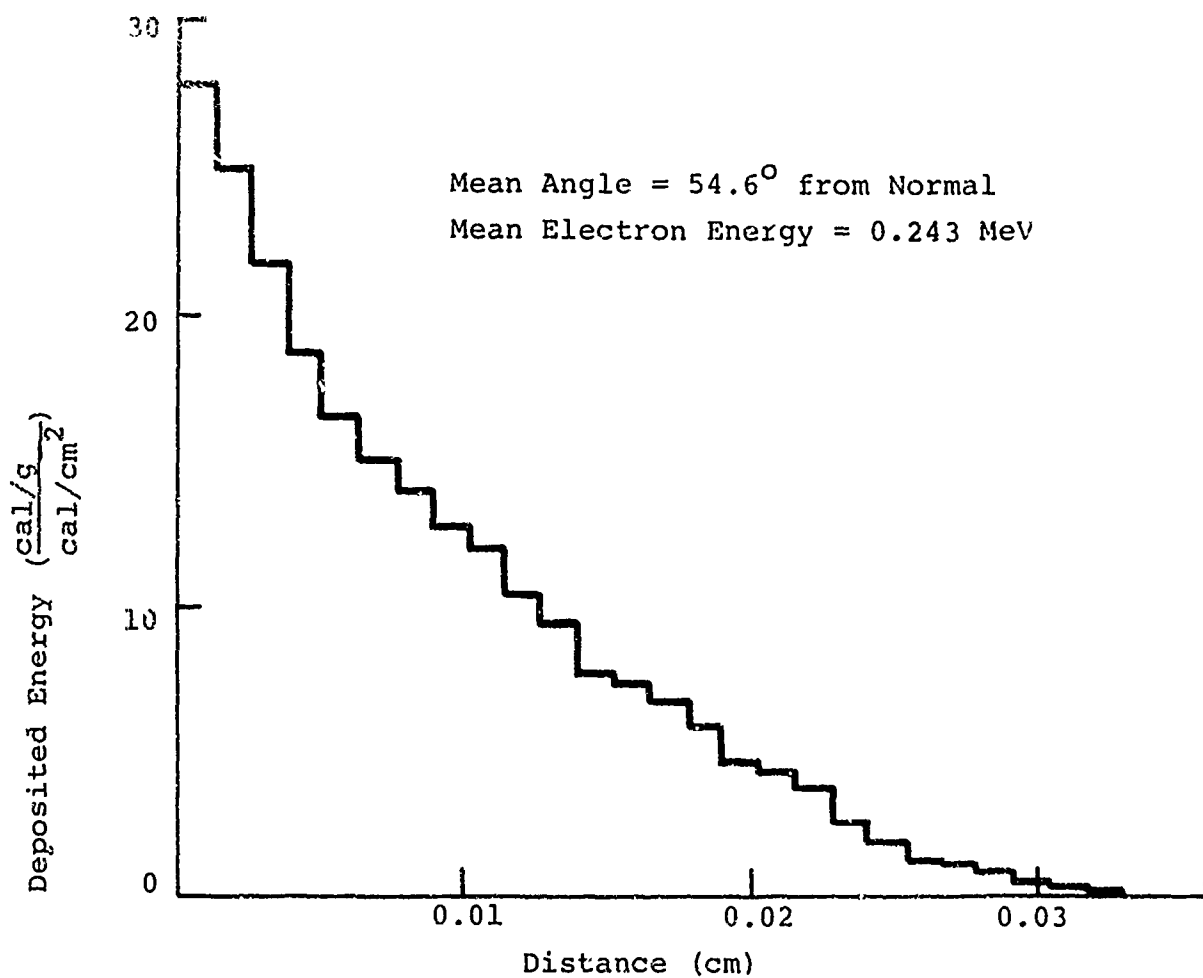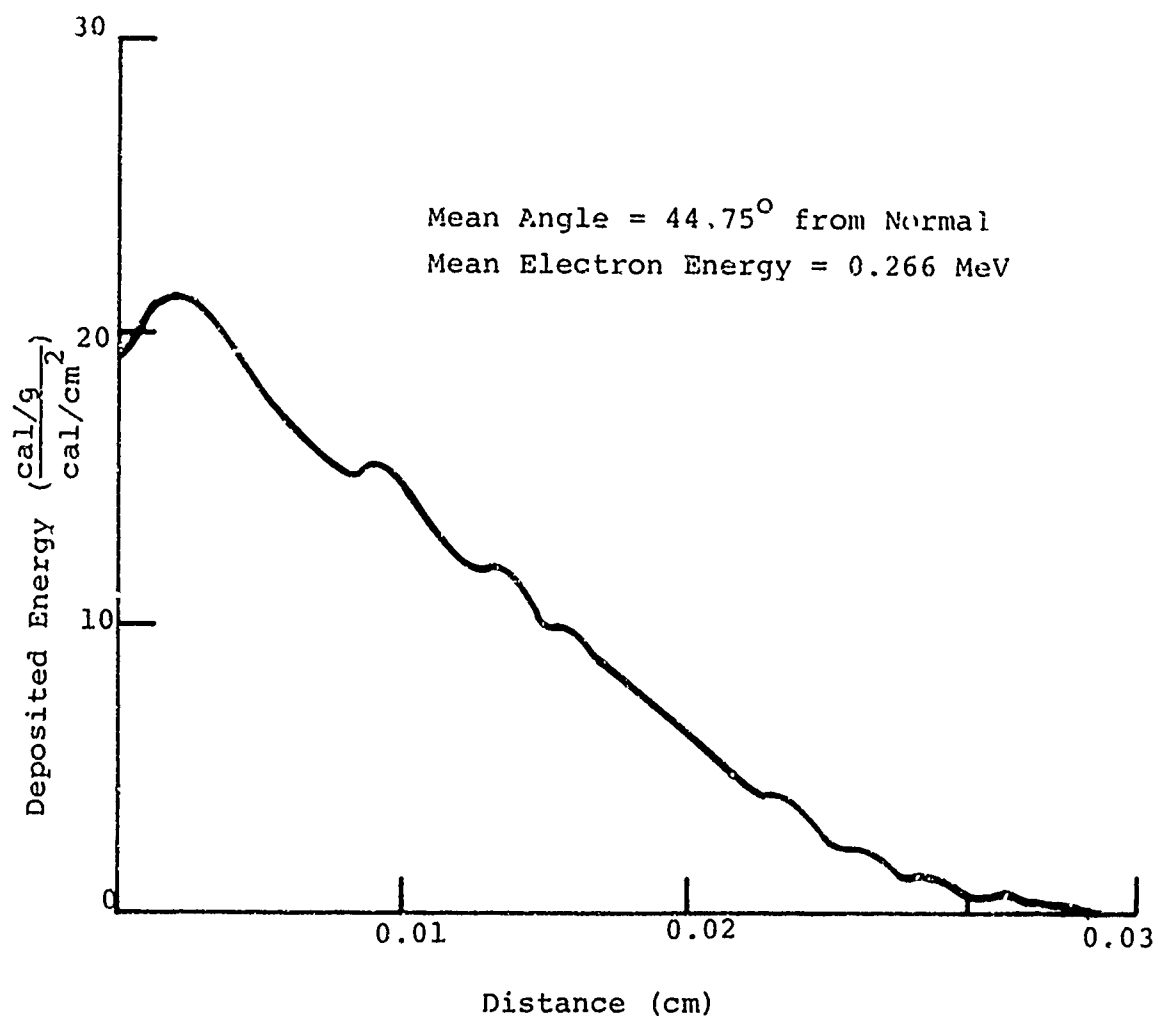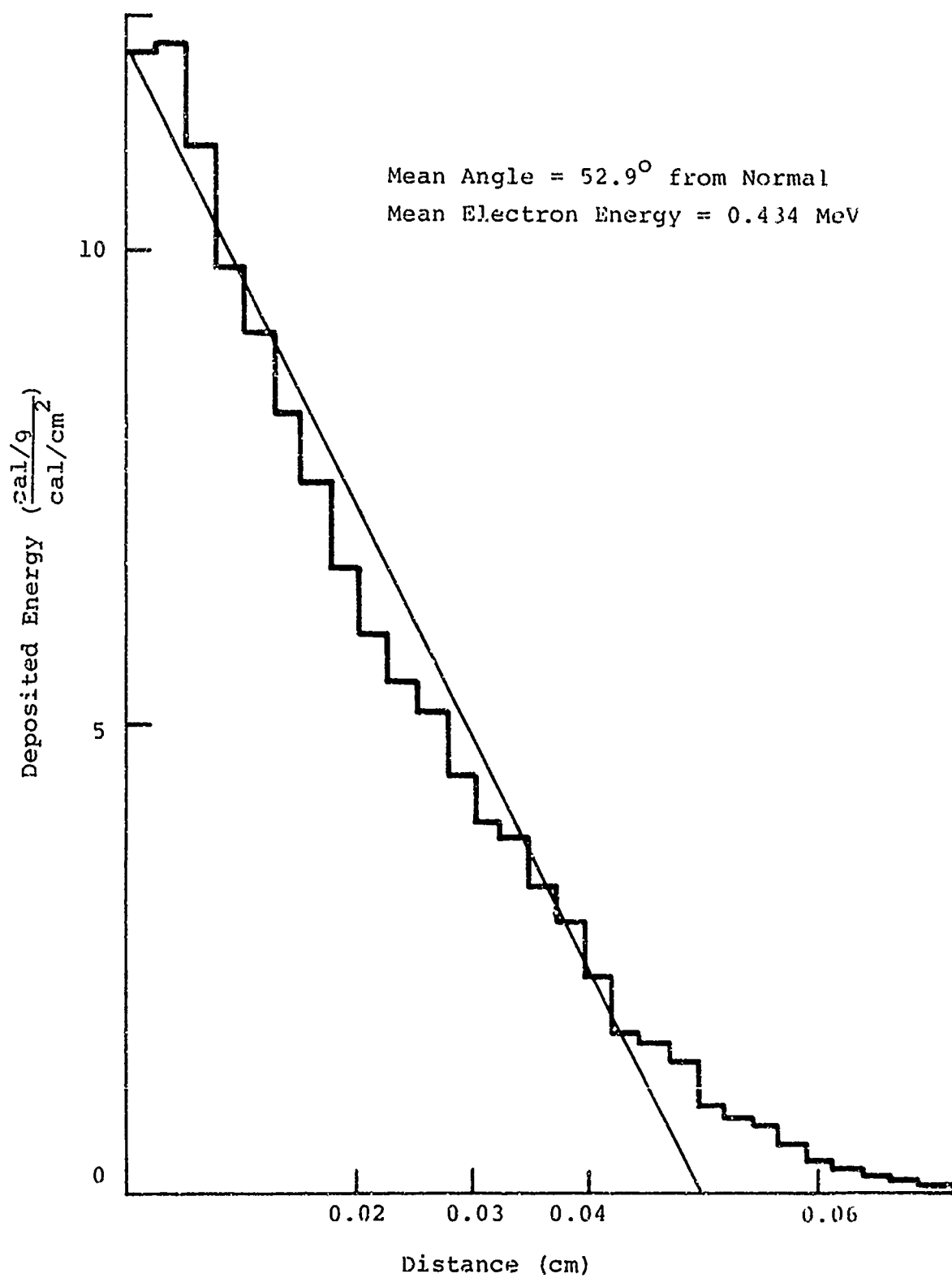
8758

FIGURE 40.   NORMALIZED DEPOSITION PROFILE

FIGURE 41.   NORMALIZED DEPOSITION PROFILE
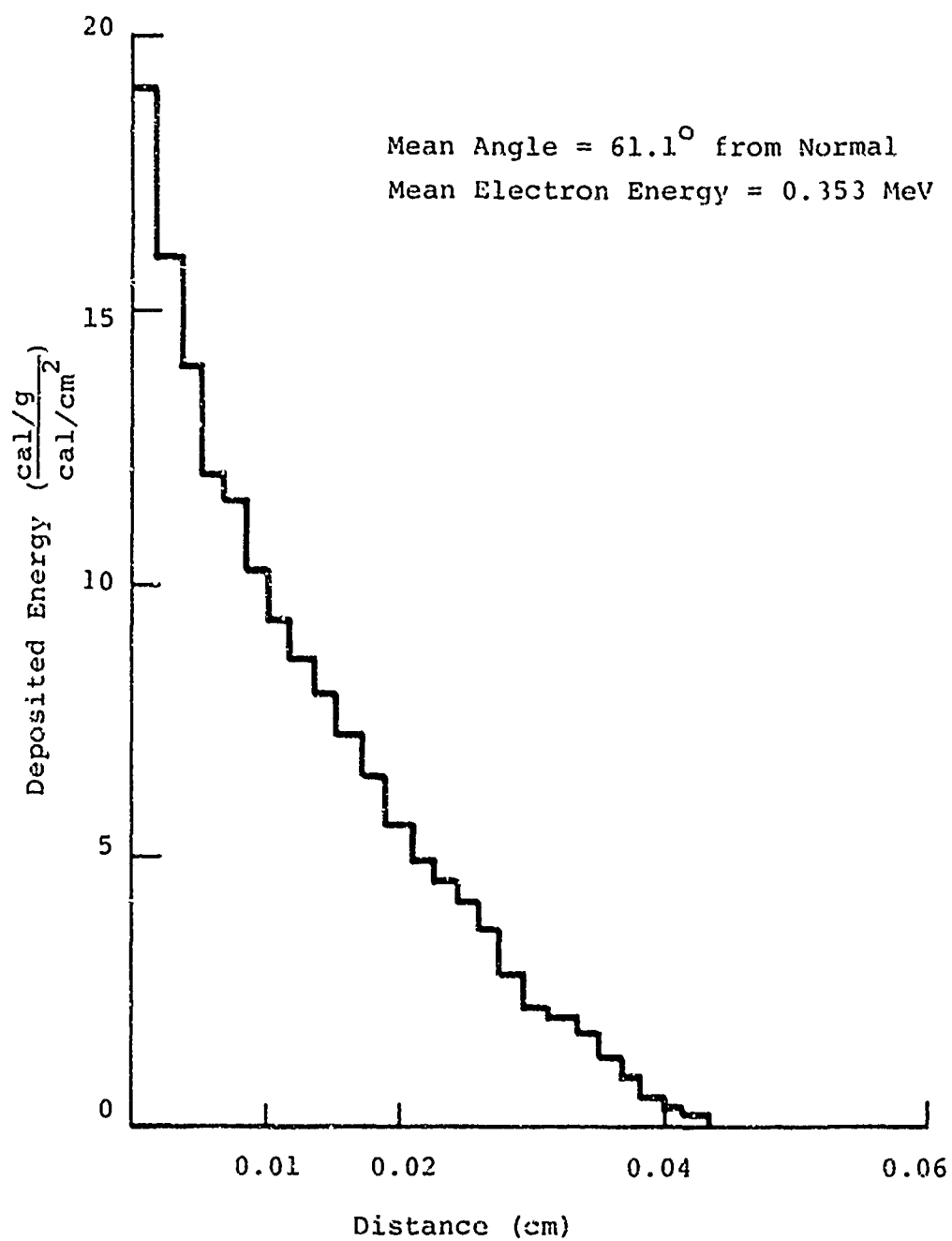
FIGURE 42.   NORMALIZED DEPOSITION PROFILE

8801
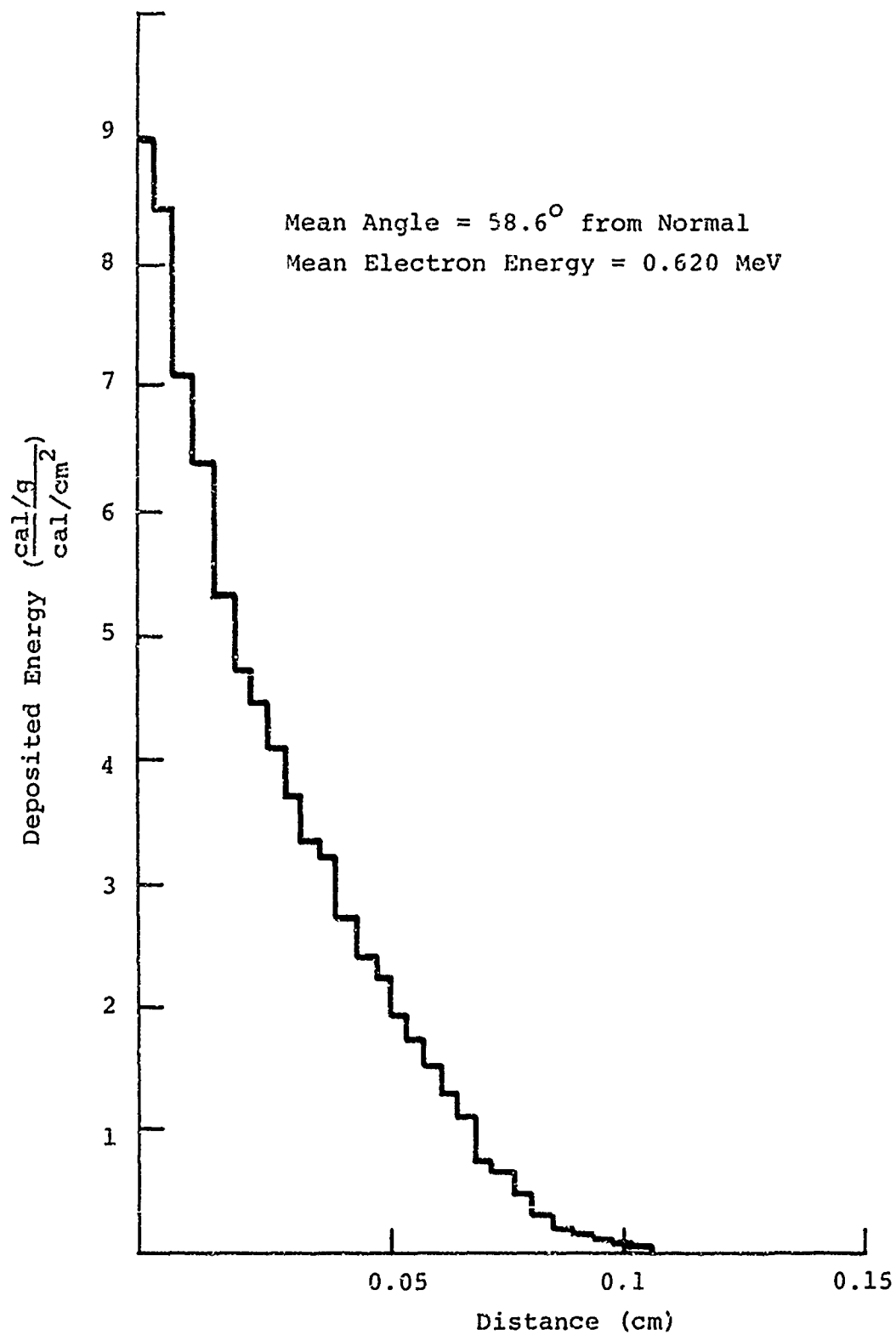
FIGURE 43. NORMALIZED DEPOSITION PROFILE

Mean Angle = 58.6° from Normal
Mean Electron Energy = 0.620 MeV

8790

97

EXPERIMENTS AND ANALYSIS ON
MELT-DOMINATED IMPULSE

A. INTRODUCTION

The two previous sections describe analytical and experimental techniques used for studying impulse generation and the impulse data that were collected for aluminum in the melt-dominated or liquid splash-off regime.

In this section, a model for melt-dominated impulse is developed that gives good agreement with the data collected here as well as other data. When certain simplifying assumptions are added to the model, the equations are linearized to second order in deposited energy, and the deposition profile is represented as a straight line, the model predicts impulse as being proportional to fluence, multiplied by an exponential factor that contains the deposition time. That is,

$$ I = 0.04186 \frac{\Gamma}{2C_k} \phi \exp \left(- \frac{1}{2} \frac{C_k \, t_D}{r} \right) $$

where I is the impulse in ktap, Γ is the Gruneisen ratio, C_k is the bulk sound speed in cm/μsec $(K/\rho_o)^{\frac{1}{2}}$, where K is the bulk modulus, ϕ is the fluence in cal/cm^2, r is the electron range in cm, and t_D is the deposition time in μsec. This simplified model gives quite good agreement with magnesium, aluminum, and silver, and fair agreement with lead, using no adjustable parameters and handbook values for material properties.

In addition, an analysis is made of other experimental techniques for measuring impulse. The techniques include the use of quartz gauges for measuring stress histories, and flyer plates used as momentum traps on the back of the irradiated sample.

Preceding page blank

B.   A MODEL FOR MELT-DOMINATED IMPULSE

The first logical step in building a model for melt-dominated impulse would be to define the region. A quantitative estimate of the upper bound, must come from parameters of the model itself. For now, however, the assumption will be made that vapor effects are negligible, and an estimate of where vapor effects are important will be made later on.

It would be desirable to use one of the analytical expressions, (Reference 17), such as the Whitener (1) or BBAY (2) expressions

$$I = \sqrt{2} \int_{0}^{x} \left[E_i(m) - E_f(m) \right]^{\frac{1}{2}} dm \tag{1}$$

$$I = 1.2 \left\{ 2 \int_{0}^{x} m \left[E_i(m) - E_f(m) \right] dm \right\}^{\frac{1}{2}} \tag{2}$$

for calculating impulse. To do so requires an expression for $E_f(m)$, the final internal energy. To use the sublimation energy, E_s, is clearly incorrect since this would imply that no impulse is generated for deposited energy less than E_s, and there is experimental evidence that impulse is generated.

Certainly the McCloskey-Thompson model (Reference 17) could be used to calculate the final state energy. When this is done for aluminum, however, the model does not fit the data. Figure 44 shows the impulse data in aluminum, and the impulse predicted by the McCloskey-Thompson model, in the BBAY expression, where

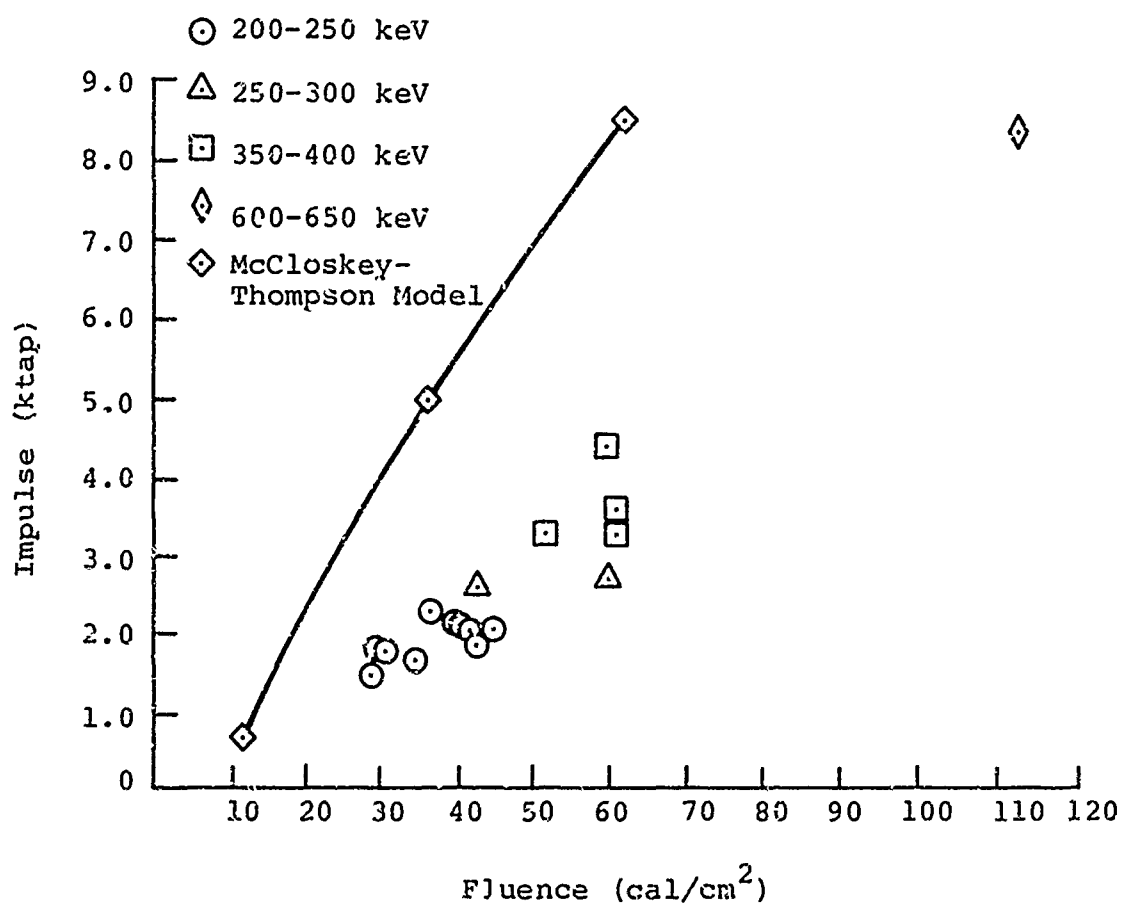$$E_f = E_m \left(1 + \ln \frac{E_d}{E_m} \right),$$

100

FIGURE 44. ALUMINUM IMPULSE DATA AND McCLOSKEY-THOMPSON-
BBAY EXPRESSION

101

for aluminum $E_m = 160$ cal/g and $E_d =$ the deposited energy. To understand why this model is not appropriate, it will be useful to picture the process going on in melt-dominated impulse generation.

Consider energy incident from the left, deposited in a material instantaneously and for simplicity, with a linear deposition profile. If the material had strength and were a linear fluid, the initial stress would separate into halves, a right-moving stress wave and one moving to the left. The left-moving wave reflects from the front surface as a following, anti-symmetric tension. The stress history at a point, then, shows the initial compression (followed by an increase in compression if the point is more than half the range from the front surface) and a sudden drop into tension. If, on the other hand, the heated material has no tensile strength, an increment of liquid will separate from the body of "solid" at each time increment.

In effect, the vapor phase is ignored (the equilibrium vapor pressure of the spalled liquid is assumed zero), and the solid-liquid transition is also ignored--the material is treated as though it is simply a strengthless solid. With this model, the generated impulse can be calculated by finding the internal energy changed to kinetic energy in adiabatic expansion, and this energy substituted in the Whitener expression for impulse. (The Whitener rather than the BBAY expression should be used as each increment of mass is suddenly relieved to zero pressure; it is not pushing on other mass.) To this end, the kinetic energy for a simplified equation of state is derived below.

Assume an equation of state to be of the form

$$P = f(v) + \frac{\Gamma E}{v} ,$$

102

where for definiteness the units of pressure, P, and internal energy, E, are 10^{12} erg/ref cm^3 (Mbar), v is the relative volume (V/V_{ref}), and Γ is the Gruneisen ratio (assumed constant). To find the path of adiabats, the condition $(dE/dv) = -P$ is substituted, to give the differential equation

$$\frac{dP}{dv} + \frac{\Gamma + 1}{v} P = \frac{1}{v} \frac{d}{dv} \left(v f(v) \right)$$

which has the solution

$$P = f(v) - \Gamma \left(\frac{1}{v}\right)^{\Gamma + 1} \int^{v} \xi^{\Gamma} f(\xi) d\xi + C \left(\frac{1}{v}\right)^{\Gamma + 1}$$

Specializing f to be the first term of a standard polynomial equation of state for a solid

$$f(v) = K \left(\frac{1}{v} - 1\right)$$

where K is the bulk modulus,

$$P = C\left(\frac{1}{v}\right)^{\Gamma + 1} - \frac{K}{\Gamma + 1}$$

and C is determined by the initial condition

$$P_o = f(v_o) + \frac{\Gamma E_o}{v_o}$$

defining

$$\varepsilon = \frac{(\Gamma + 1) \, P_o}{K}$$

$$P = \frac{K}{\Gamma + 1} \left[(1 + \varepsilon) \left(\frac{v_o}{v}\right)^{\Gamma + 1} - 1 \right]$$

103

Thus the relative volume at which the adiabat is at zero pressure, v^* is

$$v^* = v_0 (1 + \varepsilon)^{1/(\Gamma + 1)}$$

The energy released in expanding to zero pressure, which is the kinetic energy of motion, is given by

$$\Delta E = \int_{v_0}^{v^*} P_{adia}^{(\xi)} \, d\xi$$

Substituting

$$\Delta E = \frac{K}{\Gamma + 1} \int_{v_0}^{v_0(1 + \varepsilon)^{1/(\Gamma + 1)}} \left[(1 + \varepsilon) \left(\frac{v_0}{v} \right)^{\Gamma + 1} - 1 \right] dv$$

$$\Delta E = \frac{K v_0}{\Gamma(\Gamma + 1)} \left\{ (\Gamma + 1) + \varepsilon - (\Gamma + 1)(1 + \varepsilon)^{1/(\Gamma + 1)} \right\}$$

This is the result sought, but more usefully in what follows, we expand for small ε (using a Taylor's series), and obtain

$$\Delta E = \frac{K v_0}{2(\Gamma + 1)^2} \varepsilon^2 = \frac{v_0 P_0^2}{2K}$$

This expression is compared to the McCloskey-Thompson expression for the final energy in Figure 45 for the parameters of aluminum assuming the energy is deposited at reference volume. It is clear that the final energy is larger for the linear fluid; hence, the impulse calculated will be less since less energy is available for the kinetic energy of motion.
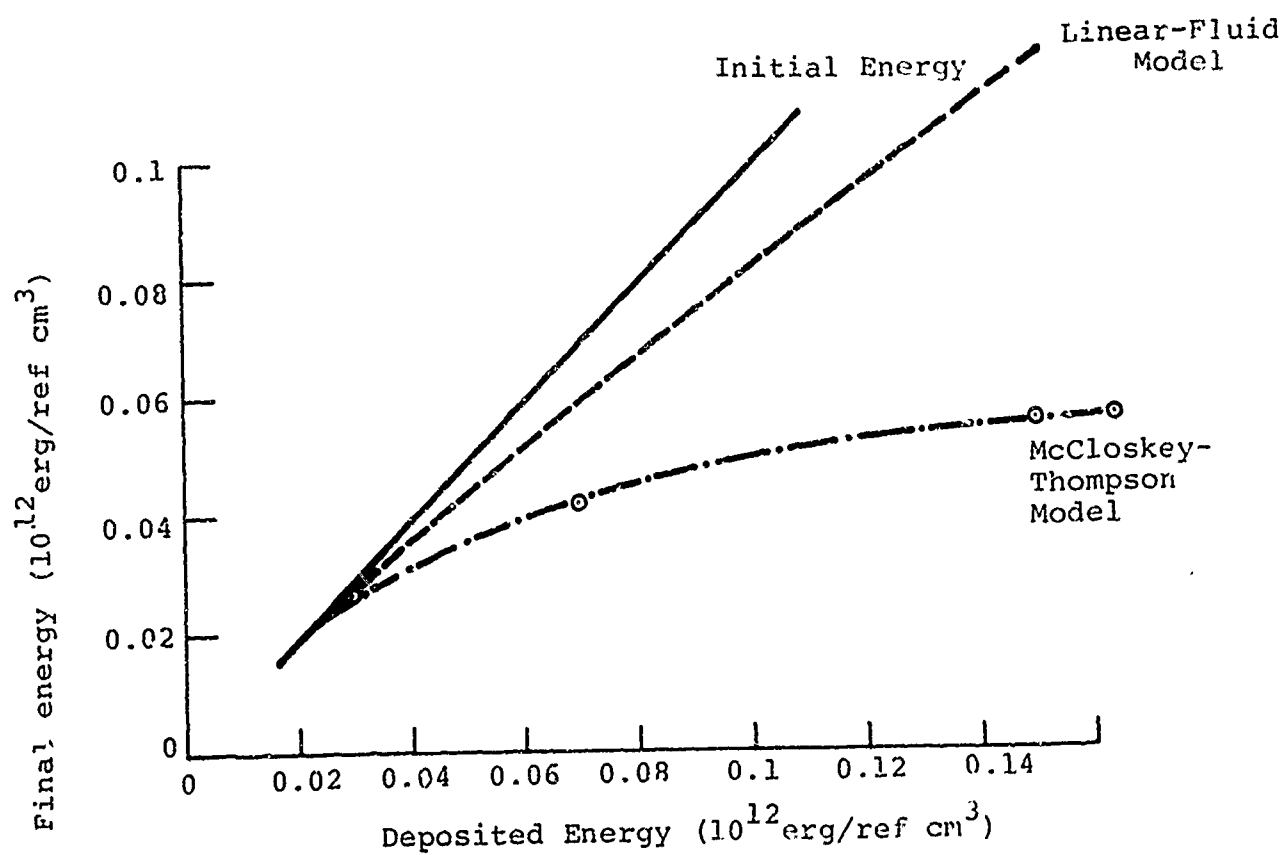
FIGURE 45. FINAL-STATE ENERGY FOR ALUMINUM

8777

The other interesting feature of the expression is the dependence on the volume at which energy is deposited, shown in Figure 46, for the parameters of alumin.. and a dose of 0.1 Mbar ($\approx$ 900 cal/g). This shows qualitatively that if the deposition time is not zero, so that loading near the front surface is at relative volumes larger than one, the impulse will be reduced. In contrast to this, the expression for kinetic energy of a γ-law gas, by a similar derivation, can be shown to be

$$\Delta E = (E_o - E_s)$$

where E_s is the unavailable energy (required to overcome the potential well of the lattice), independent of the volume at which it is deposited. Thus we have the first indication of the importance of deposition time in melt-dominated impulse.

With the approximations of

1. Linear deposition profile
2. Material removed to the end of the range, r(cm)
3. Fluence $= (1/2\ \varepsilon_o\ \rho_o r)$ where ε_o is the front surface dose in (cal/g)*
4. Linearized expression for ΔE
5. Whitener expression for impulse,

the impulse is given by

$$I = 0.04186\ \frac{r}{2\ C_k}\ \phi$$

where I is the impulse in ktap, C_k is the bulk sound speed in cm/μsec ($= \sqrt{K/\rho_o}$), and ϕ is the fluence in cal/cm^2. This is most easily derived by considering that the momentum density (u) is given by

---

*This assumes that bremsstrahlung losses and electron back-scattering losses are neglected.
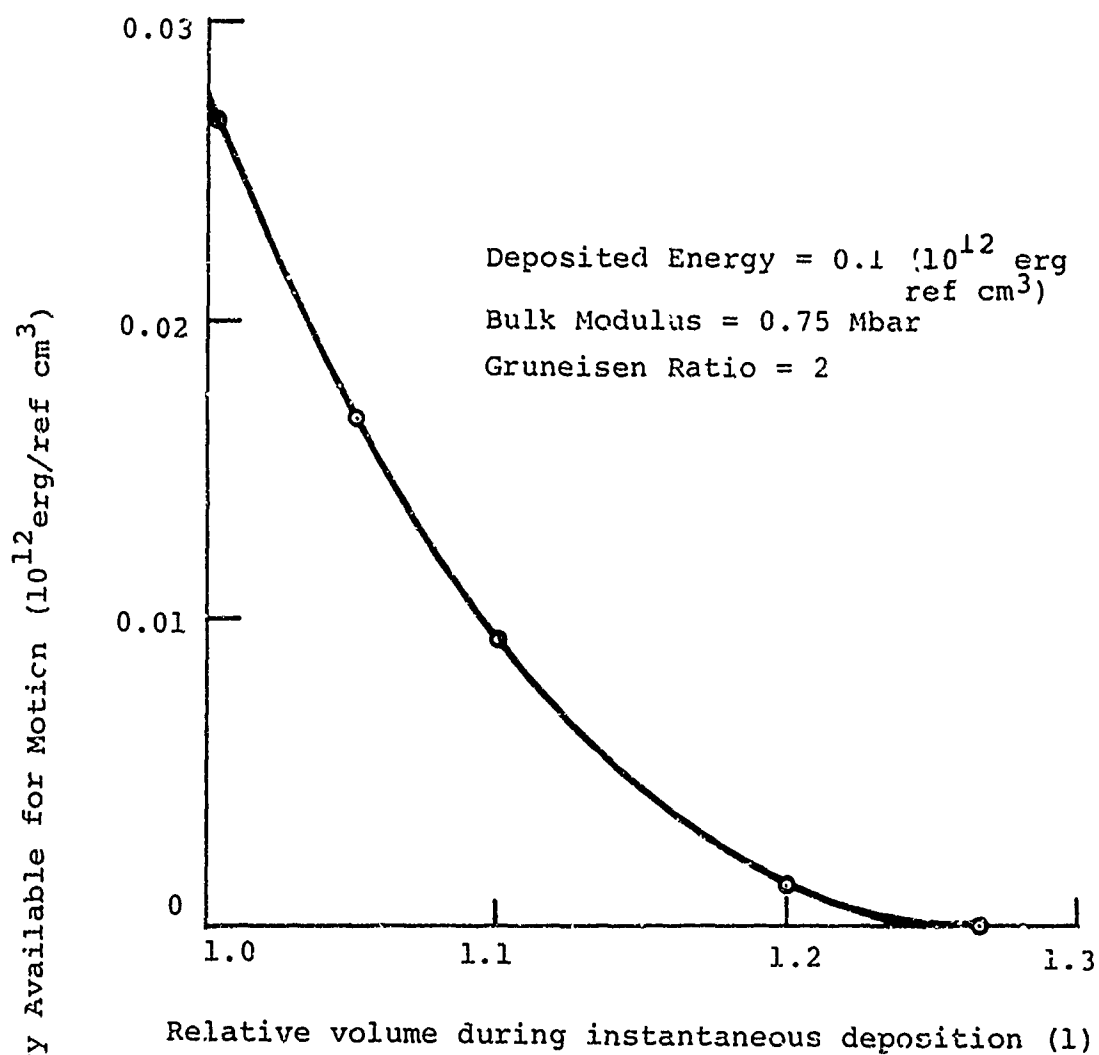
FIGURE 46.   ENERGY AVAILABLE FOR MOTION IN ALUMINUM

107

$$u = \left(2 \, \frac{\Delta E}{\rho_o} \right)^{\frac{1}{2}}$$

where ΔE is the kinetic energy density (10^{12} erg/ref cm^3), u is in cm/μsec, and integrating the velocity over the mass that is included in the electron range.

The expression for impulse is, of course, only appropriate for negligible deposition times, but is useful for predicting upper bounds for melt-dominated impulse. Before considering the effects of deposition time, there is additional information contained in the expression for impulse and kinetic energy that should be noted.

First the expression for impulse has only two material sensitive parameters, Γ and C_k, and for metals, the ratio varies by about a factor of 10 from Be (1.45) to Pb (13.3). Second, the velocity given by $u = \sqrt{(2\Delta E/\rho_o)}$ is just $P/\rho_o \, C_k$, the particle velocity that would be expected from the Hugoniot jump conditions and the first order approximation that the velocity from a rarefaction (the Riemann invariant) U_r, is just the particle velocity, U_p. Third, since neither Γ nor C_k are sensitive to small alloy concentration, the difference in impulse between different alloys is expected to be small.

Finally the linear fluid model is compared with the McCloskey-Thompson model and with the experimental data in aluminum (Figure 47)

The effect of deposition time has been considered by Bade, et al., (Reference 18), in their calculation of non-blowoff impulse I_N. When their formulas are generalized to an arbitrary deposition profile (Reference 19), the expression for non-blowoff impulse is
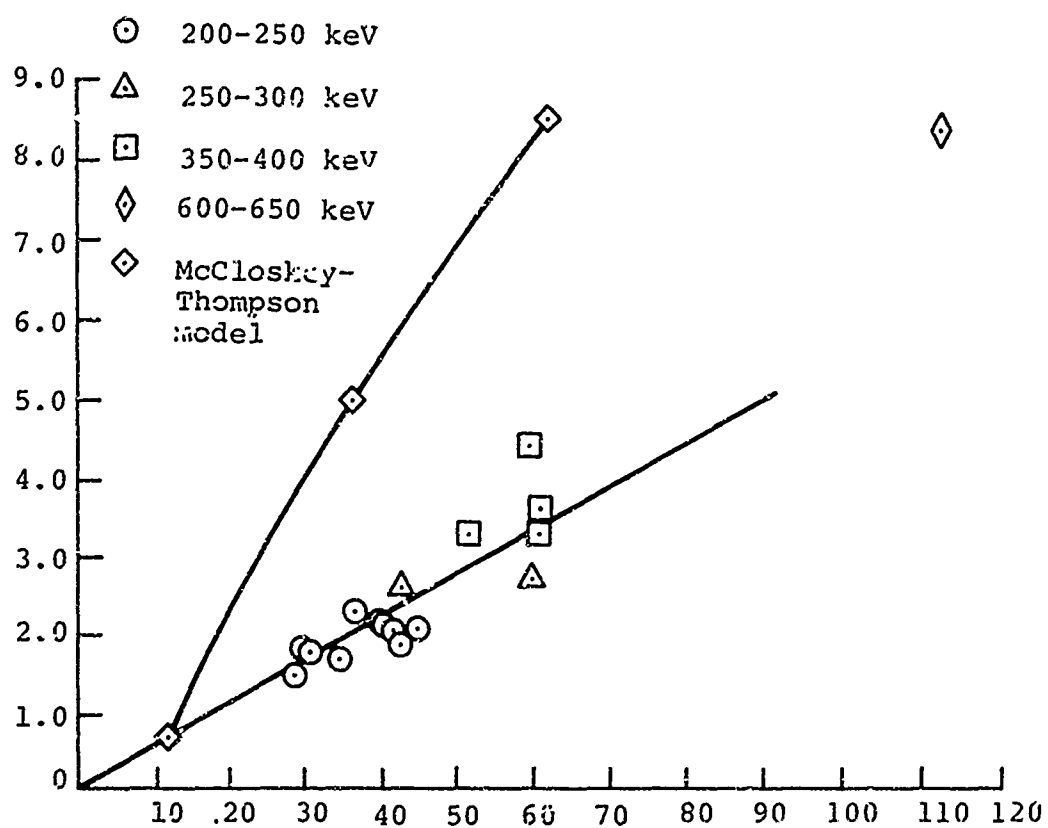
FIGURE 47.   McCLOSKEY-THOMPSON-BBAY EXPRESSION AND LINEAR
FLUID MODEL FOR IMPULSE

109

$$I_N = \frac{r}{C_k^2 t_D} \left[\frac{C_k t_D}{2} \int_{C_k t_D/2}^{r} \varepsilon'(x) \, dx + \int_{0}^{C_k t_D/2} x \, \varepsilon'(x) \, dx \right]$$

When this formula is specialized for a linear deposition profile, and the approximation that the fluence, ϕ, is given by

$$\phi = \frac{1}{2} \varepsilon_o \, r \, \rho_o$$

is retained, the expression for impulse becomes

$$I = 0.0418 \frac{r}{2C_k} \phi \, f(\xi)$$

where

$$f(\xi) = \begin{cases} 1 - \xi + 1/3 \, \xi^2, & \xi < 1 \\[2ex] 1/3 \, 1/\xi & , \, \xi \geq 1 \end{cases}$$

and

$$\xi = \frac{1}{2} \frac{C_k t_D}{r}$$

For

$$C_k t_D \lesssim 3.5 \, r, \quad f(\xi) \simeq e^{-\xi} \pm 7\%$$

as can be seen in Figure 48. Thus, to the accuracy of the approximations we may use

$$I = 0.0418 \frac{r}{2C_k} \phi \, e^{-(C_k t_D)/2r} \, , \quad \text{for} \quad C_k t_D \lesssim 3.5 \, r$$

To compare the expression with electron-beam impulse data more readily, Figure 2-13 of Reference 20 has been used to obtain the range of electrons in g/cm^2, $\rho_o r$, as a function of mean electron energy $\langle \mathcal{E} \rangle$ (MeV) suitable for energies near 0.25 MeV for all materials.

110

FIGURE 48. COMPARISON OF DEPOSITION TIME-DEPENDENCE FUNCTIONS

111

From this figure

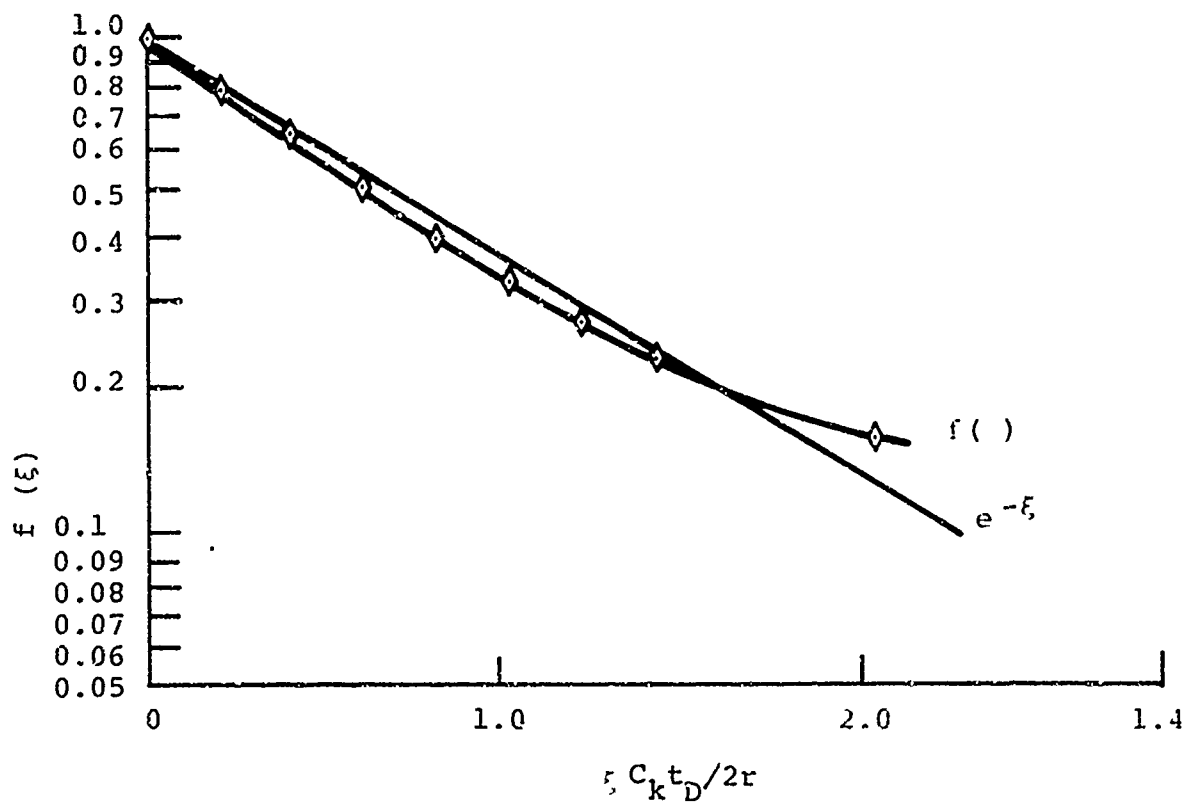$$\rho_o r = 1.2 \quad <\mathcal{E}>^2$$

Hence the deposition time dependence is given by

$$f\left(\frac{C_k t_D}{2r}\right) \sim \exp\left(-\frac{C_k t_D \rho_o}{2.4 \quad <\mathcal{E}>^2}\right)$$

The dependence of impulse on the deposition time should be strongly emphasized. For melt-dominated impulse, it becomes an important parameter. If, for example, an attempt were made to obtain an effective E_f by a least-squares fit to one of the analytical expressions, as discussed in Reference [17], and the deposition time was not considered, the results would not extrapolate to other deposition profiles with the same deposition time. Indeed, the final energy E_f could be a strong function of deposition time.

Figures 49, 50, and 51, taken from data reported in References 21 and 22, show impulse versus fluence for four materials--Mg, Al, Ag, Pb--without any scaling, scaled by the linearized impulse expression without regard to deposition time, and scaled by the full formula, respectively. The material properties used are standard PUFF equation-of-state parameters and are shown in Table III. From these figures, when the approximate time dependence and impulse formulas are used, there is quite reasonable agreement, and the data tend to cluster about the theoretical line that has no adjustable parameters.

Since the expression and hence the model for melt-dominated impulse has been verified, we may use the model to estimate the limits of the melt-dominated region.
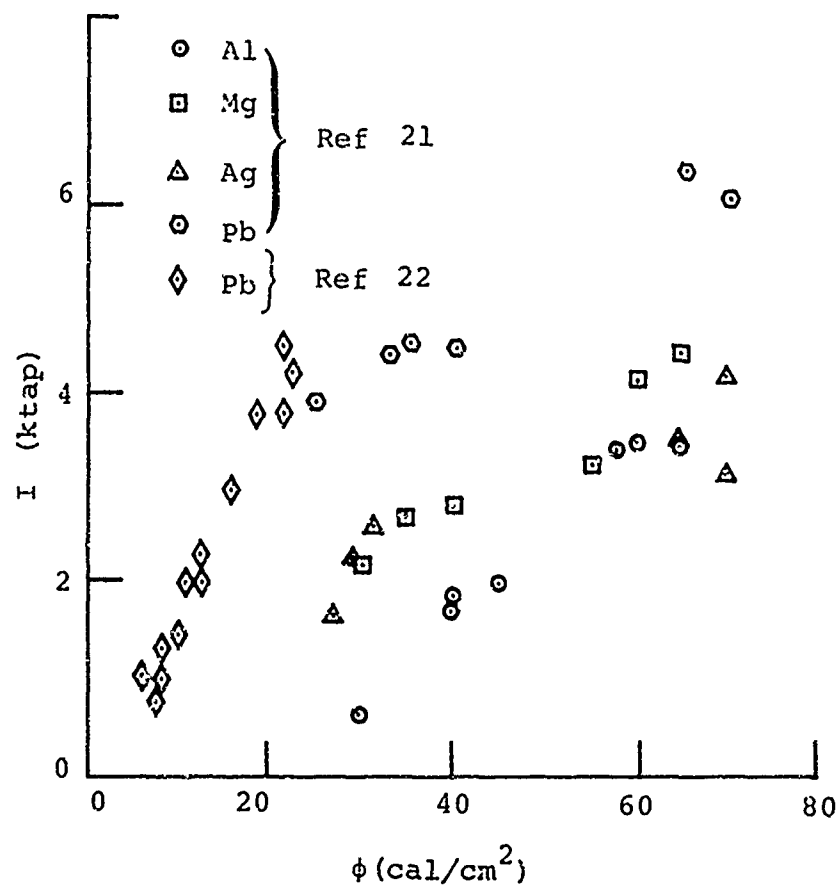
FIGURE 49   RAW IMPULSE DATA

113
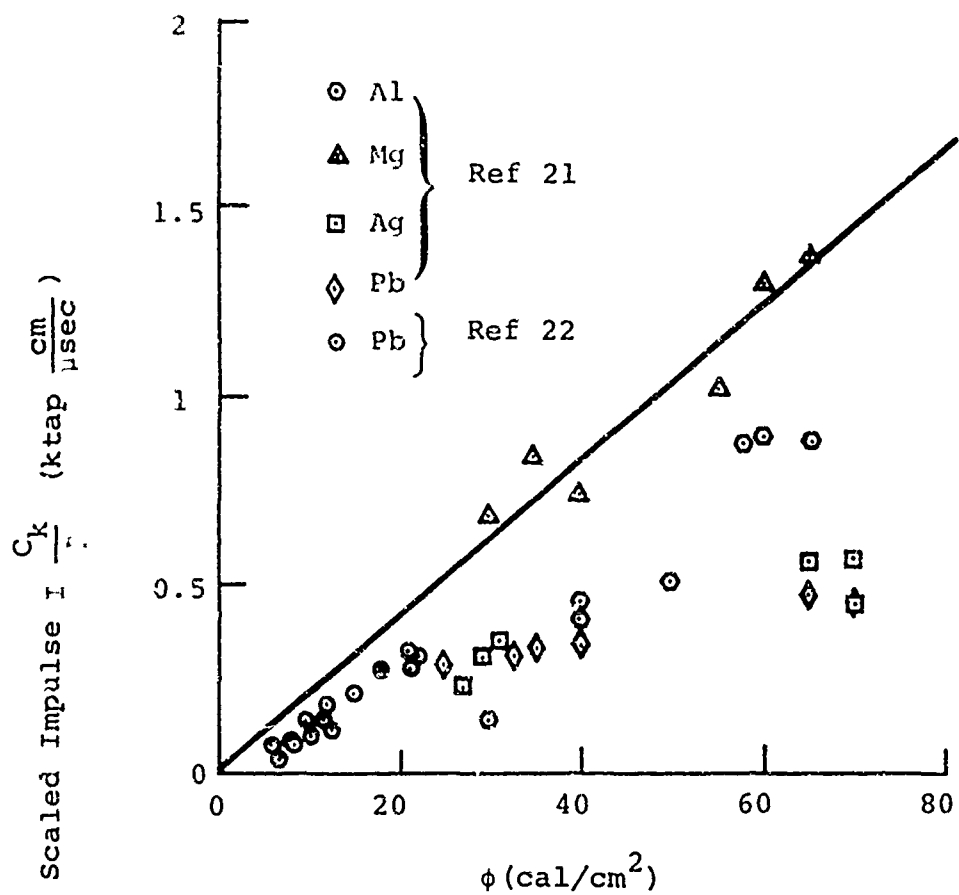
FIGURE 50   IMPULSE SCALED WITH DEPOSITION
            TIME DEPENDENCE

114
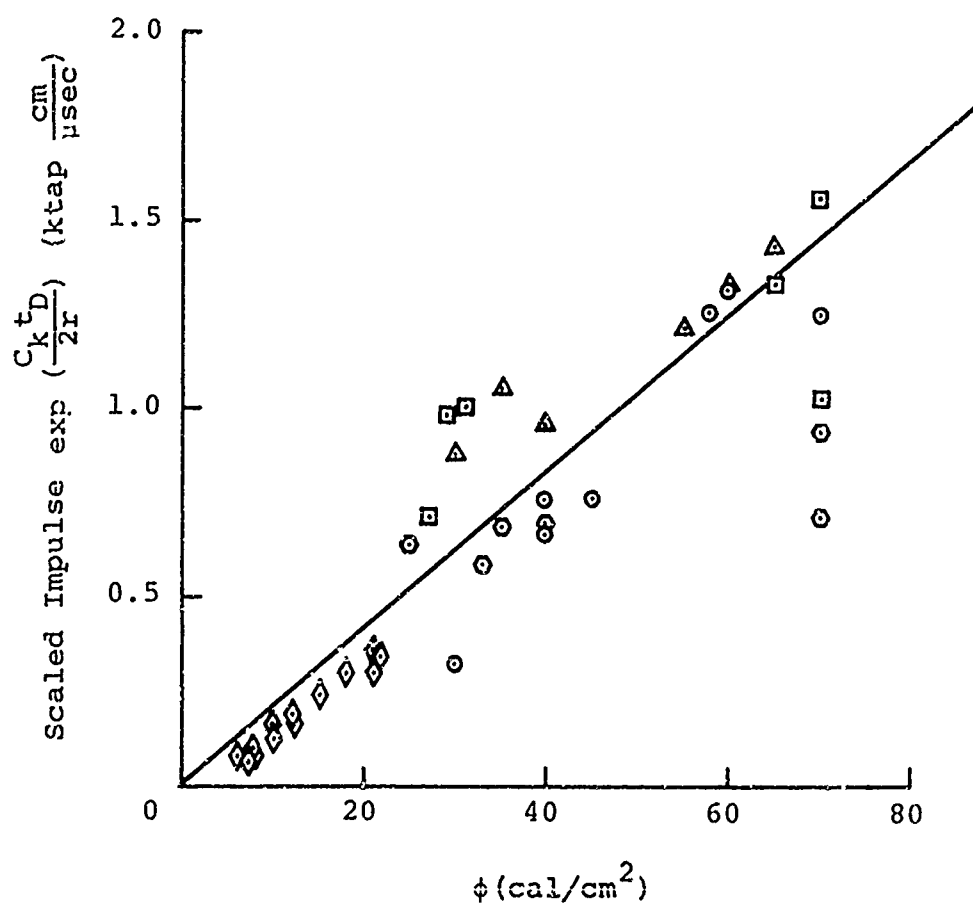
FIGURE 51.   IMPULSE SCALED WITH DEPOSITION TIME DEPENDENCE

TABLE III

PARAMETERS USED FOR SCALING IMPULSE DATA

	r	C_k (cm/μsec)	ρ_o (g/cm^3)	t_D (μsec)
Al	2.13	0.536	2.70	0.03
Mg	1.46	0.450	1.74	0.03
Ag	2.34	0.327	10.5	0.03
Pb	2.78	0.209	11.3	0.03

116

We assume that the liquid and solid both have the same bulk modulus, K; then, the intersection of the release adiabat with the liquid-vapor dome will be at a pressure depending on the initial internal energy. The release adiabat of the liquid that intersects the liquid vapor dome at about 0.1 kbar, extended to zero pressure, reaches a volume of approximately $1/2\ v_c$, v_c being the critical-point volume (Reference 23). The 0.1 kbar level is chosen more or less arbitrarily so that any impulse contribution from the vapor, which should be complete by ≈ 4 μsec, is less than 0.2 ktap. With the approximation that $v_c \simeq 3v_{ref}$, we estimate the internal energy required to reach this adiabat by using

$$v^* = v_o\ (1 + \epsilon)^{1/(\Gamma + 1)}$$

If the energy is deposited at reference volume, this gives

$$E_o\ (cal/g) = \frac{K \times 10^5}{4.186\ \rho_o\ \Gamma(\Gamma + 1)}\ (1.5^{\Gamma + 1} - 1)$$

For aluminum, $K = 0.75$ Mbar, $\Gamma = 2$, $\rho_o = 2.7$ and this gives

$$E_o \cdot ' 2600\ cal/g$$

as the approximate upper bound for the melt-dominated impulse region.

C. ANALYSIS OF OTHER TECHNIQUES USED FOR IMPULSE MEASUREMENTS

At this point, a model for melt-dominated impulse has been
proposed, and a simplified formula for the dominant features of
impulse generation has been derived. To check the model more
carefully, information about the propagated stress wave is re-
quired. This information was obtained experimentally by measuring
the stress history with quartz gauges. The analytical details of
stress propagation were obtained by programming the model for liquid
splashoff as part of the constitutive relation in a Lagrange hydro-
dynamic code, POD.

The solid-liquid phase transition was ignored. The justification
for this is twofold: (1) The results of McQueen, et al. (Reference 24)
show that the liquid-solid transition in copper was virtually indis-
tinguishable on a shock speed-particle velocity plot, and (2) that
inclusion of the phase transition was unnecessary to obtain good
agreement with stress and impulse data. The constitutive relation,
then, describes the liquid phase as having the same bulk properties
as the solid, but with yield stress, shear modulus, and tensile
strength that approach zero as the internal energy reaches the en-
thalpy required to reach the melting point at 1 atm. The relations
used are shown in Table IV and Figure 52. With these constitutive
relations, machine diagnostics were used, as described in Reference 2,
to obtain the energy spectrum, mean angle of incidence of the electron
stream, fluence, and effective deposition time. The deposition
profile was then calculated by a Monte Carlo electron transport code,
and this information was used in a series of hydrodynamic code
calculations.

TABLE IV

CONSTITUTIVE RELATION FOR ALUMINUM

Pressure

$$P = 0.75\mu + 0.405\mu^2 + (2 + 2\mu)\ E \quad , \ \mu \geq 1 \qquad \text{(Ref 26)}$$

$$0.75\mu \qquad\qquad + (2 + 2\mu)\ E \quad , \ \mu < 1$$

Where $\mu = \rho/\rho_o - 1$

Shear Modulus

$$G = 0.275 - 15.28E \quad , \ E < 0.0181 \qquad \text{(Ref 26)}$$

$$0 \qquad\qquad\qquad E > 0.0181$$

Von Mises yield stress, $Y_0 = f(E)$, $f(E)$ is shown in Figure 52.

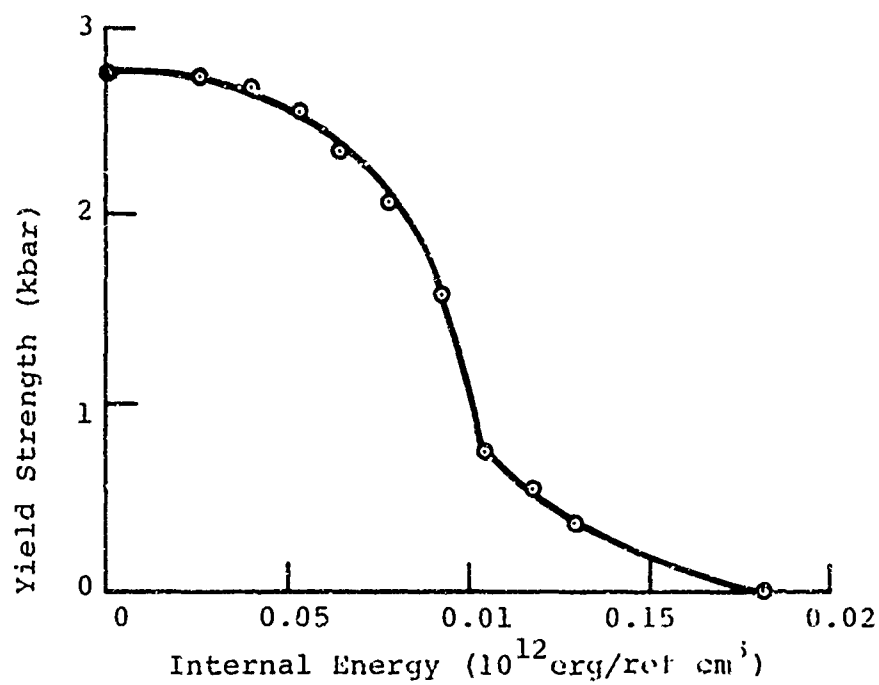Spall strength $P_{min}(E) = -0.006\ (1 - E/0.0181)$.

119

FIGURE 52. ENERGY-DEPENDENT YIELD STRENGTH OF ALUMINUM

The first series of calculations was made to obtain impulse by recording the momentum of the spalled liquid. The results of the calculations and the simplified model discussed in Section III are shown with the impulse data in Figure 53. In addition to these calculations, other calculations were made to verify the dependence of impulse on various constitutive parameters. They showed that, indeed, a 20% reduction in bulk modulus (programmed as a linear decrease with energy) caused a 10% increase in impulse, and that the effect of deposition time could be represented by exp $(- c_k \, t_D / 2r)$.

The second series was run to obtain the predicted stress histories in quartz. The deposition profile calculated for one of these is shown in Figure 54. To obtain agreement with the measurement, it was found necessary to include the epoxy bond between the quartz and the aluminum in the calculations. When this was done, the experimental and calculated stress histories were compared and are shown in Figure 55. The good agreement lends considerable credibility to the proposed model.

When the quartz gauge record is studied more carefully, it is noted that the integral of stress over time is 1.3 ktap, which is less than the calculated momentum in the spalled liquid, which was 1.6 ktap. The impedance mismatch of quartz and aluminum indicates that if the stress-time momentum in aluminum were 1.6 ktap, the quartz would show at least 1.5 ktap. Thus, we have a small but apparently real discrepancy in the calculation. To understand this discrepancy, one must consider the details of elastic-plastic behavior.
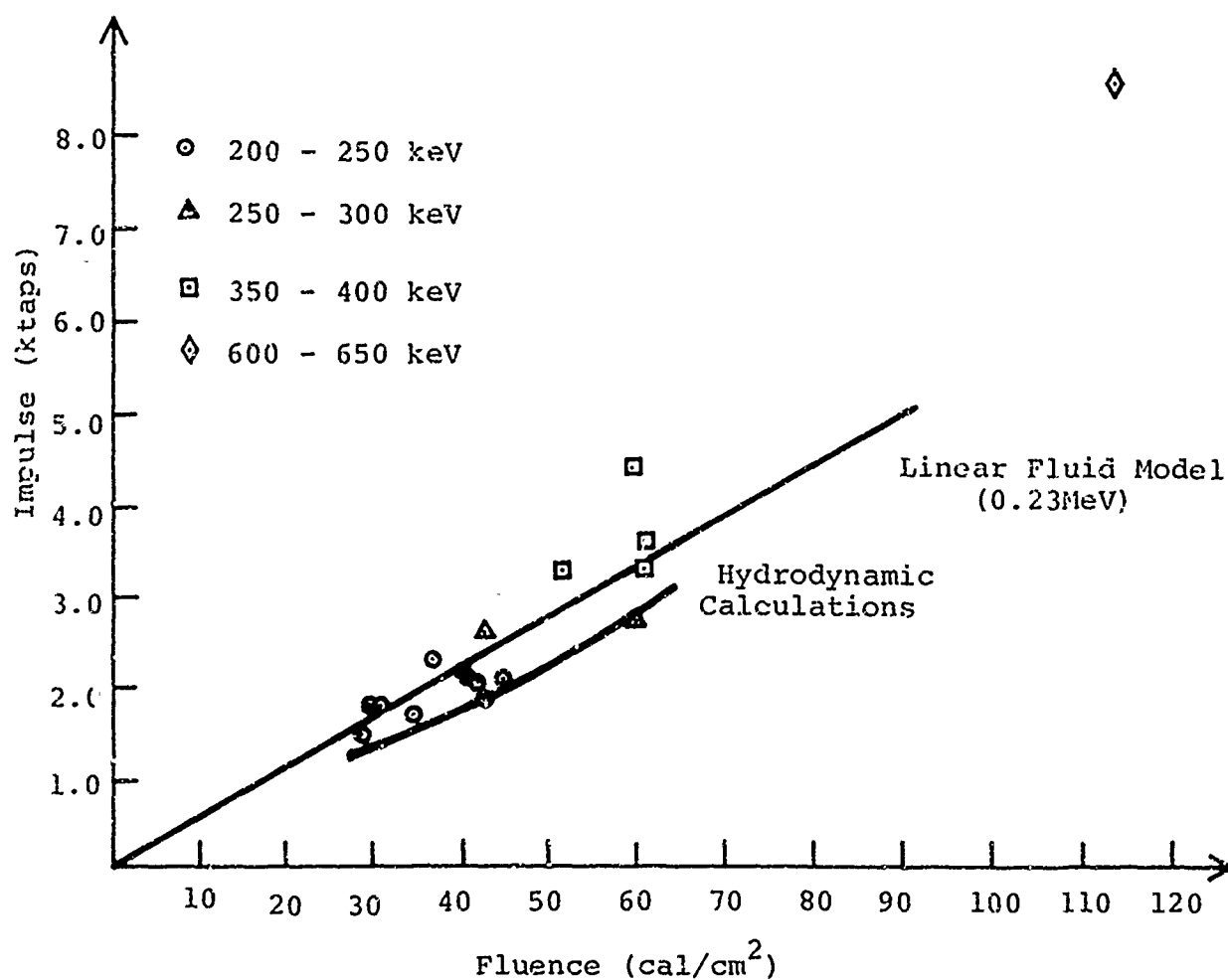
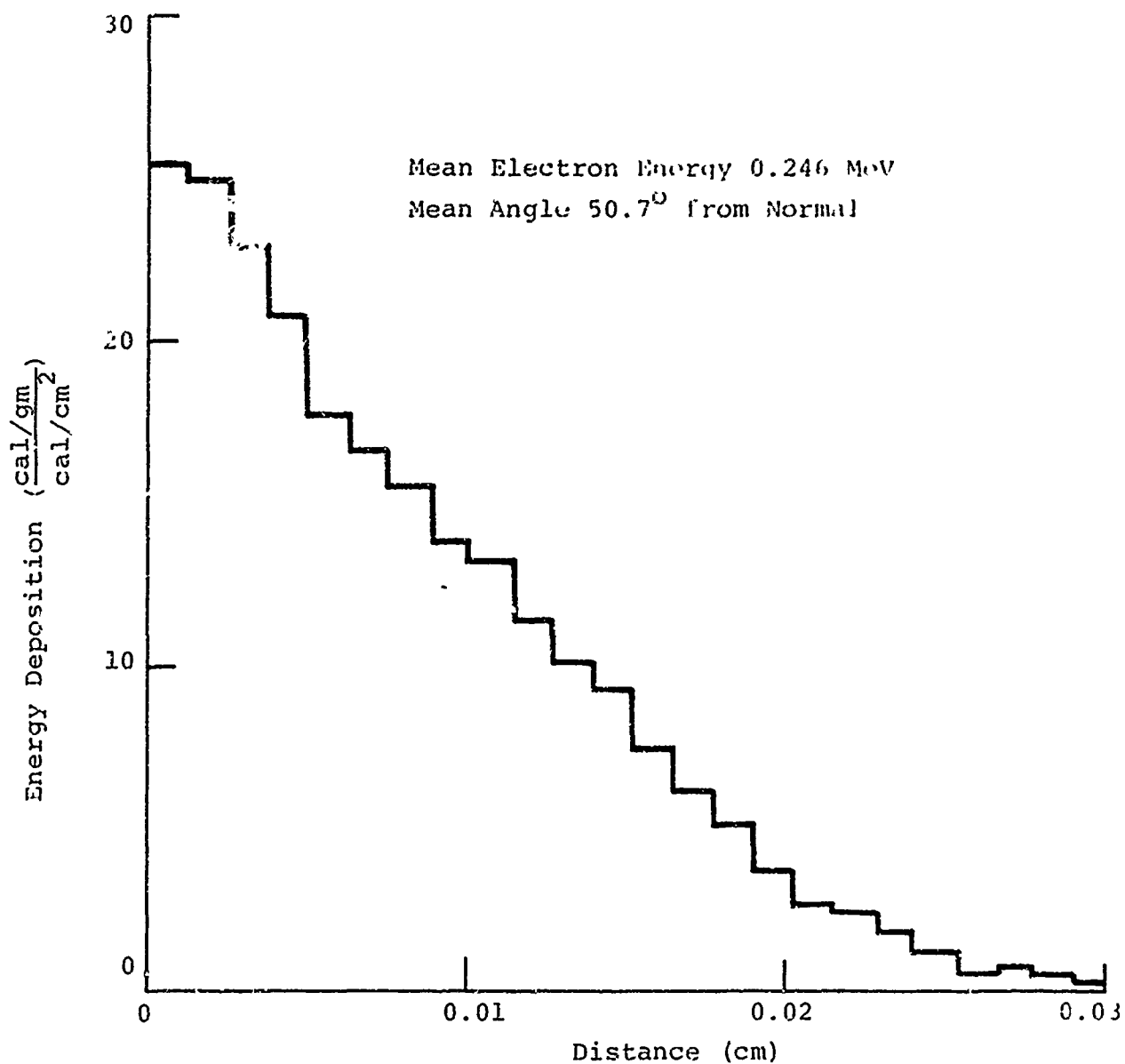FIGURE 53.   ELASTIC-PLASTIC HYDRODYNAMIC
CALCULATIONS OF IMPULSE

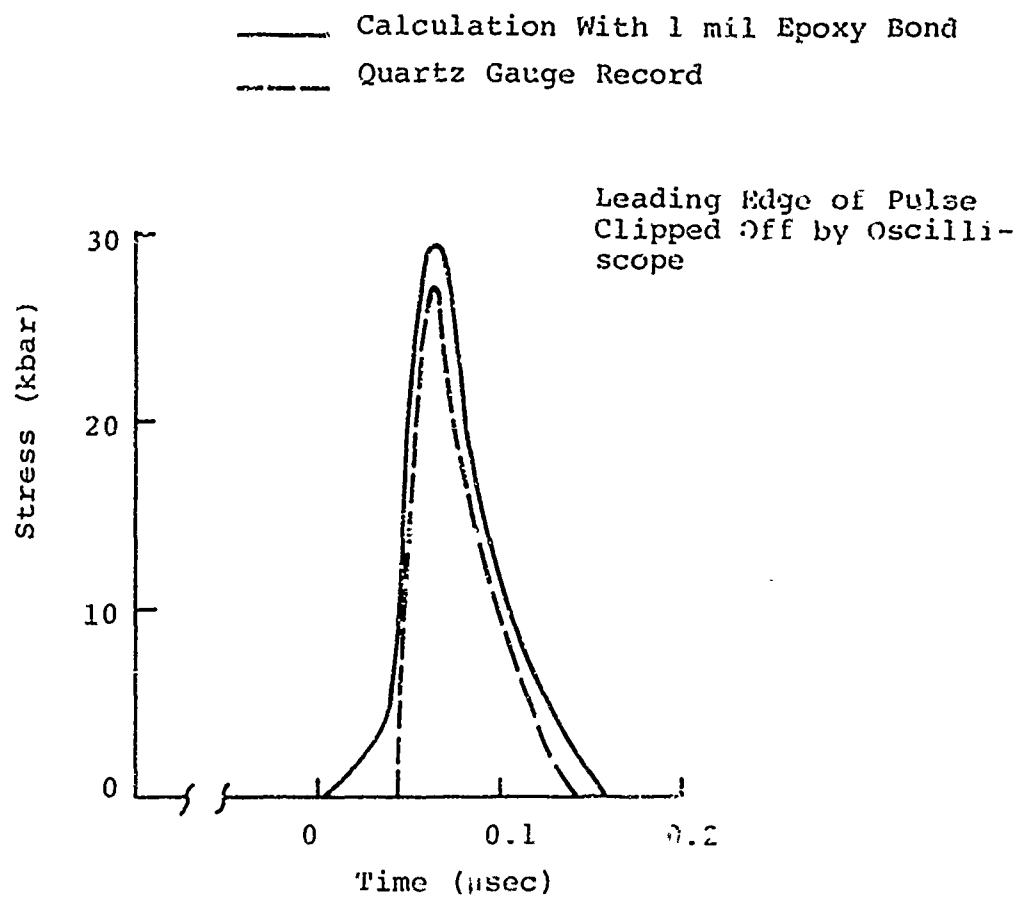FIGURE 54. DEPOSITION PROFILE IN ALUMINUM

FIGURE 55. STRESS HISTORY IN REAR-SURFACE QUARTZ GAUGE

8241

124

If enough material at the front surface is removed, the normal
tensile tail caused by thermal stress production (Reference 27) is
completely suppressed, and the traveling stress pulse is only com-
pressive. The path in stress-volume space that is traversed by
elastic-plastic compression and release has hysteresis; that is,
there is a residual compression. This same hysteresis occurs in
stress-particle velocity space, so that the result of passing a
compressive stress wave is to leave the material at a uniform
velocity. This velocity, for the parameters of aluminum used,
corresponds to 5×10^{-4} cm/µsec, which is 0.135 ktap/mm. The
distance that the stress wave traveled to reach the quartz in the
above calculation was greater than 1 mm, which accounts for the
discrepancy. This phenomenon will occur with all materials that
have different loading and unloading paths. Further, if the plastic
part of the stress wave in the irradiated sample is transmitted as
a stress wave that stays within the elastic limit of quartz, the
residual velocity of the material will appear as a stress offset
in the quartz, an apparent baseline shift.

A second technique suggested for the measurement of impulse is
the use of flier plates attached to the rear of irradiated samples.
The velocity of these plates can be measured by recording their
trajectories with a high-speed movie camera, and measuring the mass
and center-of-mass velocity. To relate this momentum to the ejecta
momentum, we will consider the one-dimensional stress-wave inter-
actions in some detail.

Assume that the flier and target have the same shock impedance,
and that the stress wave, however generated in the target, is an
elastic finite pulse. The first important feature is that the simple
energy and momentum conservation relations used for rigid bodies do
not work. That is, in the lab frame,

$$V_F \neq \frac{2m_T}{m_T + m_F} \, v_T$$

Indeed, for the same impedance targets,

$$v_F = \frac{m_T v_T}{m_F}$$

when the thickness of the plate, F, is such that the entire stress pulse can be contained in it.

This flier velocity is certainly a contradiction, and at first thought, it appears to be nonconservation of kinetic energy. That is, $m_F v_F^2 \neq m_T v_T^2 \, (m_T/m_F)$. The kinetic energy that is apparently lost, however, goes into the ringing of the elastic pulse, which becomes apparent when it is remembered that for a nonuniform velocity distribution— a pulse—the square of the average velocity is less than the average of the squared velocity. That is. when the kinetic energy associated with the momentum of a stress pulse is assumed smoothed into center-of-mass translation, kinetic energy is lost.

When the flier has higher shock impedance than the target, and the flier is thick enough to contain the pulse for elastic stresses,

$$v_F = \frac{2Z_F}{Z_T + Z_F} \, \frac{(m_T v_T)}{m_F}$$

where Z_F and Z_T are the respective shock impedances. If the impedance of the flier is less than the sample

$$v_F \leq \frac{(m_T v_T)}{m_F} \left(\frac{2Z_F}{Z_T + Z_F} \right)$$

126

how much less v_F is than the upper bound depends on the shape of the stress pulse.

If there is a hysteresis in the sample, then the flier, like the quartz gauge, will trap only part of the momentum. For "thick" fliers, with shock impedances greater than or equal to the target

$$m_F v_F \cong \frac{2 Z_F}{Z_T + Z_F} (m_T v_T - \rho_0 \ell u_r)$$

where u_r is the residual sample velocity. (For aluminum the subtractive term is ≈ 0.13 ktap/mm.)

Things are not nearly so simple, however, when the flier is not thick enough to contain the stress pulse, due to, say, vapor pushing for long times. In this case, a calculation of the stress waves is required to get even an approximate value for the momentum fraction trapped in the flier.

D. EJECTA VELOCITIES

A further test of the spall-dominated model, and probably more direct confirmation than even transmitted stress, would be agreement with calculated and measured ejecta velocities.

Under a program carried out at Physics International by D. Dean of the Sandia Corporation, (Reference 9), a number of experiments on the Pulserad 738 machine were performed using a high-speed framing camera to record the motion of the front surface ejecta. Selected frames of the front surface response of aluminum exposed to 40 cal/cm^2 of 0.26 MeV electrons are shown in Figure 36. The position leading and trailing edges of persistent structure in the ejecta show velocities of 0.06 and 0.020 cm/μsec. The calculated mean velocity for the deposition conditions was 0.03 cm/μsec. It is seen that good quantitative agreement between calculated and measured velocities exists within the uncertainty of the experiment, thereby providing confirmation of the melt-dominated model.

127

t=0

t=8μsec

t=16μsec
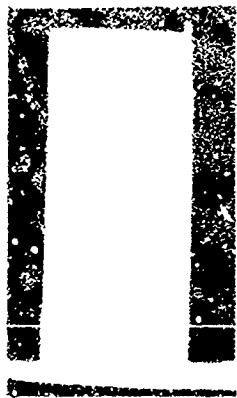
t=24μsec

FIGURE 56. EJECTA VELOCITY FROM SLAB

R8861

128

SECTION V

CONCLUSIONS

Measurements of impulse generation using a ballistic pendulum, transmitted stress histories using quartz gauges, and ejecta velocities using framing cameras have been successfully performed in an electron-beam environment. These measurements, together with analysis, have been used in an extensive program to study impulse generation in aluminum in the melt-dominated regime.

The major result of the combined analytical and experimental program is the conclusion that the description of material removal by liquid spall extends to rather large energy densities. In aluminum, for example, it is anticipated that energy densities nearly sufficient to cause complete vaporization at atmospheric pressure can be successfully treated by ignoring the vapor phase. This analysis was also seen to be a reasonable approximation for other simple materials. Thus, we take it as a general conclusion that the liquid-spall model is appropriate up to energy densities given approximately by

$$E_o \text{ (cal/g)} = \frac{K \times 10^5}{4.186 \, \rho_o \, \Gamma(\Gamma + 1)} (1.5^{\Gamma + 1} - 1)$$

where K is the bulk modulus in Mbar, Γ is the Gruneisen ratio, and ρ_o is the initial density in g/cm^3. When this formula is evaluated for various materials, Mg, Al, Ag, and Pb, the maximum dose is within 25% of the energy of vaporized metal at atmospheric pressure.

With recent improvements in achievable doses on the Pulserad 728, it is anticipated that an extension of the experimental results presented here would be made to experimentally verify the upper bound of the spall-dominated impulse region and to determine appropriate models in the mixed phase and vapor-dominated regions. A

129

combined analytical and experimental approach, such as used on this program and outlined in Figure 57, is recommended. In this way, the results of experiments and analysis can affect each other during the course of the program.

It is expected that such an approach will provide the fundamental basis of understanding required to model mixed-phase effects and permit the extension to even more complex materials such as fiber-reinforced composites.
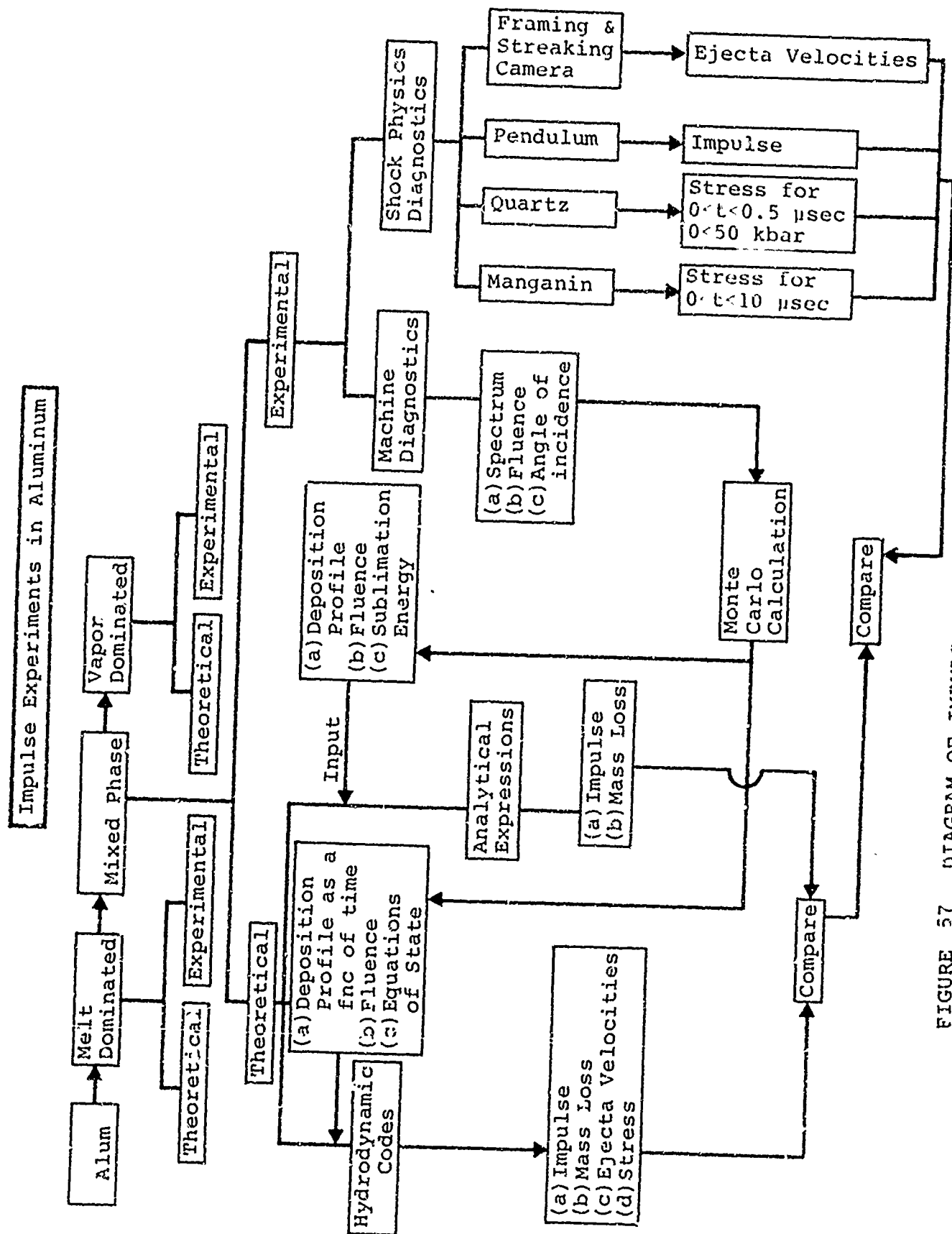
FIGURE 57   DIAGRAM OF IMPULSE EXPERIMENTS IN ALUMINUM

131

REFERENCES

1. G. Yonas and P. Spence, Experimental Investigation of High ν/γ Electron Beam Transport, PIFR-106, Physics International Company, San Leandro, California, October 1968.

2. G. Yonas, P. Spence, D. Pellinen, B. Ecker, and S. Heurlin, Dynamic Effects of High ν/γ Beam Plasma Interactions, PITR-106-1, Physics International Company, San Leandro, California, April 1969.

3. G. Yonas, P. Spence, B. Ecker, and J. Rander, Dynamic Effects of High ν/γ Beam Plasma Interactions, PIFR-106-2, Physics International Company, San Leandro, California, August 1969.

4. I. Smith and R. Ward, Development and Application of Mylar Striplines, PIFR-137, Physics International Company, San Leandro, California.

5. P. Spence and G. Yonas, Generation, Control and Diagnosis of High Energy Density Electron Beams, PITR-205-1, Physics International Company, San Leandro, California, October 1969.

6. P. Spence and G. Yonas, Impulse Generation in Several Materials Under High Energy Density Electron Beam Environment, PIFR-205, Physics International Company, San Leandro California, February 1970.

7. Ya. B. Zel'dovich and Yu. P. Raizer, Physics of Shock Waves and High-Temperature Hydrodynamic Phenomena, Vol. II, Academic Press, New York, N.Y. (1966).

8. W. Bade, Radiation Damage Study, Final Report, Vol. II, AVCO, Wilmington, Mass. AVMSD-0339-66-RR, Vol. II (1966) (Classified Report).

9. P. Spence, G. Yonas, and D. Dean, "Shock Generation in S-200 Beryllium Using a Pulsed Electron Beam," Bull. Amer. Phys. Soc., 14, 1070 (1969).

10. J. H. Tillotson, Metallic Equations of State for Hypervelocity Impact, Gulf General Atomic, San Diego, California, Report No. GA-3216 (1962).

11. R. Hofmann and J. Reaugh, Shock Hydrodynamic Calculations in Wires, PIFR-104, Physics International Company, San Leandro, California (1968).

12. R. Brodie and J. Hormuth, The PUFF 66 and PPUFF 66 Computer Programs, Air Force Weapons Laboratory, Kirtland Air Force Base, New Mexico, Report No. AFWL-TR-66-48 (1966).

13. The MONK Code, PIFR-119, Physics International Company, San Leandro, California (1969).

14. S. Kormer, A. Funtikov, V. Urlin, and A. Kolesnikova, Sov. Phys. JETP 15, (3), 477 (1962).

15. J. Hirschfelder, R. Buehler, H. McGee, Jr., and J. Sutton, "Generalized Equation-of-State for Gases and Liquids, "Industrial and Engineering Chemistry, 50, (3), 375 (1958).

16. J. Hirschfelder, C. Curtiss and R. Bird, Molecular Theory of Gases and Liquids, John Wiley and Sons, New York, N. Y. (1958).

17. J. Reaugh, Impulse Calculations, PIQR-144-1, Physics International Company, San Leandro, California, July 1969.

18. W. L. Bade, J. P. Averell, and J. M. Yos, Analytical Theory of X-Ray Effects, AFSWC TDR-62-92, AVCO Corporation, Wilmington, Mass., September 1966.

19. G. Yonas, Dynamic Fracture Assessment of a Re-Entry Vehicle Composite, PIFR-093, Physics International Company, San Leandro, California, August 1968.

20. E. Segre, Nuclei and Particles, W. A. Benjamin and Company, Inc., New York, N. Y. (1965), p. 36.

21. A. Lutze and G. Yonas, Testing Services, PIFR-141, Physics International Company, San Leandro, California, March 1968.

22. L. W. Woodruff, Thermodynamic Effects Induced in Metals by a 2-MeV Pulsed Electron Beam, UCRL-50621, Lawrence Radiation Laboratory, Livermore, California, April 1969.

23. R. S. Wright and L. A. Johnson, SUPER PUFF Program Equation-of-State, Autoneutronic Division of Philco-Ford, October 1968.

24. R. G. McQueen, et al., The Solid-Liquid Phase Line in Cu, Los Alamos Scientific Laboratory of the University of California, Los Alamos, New Mexico, LA-DC-9988 (1968) (Preprint).

25. A. Lutze and G. Yonas, Techniques Used in Impulse Experiments, PIQR-144-2, Physics International Company, San Leandro, California, December 1969.

26. R. Hofmann, D. J. Andrews, and D. E. Maxwell, "Computed Shock Response of Porous Aluminum," J. Appl. Phys. 39, 10, 4555 (1968).

27. J. C. Bushnell and D. J. McCloskey, "Thermoelastic Stress Production in Solids," J. Appl. Phys. 39 (12), 5541 (1968).

DOCUMENT CONTROL DATA - R&D		
(Security classification of title, body of abstract and indexing annotation must be entered when the overall report is classified)		

1 ORIGINATING ACTIVITY (Corporate author)	2a REPORT SECURITY CLASSIFICATION
Physics International Company 1700 Merced Street San Leandro, California 94577	UNCLASSIFIED
	2b GROUP

3 REPORT TITLE

Melt-Dominated Impulse Experiments and Calculations

4 DESCRIPTIVE NOTES *(Type of report and inclusive dates)*

Summary January 1969 to April 1970

5 AUTHOR(S) *(Last name, first name, initial)*

Reaugh, J.; Lutze, A.; and Yonas, G.

6 REPORT DATE	7a TOTAL NO OF PAGES	7b NO OF REFS
April 1970	135	27

8a CONTRACT OR GRANT NO.	9a ORIGINATOR'S REPORT NUMBER(S)
DASA-01-69-C-0065	
b PROJECT NO NWER XAXA	PIFR-144
c Task and Subtask C321	9b OTHER REPORT NO(S) (Any other numbers that may be assigned this report)
d Work Unit 02	DASA 2475

10 AVAILABILITY/LIMITATION NOTICES

This document has been approved for public release and sale; its distribution is unlimited.

11 SUPPLEMENTARY NOTES	12 SPONSORING MILITARY ACTIVITY
	Director Defense Atomic Support Agency Washington, D. C. 20305

13 ABSTRACT

A combined experimental and analytical study of impulse generation in aluminum has been carried out using intense electron beams as the source of high energy density loading. Both analytical models and hydrodynamic codes were used in the modeling of the observed material response. In addition this report presents a detailed survey of current calculational techniques and an extensive discussion of the experimental methods required for this work. For the electron beam fluence range employed here, giving peak doses less than 2000 cal/g, a model of liquid spall was found to represent the data well. This model was simplified to an analytical expression which depends exponentially on deposition time and is suitable for predicting melt-dominated impulse in a wide range of materials. In addition, hydrodynamic code calculations have been carried out and comparisons are made with measured transmitted stress histories and liquid ejecta velocities.

DD FORM 1473 1 JAN 64

KEY WORDS	LINK A		LINK B			
	ROLE	WT	ROLE	WT		
Impulse						
Electron Beams						
Stress Generation						
Liquid Spall						
Hydrodynamic Codes						

INSTRUCTIONS

1. ORIGINATING ACTIVITY: Enter the name and address of the contractor, subcontractor, grantee, Department of Defense activity or other organization (corporate author) issuing the report.

2a. REPORT SECURITY CLASSIFICATION: Enter the overall security classification of the report. Indicate whether "Restricted Data" is included. Marking is to be in accordance with appropriate security regulations.

2b. GROUP: Automatic downgrading is specified in DoD Directive 5200.10 and Armed Forces Industrial Manual. Enter the group number. Also, when applicable, show that optional markings have been used for Group 3 and Group 4 as authorized.

3. REPORT TITLE: Enter the complete report title in all capital letters. Titles in all cases should be unclassified. If a meaningful title cannot be selected without classification, show title classification in all capitals in parenthesis immediately following the title.

4. DESCRIPTIVE NOTES: If appropriate, enter the type of report, e.g., interim, progress, summary, annual, or final. Give the inclusive dates when a specific reporting period is covered.

5. AUTHOR(S): Enter the name(s) of author(s) as shown on or in the report. Enter last name, first name, middle initial. If military, show rank and branch of service. The name of the principal author is an absolute minimum requirement.

6. REPORT DATE: Enter the date of the report as day, month, year; or month, year. If more than one date appears on the report, use date of publication.

7a. TOTAL NUMBER OF PAGES: The total page count should follow normal pagination procedures, i.e., enter the number of pages containing information.

7b. NUMBER OF REFERENCES: Enter the total number of references cited in the report.

8a. CONTRACT OR GRANT NUMBER: If appropriate, enter the applicable number of the contract or grant under which the report was written.

8b, 8c, & 8d. PROJECT NUMBER: Enter the appropriate military department identification, such as project number, subproject number, system numbers, task number, etc.

9a. ORIGINATOR'S REPORT NUMBER(S): Enter the official report number by which the document will be identified and controlled by the originating activity. This number must be unique to this report.

9b. OTHER REPORT NUMBER(S): If the report has been assigned any other report numbers (either by the originator or by the sponsor), also enter this number(s).

10. AVAILABILITY LIMITATION NOTICES: Enter any limitations on further dissemination of the report, other than those imposed by security classification, using standard statements such as:

(1) "Qualified requesters may obtain copies of this report from DDC."

(2) "Foreign announcement and dissemination of this report by DDC is not authorized."

(3) "U. S. Government agencies may obtain copies of this report directly from DDC. Other qualified DDC users shall request through

_____."

(4) "U. S. military agencies may obtain copies of this report directly from DDC. Other qualified users shall request through

_____."

(5) "All distribution of this report is controlled. Qualified DDC users shall request through

_____."

If the report has been furnished to the Office of Technical Services, Department of Commerce, for sale to the public, indicate this fact and enter the price, if known.

11. SUPPLEMENTARY NOTES: Use for additional explanatory notes.

12. SPONSORING MILITARY ACTIVITY: Enter the name of the departmental project office or laboratory sponsoring (paying for) the research and development. Include address.

13. ABSTRACT: Enter an abstract giving a brief and factual summary of the document indicative of the report, even though it may also appear elsewhere in the body of the technical report. If additional space is required, a continuation sheet shall be attached.

It is highly desirable that the abstract of classified reports be unclassified. Each paragraph of the abstract shall end with an indication of the military security classification of the information in the paragraph, represented as (TS), (S), (C), or (U).

There is no limitation on the length of the abstract. However, the suggested length is from 150 to 225 words.

14. KEY WORDS: Key words are technically meaningful terms or short phrases that characterize a report and may be used as index entries for cataloging the report. Key words must be selected so that no security classification is required. Identifiers, such as equipment model designation, trade name, military project code name, geographic location, may be used as key words but will be followed by an indication of technical context. The assignment of links, roles, and weights is optional.